A UNITED STATES DEPARTMENT OF COMMERCE PUBLICATION

NOAA Technical Report ERL 228-AOML 7-2

U.S. DEPARTMENT OF COMMERCE
National Oceanic and Atmospheric Administration
Environmental Research Laboratories

Sea Surface Topography From Space
Volume II

JOHN R. APEL, Editor

BOULDER, COLO.
MAY 1972

ENVIRONMENTAL RESEARCH LABORATORIES

The mission of the Environmental Research Laboratories is to study the oceans, inland waters, the lower and upper atmosphere, the space environment, and the earth, in search of the understanding needed to provide more useful services in improving man's prospects for survival as influenced by the physical environment. Laboratories contributing to these studies are:

Earth Sciences Laboratories (ESL): Geomagnetism, seismology, geodesy, and related earth sciences; earthquake processes, internal structure and accurate figure of the Earth, and distribution of the Earth's mass.

Atlantic Oceanographic and Meteorological Laboratories (AOML): Oceanography, with emphasis on the geology and geophysics of ocean basins, oceanic processes, sea-air interactions, hurrican research, and weather modification (Miami, Florida).

Pacific Oceanographic Laboratories (POL): Oceanography; geology and geophysics of the Pacific Basin and margins; oceanic processes and dynamics; tsunami generation, propagation, modification, detection, and monitoring (Seattle, Washington).

Atmospheric Physics and Chemistry Laboratory (APCL): Cloud physics and precipitation; chemical composition and nucleating substances in the lower atmosphere; and laboratory and field experiments toward developing feasible methods of weather modification.

Air Resources Laboratories (ARL): Diffusion, transport, and dissipation of atmospheric contaminants; development of methods for prediction and control of atmospheric pollution (Silver Spring, Maryland).

Geophysical Fluid Dynamics Laboratory (GFDL): Dynamics and physics of geophysical fluid systems; development of a theoretical basis, through mathematical modeling and computer simulation, for the behavior and properties of the atmosphere and the oceans (Princeton, New Jersey).

Research Flight Facility (RFF): Outfits and operates aircraft specially instrumented for research; and meets needs of NOAA and other groups for environmental measurements for aircraft (Miami, Florida).

National Severe Storms Laboratory (NSSL): Tornadoes, squall lines, thunderstorms, and other severe local convective phenomena toward achieving improved methods of forecasting, detecting, and providing advance warnings (Norman, Oklahoma).

Space Environment Laboratory (SEL): Conducts research in solar-terrestrial physics, provides services and technique development in areas of environmental monitoring, forecasting, and data archiving.

Aeronomy Laboratory (AL): Theoretical, laboratory, rocket, and satellite studies of the physical and chemical processes controlling the ionosphere and exosphere of the earth and other planets.

Wave Propagation Laboratory (WPL): Development of new methods for remote sensing of the geophysical environment; special emphasis on propagation of sound waves, and electromagnetic waves at millimeter, infrared, and optical frequencies.

Marine Minerals Technology Center (MMTC): Research into aspects of undersea mining of hard minerals: development of tools and techniques to characterize and monitor the marine mine environment; prediction of the possible effects of marine mining on the environment; development of fundamental mining technology (Tiburon, California).

NATIONAL OCEANIC AND ATMOSPHERIC ADMINISTRATION

BOULDER, COLORADO 80302

U.S. DEPARTMENT OF COMMERCE
Peter G. Peterson, Secretary

NATIONAL OCEANIC AND ATMOSPHERIC ADMINISTRATION
Robert M. White, Administrator
ENVIRONMENTAL RESEARCH LABORATORIES
Wilmot N. Hess, Director

NOAA TECHNICAL REPORT ERL 228-AOML 7-2

Sea Surface Topography From Space

Volume II

Proceedings of a Conference Sponsored Jointly by
The National Oceanic and Atmospheric Administration,
The National Aeronautics and Space Administration,
and The United States Navy, Key Biscayne, Florida
October 6-8, 1971

Host Organization: Atlantic Oceanographic and Meteorological Laboratories, Environmental Research Laboratories, National Oceanic and Atmospheric Administration, U.S. Department of Commerce

JOHN R. APEL, Editor

BOULDER, COLO.
May 1972

For sale by the Superintendent of Documents, U. S. Government Printing Office, Washington, D. C. 20402
Price $1.25

FOREWORD

Our generation faces two great challenges to our innate curiosity about the place in which we live, the exploration of space and the understanding of our global ocean. These two endeavors are considered by many as completely dissimilar -- even competing -- activities when, in fact, they are in many ways quite similar. Both activities entail the exploration of an environment hostile to man. Both have that magic element of excitement that accompanies most of man's attempts to push back the frontiers. Both call for ingenuity and new technology, and both, unfortunately, are very expensive. It is especially for this last reason that it is gratifying to see attention being paid to utilizing the techniques developed in space exploration for furthering our understanding of the sea.

The great contributions made so far to our understanding of the dynamics of the sea have come primarily from data obtained by oceanographic research ships. The advent of the space era does not remove the need for scientists to go to sea -- hopefully this will never be removed. It does, however, provide us for the first time the ability to "see" great reaches of the ocean at one time and to consider features and processes on an almost global scale. The oceanographer, enamoured as he is with his ships and his work at sea, has been slow, even reluctant at times, to capitalize on the space program to provide information on the sea that could not even be considered a decade ago. But for many oceanographers this earlier reluctance has given way to an eagerness to get instruments up where they can see more and to develop new instrumentation to provide new knowledge of the sea. Earth orbiting satellites can fill this need.

The Joint NOAA-NASA-NAVY Conference held on Key Biscayne, Miami, Florida, October 6-8, 1971, brought together scientists from a broad range of specialities to look specifically at the use of remote sensors on spacecraft for providing new and needed information on the upper surface of the ocean. It was an exciting conference to attend. It should be equally so to read for those who could not be there in person.

The Atlantic Oceanographic and Meteorological Laboratories were pleased to act as host organization and to publish the Proceedings as one of its technical reports.

Harris B. Stewart, Jr.
Director
Atlantic Oceanographic and
Meteorological Laboratories

TABLE OF CONTENTS

VOLUME I

TABLE OF CONTENTS (Cont'd)

TABLE OF CONTENTS (Cont'd)

VOLUME II

PROGRAM COMMITTEE

John R. Apel, Chairman, NOAA/AOML
Jerome D. Rosenberg, NASA/Headquarters
John W. Shermann, III, Navy/SPOC
H. Ray Stanley, NASA/Wallops Station
Martin J. Swetnick, NASA/Headquarters
Friedrich O. Vonbun, NASA/GSFC

CONFERENCE ATTENDEES

Dr. John R. Apel
NOAA/AOML
901 South Miami Avenue
Miami, Florida 33130

Dr. Donald Barrick
Battelle Memorial Institute
505 King Avenue
Columbus, Ohio 43201

Mr. John Berbert
NASA/Goddard Space Flight Center
Greenbelt, Maryland 20771

Mr. Harold Black
The Johns Hopkins University
Applied Physics Laboratory
Silver Spring, Maryland 20910

Mr. Paul Bouchard
DBA Systems
Melbourne, Florida 32901

Dr. Saul Broida
Coast Guard Headquarters
200 Seventh Street, SW
Washington, D.C. 20591

Mr. Ronald L. Brooks
Wolf Research & Development Corp.
Clark & Vine Streets
Pocomoke City, Maryland 21851

Mr. Walter E. Brown, Jr.
Senior Scientist
Jet Propulsion Laboratory
4800 Oak Grove Drive
Pasadena, California 91103

Mr. Bud Burke
Sea-Flight Corporation
940 S.W. 34th Street
Ft. Lauderdale, Florida 33315

Mr. George Bush
Johns Hopkins University, APL
Silver Spring, Maryland 20910

Mr. H. Michael Byrne
Woods Hole Oceanographic Institute
Woods Hole, Mass. 02543

Mr. Bernard Chovitz C111
NOAA/National Ocean Survey
Rockville, Maryland 20852

Dr. Leroy M. Dorman
NOAA/AOML/MG&G Laboratory
901 South Miami Avenue
Miami, Florida 33130

Mr. James K. Estes
USAF Aeronautical Chart & Info. Center
2nd and Arsenal Streets
St. Louis, Missouri 63118

Dr. D. Michael Fubara
Battelle Memorial Institute
505 King Avenue
Columbus, Ohio 43201

Dr. E. M. Gaposchkin
Smithsonian Astrophysical Observatory
60 Garden Street
Cambridge, Mass. 02138

Mr. Thomas W. Godbey
General Electric Company
Utica, New York 13503

Lt. (JG) Lowell Goodman
NOAA/National Ocean Survey, AMC
439 West York Street
Norfolk, Virginia 23510

Mr. Alan Greene
Raytheon Company
Boston Post Road
Wayland, Mass. 01778

Mr. George Hadgigeorge
AFCRL/LWG
L. G. Hanscom Field
Bedford, Mass. 01778

Mr. Robert Harrington
Teledyne/Ryan Aeronautical
8650 Balboa Avenue, P.O. Box 311
San Diego, Calif. 92112

Dr. Klaus Hasselmann
Woods Hole Oceanographic Institution
Woods Hole, Mass. 02543

Dr. George S. Hayne
Research Triangle Institute
P. O. Box 12194

Mr. Craig Hooper
Office of Programs
NOAA/Environmental Res. Laboratories
Boulder, Colorado 80302

Mr. Edward F. Hudson
Raytheon Company
Boston Post Road
Wayland, Mass. 01778

Mr. Albert C. Jones
Space Division
North American Rockwell SL92
12214 Lakewood Boulevard
Downey, Calif. 90241

Dr. W. Linwood Jones
NASA/Langley Research Center
Hampton, Virginia 23365

Mr. Joseph Kaye
Chief of Materiel, U.S. Navy
P.M. 16-22
Washington, D.C. 20360

Mr. Douglas S. Kimball
Westinghouse Defense & Space Center
Mail Stop 337
Baltimore, Maryland 21203

Dr. Kumar Krishen
Lockheed Electronics Co.
16811 El Camino Real
Clearlake City, Texas 77058

Mr. Clifford Leitao
NASA Wallops Station
Wallops Island, Virginia 23337

Dr. Alden Loomis
Jet Propulsion Laboratory
4800 Oak Grove Drive
Pasadena, Calif. 91103

Mr. Thomas J. Lund
Teledyne/Ryan Aeronautical
8650 Balboa Avenue, P.O. Box 311
San Diego, Calif. 92112

Dr. Charles Lundquist
Smithsonian Astrophysical Observatory
60 Garden Street
Cambridge, Mass. 02138

Mr. Paul A. Lux
Teledyne/Ryan
P.O. Box 311
San Diego, Calif. 02138

Dr. Mark M. Macomber
Naval Oceanographic Office
Director, Gravity Div. Code 8300
Washington, D.C. 20390

Dr. Chreston Martin
Wolf Research & Development Corp.
6801 Kenilworth Avenue
Riverdale, Maryland 20840

Mr. George Maul
NOAA/AOML/Physical Oceanographic Lab.
901 South Miami Avenue
Miami, Florida 33130

Mr. Robert W. McCaslin
NOAA/National Weather Service
Silver Spring, Maryland 20910

Dr. William McLeish
NOAA/AOML/Sea-Air Interaction Lab.
461 South Miami Avenue
Miami, Florida 33130

Dr. Lee S. Miller
Research Triangle Institute
P. O. Box 12194
Research Triangle Park, N. C. 27709

Dr. Richard K. Moore
Space Tech. Building
University of Kansas
Irving Hill Road, West Campus
Lawrence, Kansas 66044

Mr. A. George Mourad
Battelle Memorial Institute
505 King Avenue
Columbus, Ohio 43201

Prof. Ivan Mueller
Dept. of Geodetic Science
Ohio State University
164 West 19th Avenue
Columbus, Ohio 43210

Mr. Fred Nathanson
Technology Service Corporation
8555 16th Street
Silver Spring, Maryland 20910

Mr. J. Barry Oakes
Applied Physics Laboratory
8621 Georgia Avenue
Silver Spring, Maryland 20910

Prof. Willard J. Pierson, Jr.
Dept. of Meteorology & Oceanography
New York University
New York, New York 10453

Dr. Henry Plotkin
Code 520
NASA Goddard Space Flight Center
Greenbelt, Maryland 20770

Mr. Robert F. Pontzer
Teledyne/Ryan Aeronautical
1501 Wilson Boulevard, Suite 900
Arlington, Virginia 22209

Prof. Richard H. Rapp
Ohio State University
164 W. 19th Avenue
Columbus, Ohio 43210

Mr. Jerome Rosenberg
OSSA-NASA Headquarters
Washington, D. C. 20546

Mr. Duncan Ross
NOAA/AOML/Sea-Air Interaction Laboratory
461 South Miami Avenue
Miami, Florida 33130

Mr. Laurence Rossi
NASA/Wallops Station
Code 221
Wallops Island, Virginia 23337

Mr. Normand A. Roy
Wolf Research & Development Corp.
Clark & Vine Streets
Pocomoke City, Maryland 21851

Mr. Phillip Schwimmer
Dept. of Defense
DIA MC
The Pentagon
Washington, D.C. 20301

Mr. Alan Shapiro
E.O. Hulburt Center for Space Research
Naval Research Laboratory
Washington, D.C. 20390

Mr. John W. Sherman
Spacecraft Oceanography Project
Naval Research Laboratory
Washington, D. C. 20390

Dr. Miriam Sidran
NOAA/Natl. Marine Fisheries Service
Southeast Fishery Center
75 Virginia Beach Drive
Miami, Florida 33149

Dr. Joseph Siry
NASA/Goddard Space Flight Center
Greenbelt, Maryland 20771

Dr. David E. Smith
Code 553
NASA/Goddard Space Flight Center
Greenbelt, Maryland 20771

Mr. Sam Smith
Naval Weapons Laboratory
Code KA0
Dahlgren, Virginia 22448

Mr. H. Ray Stanley
NASA/Wallops Island Station
Wallops Island, Virginia 23337

Dr. Harris B. Stewart, Jr.
Director, NOAA/AOML
901 So. Miami Avenue
Miami, Florida 33130

Mr. William E. Strange
Computer Science Corp.
6520 Columbia Pike
Falls Church, Virginia 22041

Dr. Alan E. Strong
NOAA/NESS-ESG
3737 Branch Avenue
Washington, D.C. 20031

Dr. Wilton Sturges
Dept. of Oceanography
University of Rhode Island
Kingston, R. I. 02881

Dr. Martin Swetnick
OSSA/NASA Headquarters
Washington, D. C. 20546

Prof. Manik Talwani
Lamong-Doherty Geological Observatory
Palisades, New York 10964

Dr. Byron Tapley
University of Texas at Austin
227 Taylor Hall
Austin, Texas 78712

Capt. Raymond W. Thompson
NASA Headquarters
Code W
Washington, D. C.

Cdr. John Tuttle
Chief of Materiel, U.S. Navy
P.M 16-22
Washington, D. C. 20360

Dr. Fredrich O. Vonbun
Code 550
NASA/Goddard Space Flight Center
Greenbelt, Maryland 20771

Mr. Edward J. Walsh
NASA/Wallops Island Station
Wallops Island, Virginia 23337

Dr. George C. Weiffenbach
Smithsonian Astrophysical Observatory
60 Garden Street
Cambridge, Mass. 02138

Dr. Willard Wells
Tetra Tech., Inc.
360 Halstead
Pasadena, Calif. 91107

Mr. Ralph Willison
The Johns Hopkins University
Applied Physics Laboratory
8621 Georgia Avenue
Silver Spring, Maryland 20910

Mr. Benjamin Yaplee
E.O. Hulburt Center for Space Research
Naval Research Laboratory
Washington, D.C. 20390

Mr. Steven Yionoulis
The Johns Hopkins University
Applied Physics Laboratory
8621 Georgia Avenue
Silver Spring, Maryland 20910

Mr. Bernard D. Zetler
NOAA/AOML/Physical Oceanog. Lab.
901 South Miami Avenue
Miami, Florida 33130

INTRODUCTION

The impetus for the NOAA-NASA-NAVY Conference on Sea Surface Topography from Space was largely due to two forthcoming spacecraft that bear on the problem: SKYLAB and GEOS-C. Each vehicle is to carry an X-band radar altimeter; SKYLAB in addition has a rather comprehensive sensor package designed for observing earth resources in the visible, infrared, and microwave frequency regions.

The Conference was devoted to the subjects of geodesy and oceanography, the two topics being intimately related through the distortions that a dynamic, moving ocean introduces on the geoid as measured with a precision altimeter on an accurately tracked satellite. In a very real sense, the geodescist's noise is the oceanographer's signal. This relationship was recognized and exploited at the conference held at Williams College in August 1969, the report of which recommended the development of a 10-cm precision altimeter for space use, among other things.

As defined for purposes of the present Conference, "sea surface topography" denotes ocean surface features ranging from capillary waves through gravity waves, swell, setups, geostrophic slopes, geoidal undulations, and tides, in order of increasing wavelength. The meeting addressed itself to the problems of measuring these undulations from spacecraft or aircraft using radar or laser instrumentation. As such, it brought together, at Key Biscayne, Florida, specialists in geodesy, oceanography, space science and space technology. The interdisciplinary features of the problem proved especially stimulating to the attendees, not only because of the implications which the subject has for each discipline, but because of the social relevance (to use a current shibboleth) which the research possesses. It appears possible, for instance, to ultimately use radar systems in space to provide all-weather monitoring and prediction of surface winds, sea state, current systems, and perhaps even hurricanes and storm surges. These functions are probably a decade off, but the impact on the welfare of man is obvious.

John R. Apel
Chairman

GRAVIMETRICALLY DETERMINED GEOID IN THE WESTERN NORTH ATLANTIC

Manik Talwani, Herbert R. Poppe, and Philip D. Rabinowitz
Lamont-Doherty Geological Observatory of
Columbia University
Palisades, N. Y. 10964

1. INTRODUCTION

We describe in this paper a detailed gravimetric geoid for the western North Atlantic. In the past it has not been possible to obtain a gravimetric geoid in ocean areas because of scarcity of gravity data. However, since the nineteen sixties, the development of surface ship gravimeters has led to the accumulation of considerable amounts of sea gravity data, and it is now possible to make the first detailed determination of a gravimetric geoid over an extended oceanic area.

The success in the determination of the Earth's gravitational field from data based on satellite observations has been so spectacular that one must enquire whether sea gravity data can provide any additional useful information. Gaposchkin and Lambeck (1970, 1971) describe the Earth's gravitational field to the sixteenth order and degree from satellite and terrestrial data (1969 Smithsonian Standard Earth). A solution to the sixteenth order and degree represents wavelengths longer than about 2500 km. Gaposchkin and Lambeck state that "comparison with surface gravity indicates that up to 10,10 the satellite solution is about as good as can be expected but that some of the higher order terms are poorly determined. The terms between degrees 11 and 16 are determined largely from the surface-gravity data." A solution to the tenth order and degree represents wavelengths larger than about 4000 km. Hence it is clear that in order to provide information for wavelengths smaller than a few thousand kilometers it is necessary to use surface gravity data.

There is the further question whether the gravity field at these smaller wavelengths can make any significant contribution to the geoid undulations. Statements exist in the published literature to the effect that the geoid height is known to a few meters. Such statements are, of course, only concerned with geoid undulations of long wavelengths. As we shall demonstrate in this paper, undulations of the geoid with wavelengths of a few hundred kilometers can have amplitudes of a few tens of meters. Thus, for the complete description of the geoid it is essential to utilize surface gravity data.

The gravity field described by the range of wavelengths from a few tens of kilometers to a few thousand kilometers is of special interest to geophysicists because it reflects, in part, density inhomogeneities in the Earth's upper mantle. The location, nature, and magnitude of the density anomalies in the upper mantle will undoubtedly help in resolving the causes of the motion of the "plates" comprising the Earth's lithosphere. While the geometry of plate motions is beginning to be understood, the causes of these motions are still quite obscure.

There are reports of plans to map the geoidal undulations in the oceanic areas by radar altimeters on the Skylab and the GEOS-C satellites. A major error in the altimeter measurement will arise from the uncertainty in the position of the satellites. However, the position uncertainties are smallest for small wavelengths and the usefulness of the altimeter will be primarily for the determination of short wavelength undulations of the geoid. In order to calibrate the altimeter and to test its performance, or even to determine optimum locations at which the experiment should be performed, it is absolutely essential to know the geoid undulations at the same locations by independent means. However, no such geoid maps exist over the oceanic areas. This study, although preliminary in nature is the only one to date that provides detailed information about the geoid in an oceanic area. The study will have to be refined on the basis of newer information which is available but which has not been incorporated.

When the radar altimeter experiment has been refined to the point where geoidal undulations to the accuracy of a few tens of centimeters can be determined, a comparison with a gravimetrically determined geoid determined to the same accuracy could be of great use to physical oceanographers. Differences between the two geoids will be related primarily to currents and tides, etc. in the oceans.

2. SEA GRAVITY DATA IN THE WESTERN NORTH ATLANTIC

There are two principal problems in the utilization of existing sea gravity data for the construction of a gravimetric geoid. One problem is that the accuracy of older surface ship gravity data is poor; the second arises from the uneven areal coverage of gravity measurements. We consider these two problems in some detail below.

Gravity values obtained from submarine pendulum measurements in the western North Atlantic have been given by Vening Meinesz (1948) and Worzel (1965). The locations of the pendulum measurements are given in Figure 1. These values are accurate to a few milligals but the density of measurements is insufficient for the present study.

The locations of surface ship gravity measurements are also shown in Figure 1. These measurements were made in the period 1961-1971. The Lamont-Doherty measurements made aboard research vessels VEMA and ROBERT D. CONRAD, as well as the Dutch measurements aboard H. NETH. M. S. SNELLIUS, utilized the Graf Askania sea gravimeters. The Woods Hole measurements aboard research vessel CHAIN used the LaCoste Romberg gimbal mounted gravity meter in earlier measurements, and the vibrating string gravimeter in later measurements.

The accuracy of gravity measurements has increased steadily since the beginning of surface ship measurements. The earlier measurements seldom had an accuracy of better than 5 mgal. Under poor sea conditions the errors were as large as 20 mgal. The latest measurements almost always have an accuracy of better than 5 mgal. When

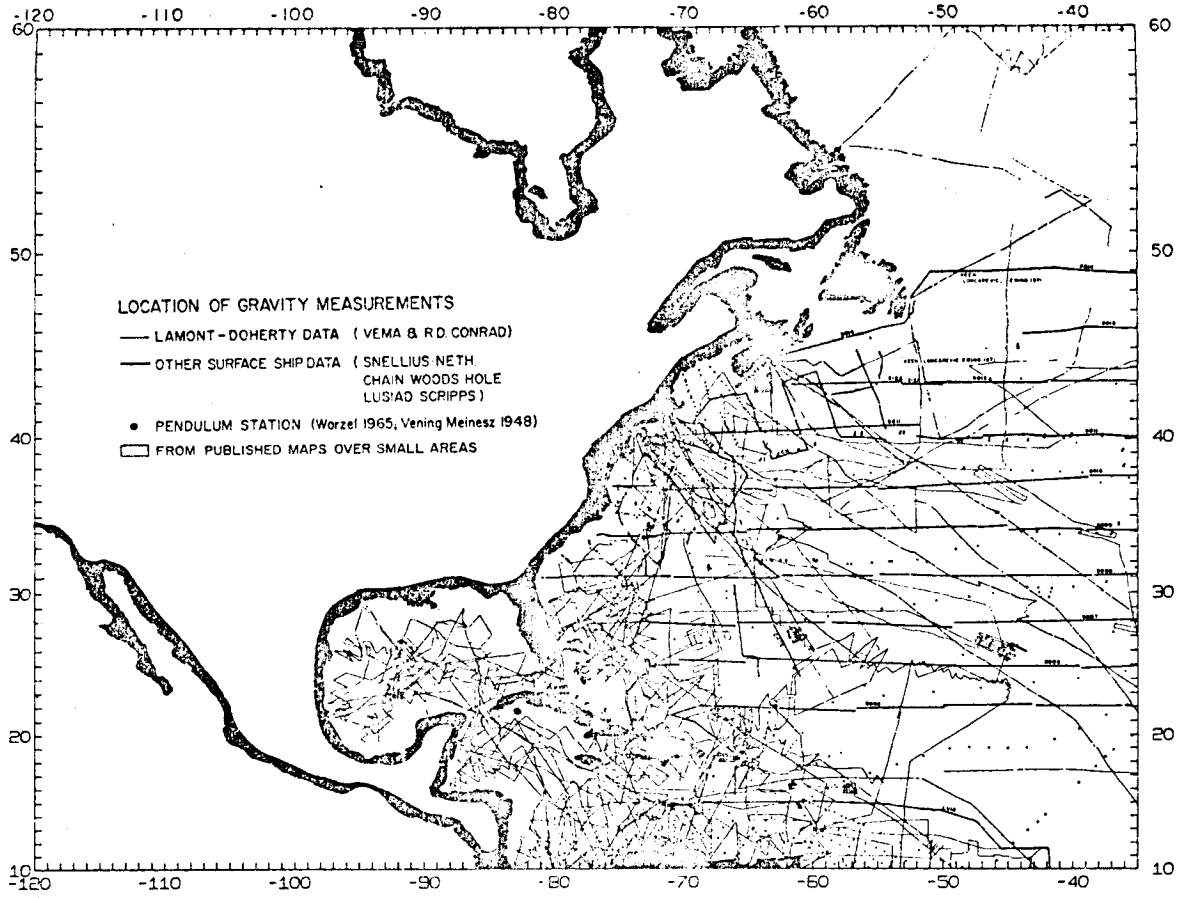

Figure 1. Location of gravity measurements in the western North Atlantic. Woods Hole data obtained on R/V CHAIN (labeled CH) are described by Emery et al. (1970). Data aboard H. Neth. M. Ship SNELLIUS (labeled S005, S006, etc.) were obtained as part of the "Navado" project. Data obtained during Scripps Institution's expedition "Lusiad" (labeled LU18) are described by Caputo et al. (1964). Small areas where published gravity maps exist (Keen, Loncarevic and Ewing, 1971; Goodacre, 1964; Orlin, 1963; and Talwani, 1959) are indicated. In parts of Gulf of Mexico where the Lamont-Doherty data average is poor, we utilized the free-air gravity map of Dehlinger and Jones (1965). Also utilized were values on the shelf west of Florida made available to us by ACIC, St. Louis, Missouri.

great care is taken, especially with navigation errors, the measurement error can be reduced to the level of 1 mgal or so.

In using data of varied accuracy, several alternative procedures are possible. One can discard all the older data which is considered less accurate. Such a procedure would seriously reduce the number of gravity measurements used for the study. A second procedure is to incorporate all data irrespective of accuracy. This procedure was followed by Talwani and LePichon (1969) in constructing averages over 1x1° and 5x5° squares in the Atlantic Ocean. However, the accuracy of the averages is certainly degraded by including data of low accuracy.

Substantial improvements in obtaining the overall gravity field from the gravity measurements can be made if advantage can be taken of the following two facts: 1. The errors in gravity observations are largely systematic rather than random, and 2. Short wavelength variations in gravity are correlated with topographic variations.

The errors in gravity measurements are influenced strongly by sea condition, and the ship's heading with respect to sea and swell. Most of the measurements in the western North Atlantic have been made by Graf Askania sea gravimeters. Measurements made with this meter are subject to the cross coupling error (LaCoste and Harrison, 1961). This error was a principal reason for the inaccuracies of surface ship gravity measurements until about 1965 when cross coupling computers (Talwani et al., 1966) which provide real time cross coupling correction came into regular use. Figure 2 shows how the value and sign of the cross coupling error varies with ship's heading (with respect to sea and swell) and Figure 3 shows how, at a constant heading, the value of the cross coupling error changes slowly as the sea state changes. Although the magnitudes of the errors in some of the examples in these figures are atypically large, having been obtained under rough sea conditions, nevertheless these figures serve to illustrate the manner in which these errors change. In cases when one ship's track is crossed by other ship tracks, recognition

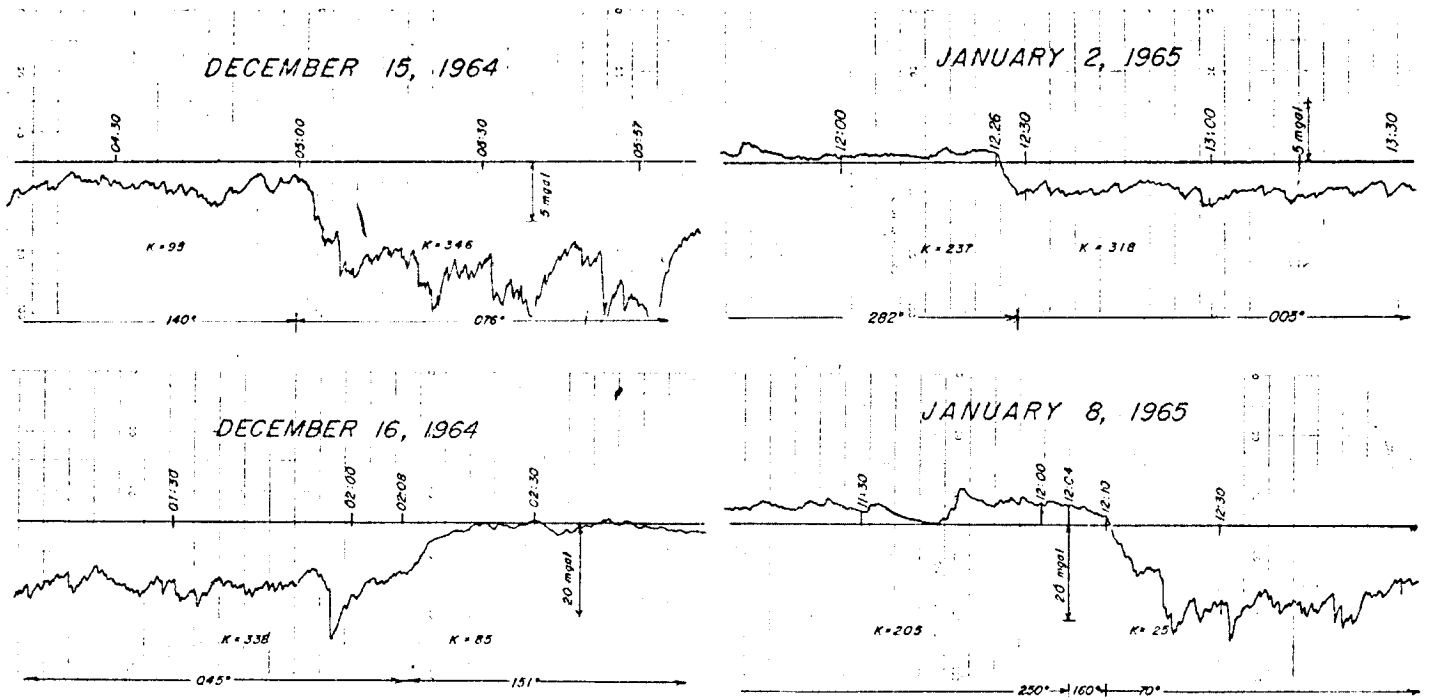

Figure 2. The cross coupling error, a principal error in measurements made with the Graf Askania sea gravimeter depends on the angle K between ships' heading and the direction of sea and swell. For the cross coupling records obtained during four different days, the change in magnitude and/or sign are clearly correlated with change in ship heading indicated at the bottom of each record section. The times in hours and minutes are indicated at the top of each record section. All the records except the one on January 2 were obtained in exceptionally rough weather. Filtering also reduces the short frequency (less than 1 cycle per minute) cross coupling noise. The systematic nature of the cross coupling error makes it easier to adjust uncorrected data. Data obtained later than 1965 used on line analog computers which eliminate the cross coupling error in real time (after Talwani et al., 1966).

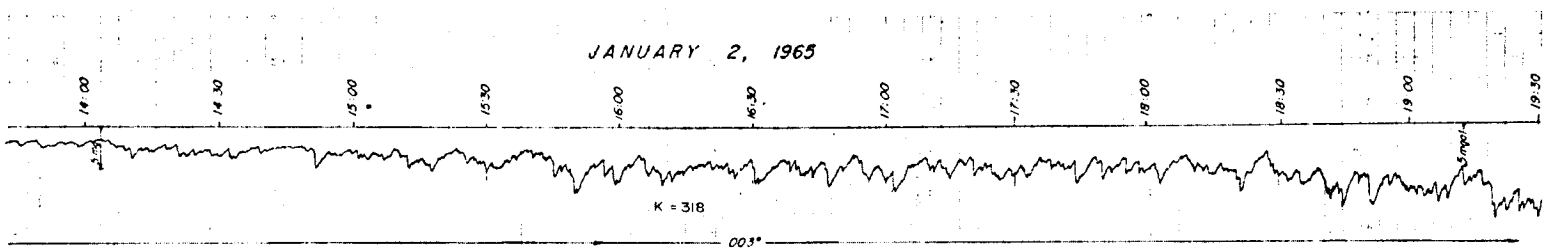

Figure 3. The gradual increase of cross coupling error as sea state became greater. This relatively slow change in cross coupling error also makes it easier to adjust uncorrected data with the help of corrected measurements made along intersecting tracks. (After Talwani et al., 1966).

of the manner in which the errors change allow us to apply adjustments to measured ship values. Thus, for instance, where a correction is determined at one point along a track segment (from an intersecting track of high accuracy), the same correction can be applied for the entire track segment where course remains unaltered. The earlier gravity measurements have been adjusted in this manner. We feel that this adjustment has been extremely important in increasing the overall accuracy of the determination of the gravity field.

The correlation of the short wavelength gravity undulations with topography is demonstrated in Figures 4 and 5. We see that this correlation is good not only in an area of the Mid-Atlantic Ridge where in an area of small thickness of sediments one would expect such a correlation, but, surprisingly, also in an area east of the Lesser Antilles where there are large anomalies due to subbottom density contrasts. The bottom topography in the North Atlantic is known in much greater detail through many extensive surveys, than the gravity field is. The high degree of correlation between short wavelength gravity and topographic variations allows us to interpolate gravity values between observation points on the basis of topography.

We have utilized knowledge of the systematic manner in which errors in gravity measurements change, as well as the knowledge of correlation of gravity with topography to construct contour maps of free-air gravity in the western North Atlantic south of 45°, the Caribbean Sea and the Gulf of Mexico (Rabinowitz and Talwani, 1969; Talwani and Poppe, 1968). These maps have a contour interval of 25 mgal but a large number of spot measurements are given which help in the interpolation of values between contours where the contours are widely spaced. Spot measurements are also given for maxima and minima.

The gravity contour maps were used to obtain free-air averages over 1x1° squares in the following manner. In areas where the gravity variations are relatively small and the distance between contours is large, each 1x1° square was divided into nine smaller squares. The values at the mid point of the smaller squares were visually

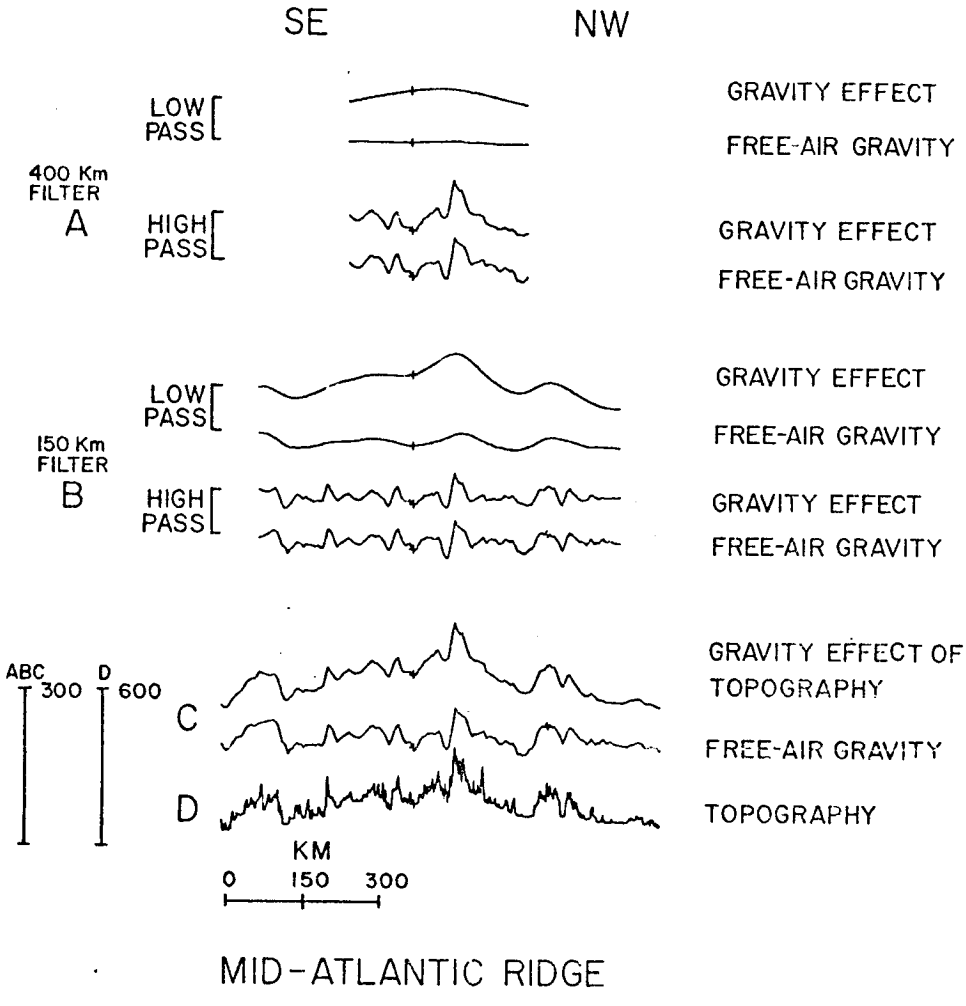

Figure 4. The bottom curve gives the topography over a section of the north Mid-Atlantic Ridge. (Scale D is in meters) The measured free-air gravity curve is immediately above the topography curve (Scales A, B, and C are in milligals). The gravity effect of topography is computed using a density contrast of 2.67-1.03 g/cm^3. Both the free-air gravity and the gravity effect of topography is filtered, using two different Gaussian filters of widths 150 km and 400 km. The filters are designed in such a way that the wavelength λ of unit amplitude after being filtered through the low pass Gaussian filter of width w has an amplitude $\exp[(-.55(w^2/\lambda^2)]$. For example for λ=2w and w/2 the respective filtered amplitudes are .96 and .11. We notice that for wavelengths of the order 400 km the free-air gravity can be predicted well from topography in the region of the Mid-Atlantic Ridge.

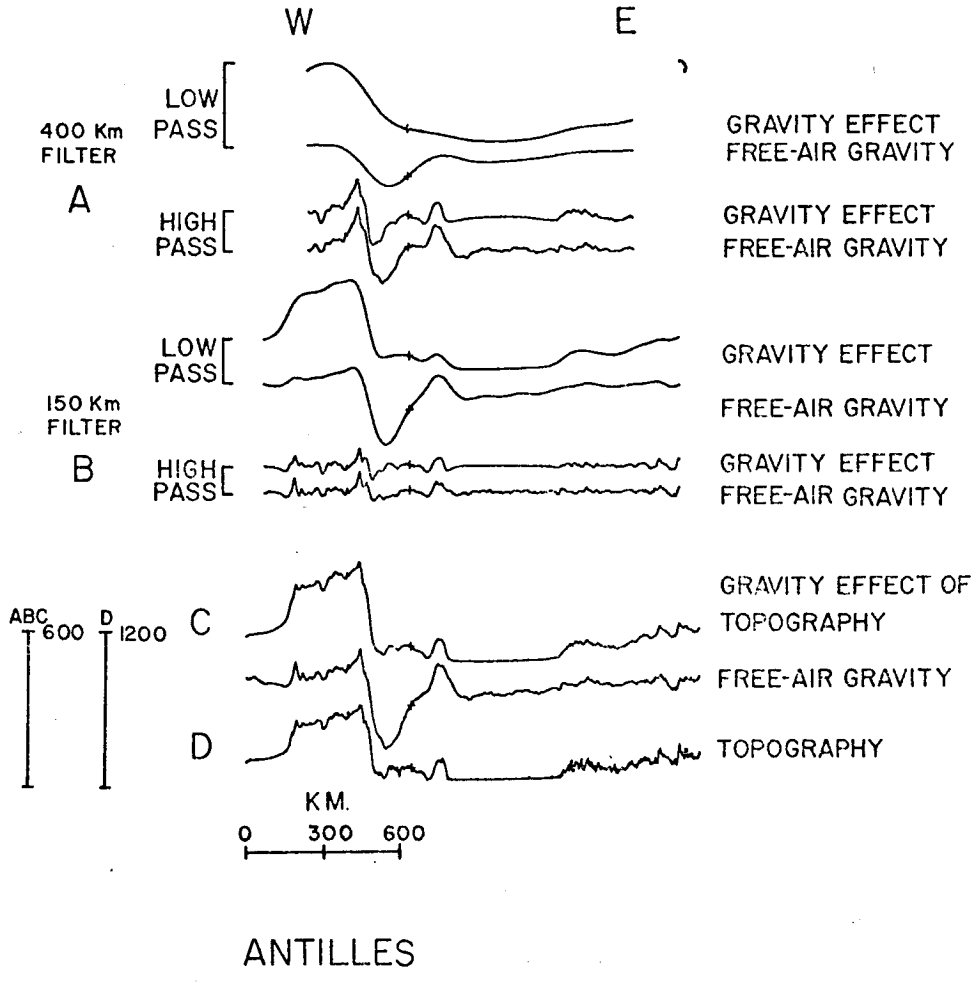

Figure 5. West-east profiles through the Lesser Antilles. For description of curves, see Figure 4. Even in this area of large subbottom density inhomogeneities gravity anomalies with wavelengths up to a few hundred kilometers can be predicted from topography. This relationship between gravity and topography enables us to interpolate free-air anomalies between two neighboring profiles if depth values are known between the two profiles.

interpolated from the contour map and averaged to give a value for the 1x1° square. For areas such as the Caribbean the above procedure was not practical since the gravity values change too rapidly. In such areas the contours as well as the locations of spot values were digitized and computer programs were written to interpolate the gravity values at the center of 10x10' squares. These values were averaged to obtain free-air gravity averages over 1x1° squares.

Figure 6 gives the free-air gravity values averaged over 1x1° squares. The values over ocean areas were obtained by the methods outlined above. In ocean areas, as for example north of 50°, the number of available gravity measurements were insufficient to allow us to draw contours. In such areas we have used the unadjusted free-air values to obtain averages over 5x5° squares. The description of the gravity field in these areas is considered poor.

We have not been able to utilize data from some of the most recent cruises whose tracks are shown in Figure 1. Hence the averaged values in Figure 6 over ocean covered areas are subject to revision. The 5x5° values in particular might be revised drastically on the basis of newer data.

The 1x1° free-air gravity values of Figure 6 are contoured at an interval of 20 mgal in Figure 7. Contours are dotted in the 5x5° square areas.

3. LAND GRAVITY DATA

We have obtained free-air averages on land from published data. Values in southeast Cuba were averaged from Shurbet and Worzel (1957). The values in Mexico and in other parts of Cuba were obtained from a Russian Bouguer gravity map of North America published in 1968 (conversion from Bouguer to free-air anomalies were made by using regional elevations). After having made the calculations in this study we became aware of the compilation of Woollard et al. (1969) for Mexico. Using the poorer Russian data in Mexico constitutes the biggest source of error in this study.

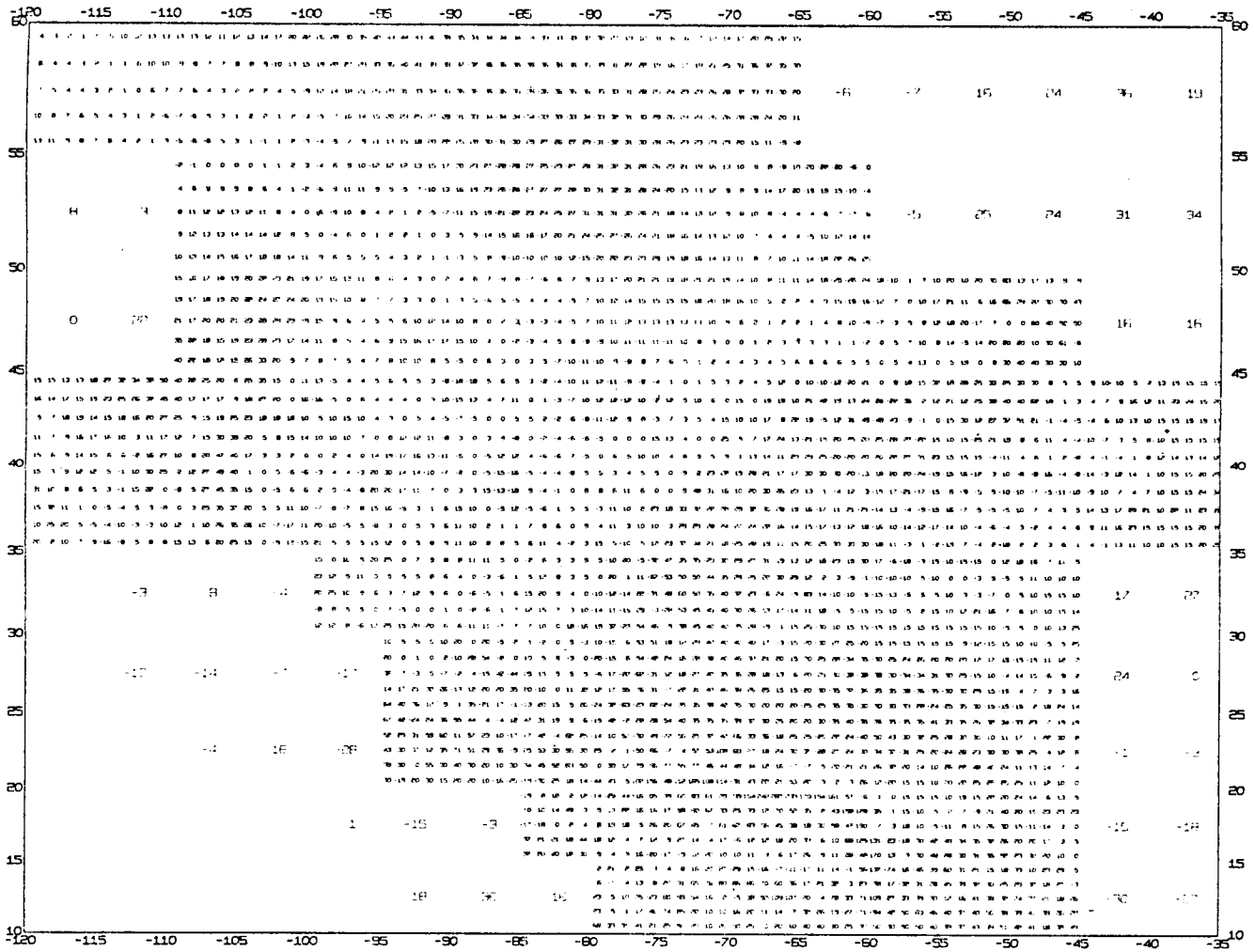

Figure 6. Gravity data averaged over 1x1° squares in the western North Atlantic and North America. Where data were available in fewer than half of the twenty-five 1x1° squares of a 5x5° square, the data are averaged for the 5x5° squares.

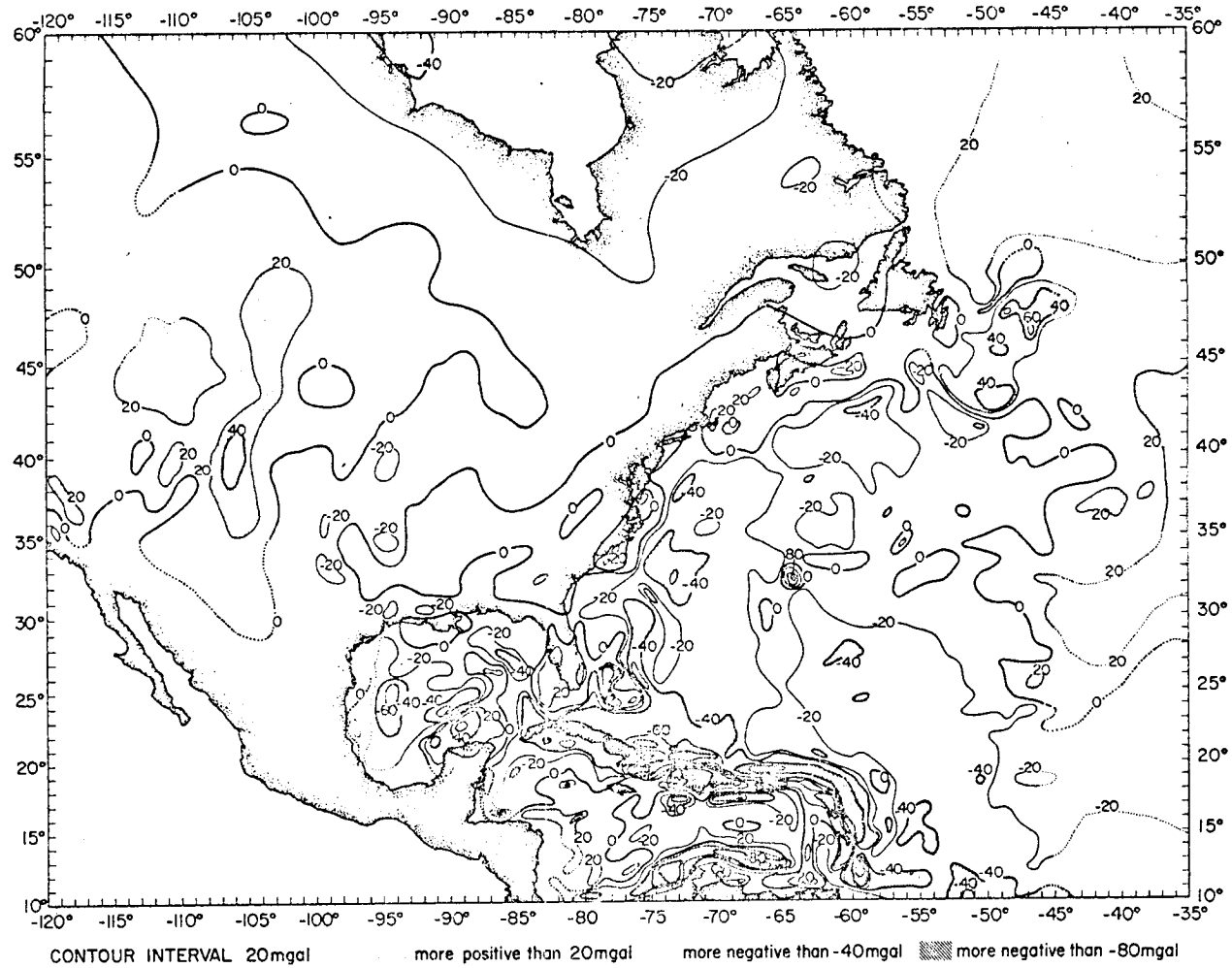

Figure 7. The 1x1° free-air gravity values of Figure 6 are contoured at an interval of 20 mgal. Contours are dotted in the 5x5° square areas.

Values in Canada obtained by the Earth Physics branch of the Department of Energy, Mines and Resources were taken from Walcott (1970). In Walcott's study, free-air gravity contours were based on averages over 1x2° squares. The values in Canada in Figure 6 have been obtained by interpolation from the contours. The values in the United States were obtained principally from a compilation by Strange and Woollard (1964).

4. METHOD USED IN CONSTRUCTION OF GEOID MAPS

Basic Approach

We have employed Stokes theorem for obtaining geoid heights. The free-air anomalies averaged over 1x1° (and some 5x5° squares) as shown in Figure 6, were utilized. Outside the area in which anomalies are given, we assume that the gravity field is determined by the spherical harmonic coefficients for the geopotential to order and degree 16 from the combination solution of Gaposchkin and Lambeck (1971). In other words, for the near zones we used the averaged free-air anomalies; for distant areas we used gravity values from Gaposchkin and Lambeck's combination solution.

The actual construction of the geoid is as follows. Geoidal heights were determined from Gaposchkin and Lambeck's combination solution in the western North Atlantic and over North America. The geoidal heights have been contoured at 5 m intervals and are shown in Figure 8. We term this geoid the "G and L" geoid for the purpose of this paper. Similarly, the spherical harmonic coefficients were used to compute gravity values averaged over 1x1° squares for the western North Atlantic. These "G and L" gravity values were subtracted from the free-air gravity values averaged over 1x1° squares (surface data shown in Fig. 6). The gravity differences, also expressed as 1x1° squares were then used to compute a "difference" geoid (Fig. 9). The "1x1° difference" geoid represents the additional information provided by the 1x1° surface gravity data. The "1x1° difference" geoid is then added to the "G and L" geoid to obtain a "1x1°" geoid (Fig. 10). The "1x1°" geoid uses 1x1° surface gravity data in the area of the maps, but gravity data from Gaposchkin and Lambeck's combination solution outside the area of the maps. The practical advantage of the above procedure

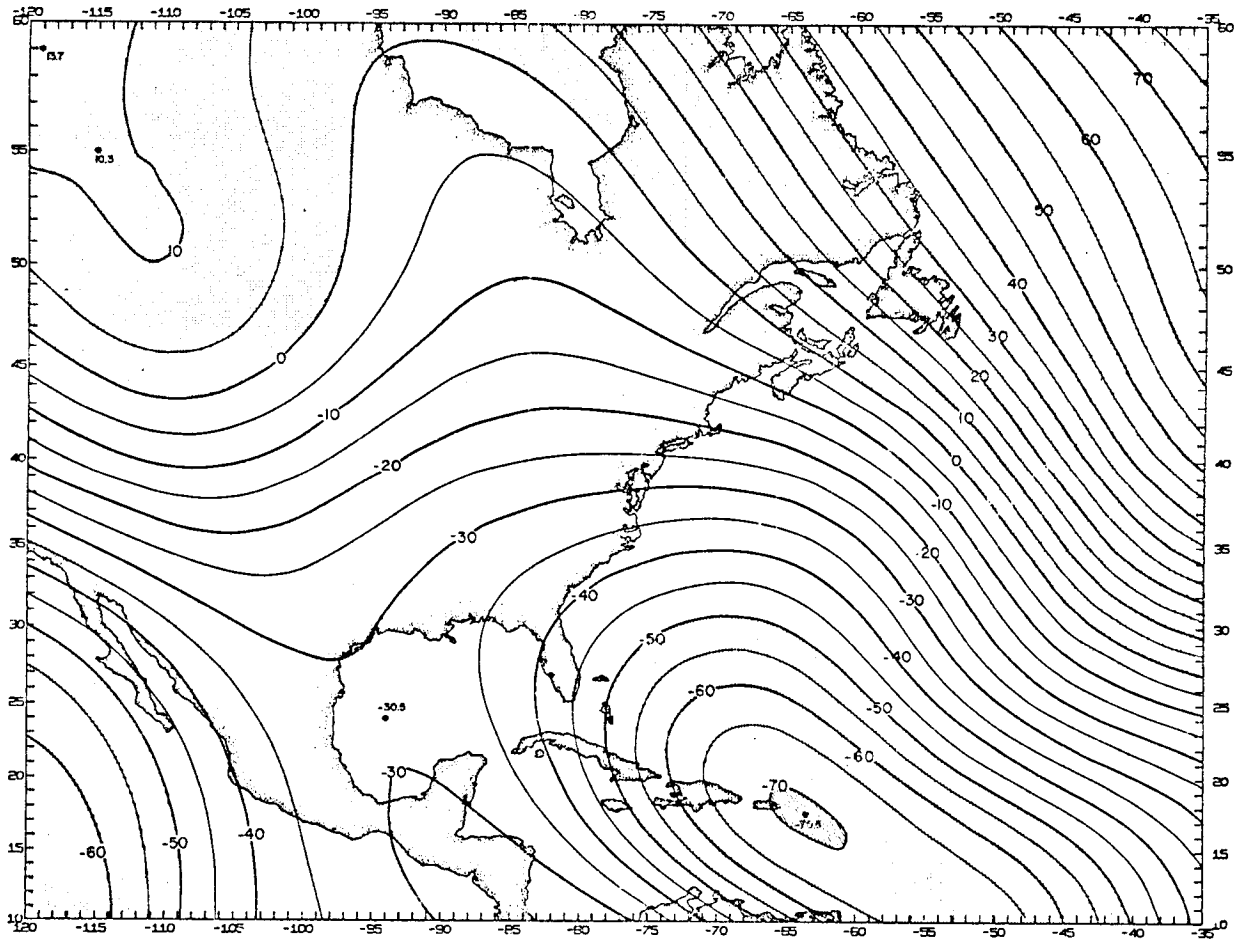

Figure 8. Geoid obtained from the spherical harmonic coefficients of degree and order 16 given by Gaposchkin and Lambeck (1971) referred to an ellipsoid of flattening 1/297.0. This geoid is called the "G and L" geoid in this study. Positive areas are stippled. Areas between -50 m and -70 m are shaded by vertical lines and areas more negative than -70 m by slant lines.

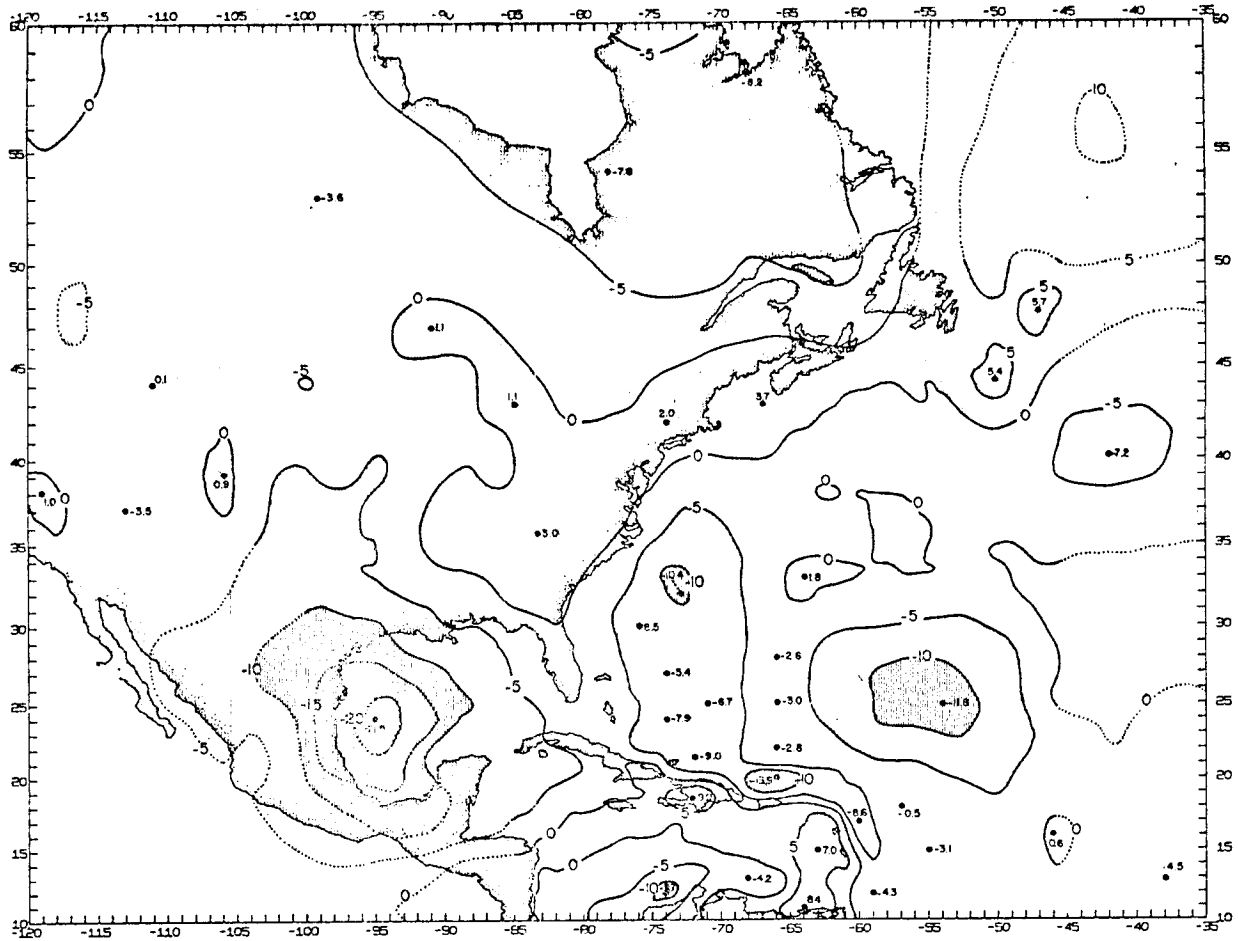

Figure 9. The "1x1° difference" geoid. From the gravity values in Figure 6 were subtracted the values of gravity obtained by using the spherical harmonic coefficients to degree and order 16 given by Gaposchkin and Lambeck (1971) and referred to an ellipsoid of flattening 1/297.0. The resultant values were used in a Stokes integration to give the "1x1° difference" geoid. Positive areas are stippled. Areas between -5 m and -10 m are shaded by vertical lines; areas more negative than -10 m are shaded by denser vertical lines. Dotted contours are in areas of poor gravity control.

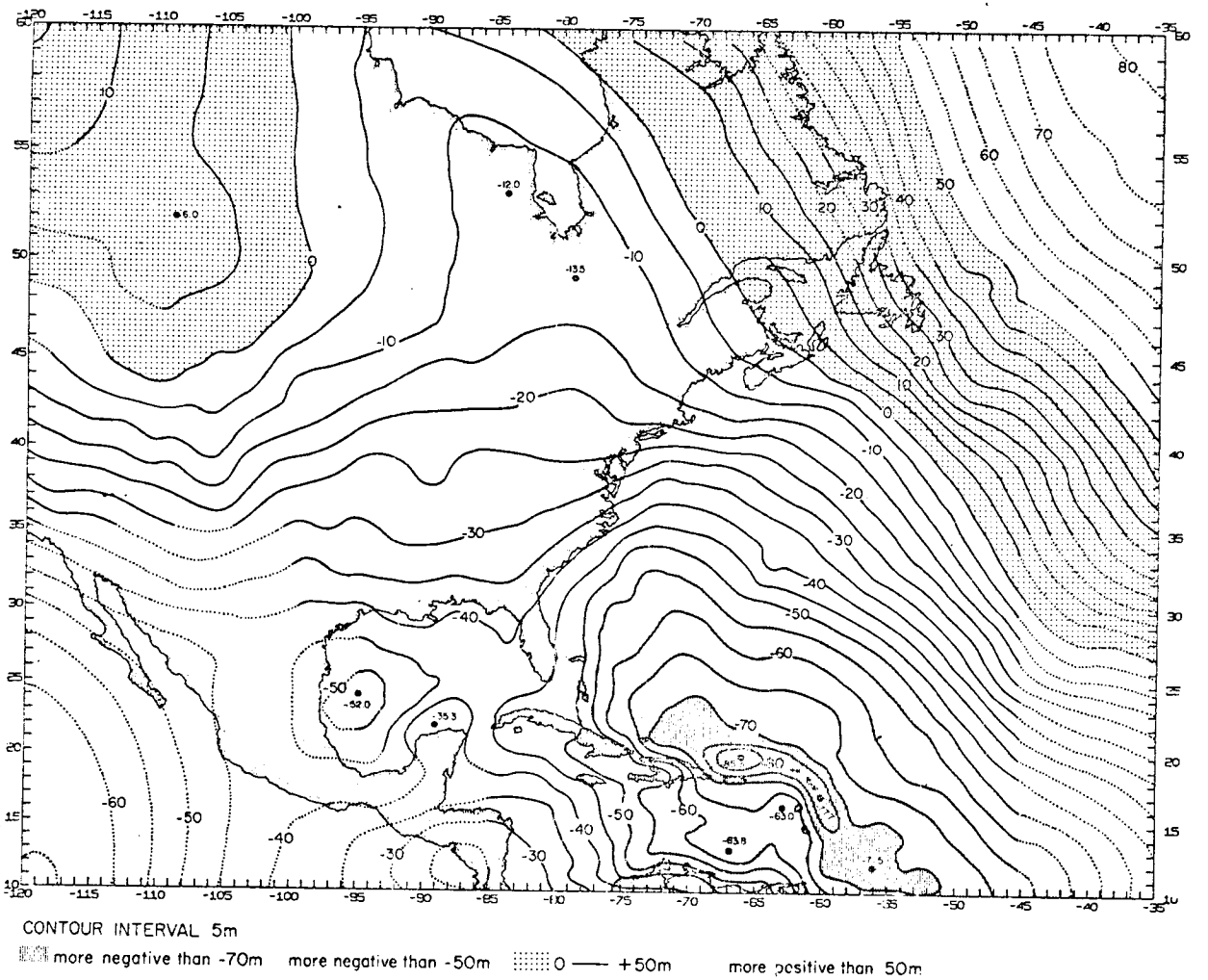

Figure 10. The "1x1°" geoid obtained by adding the "1x1° difference" geoid of Figure 9 to the "G and L" geoid of Figure 8. The "1x1°" geoid represents a geoid obtained by free-air values within the area of Figure 6 and using gravity values obtained from Gaposchkin and Lambeck spherical harmonic coefficent to degree and order 16 outside this area. The reference ellipsoid has a flattening of 1/297.0. Dotted contours are in areas of poor gravity control.

is that the actual numerical integration which is the most laborious part of the procedure is done only for the limited area of the western North Atlantic. It also has the advantage that the "1x1° difference" geoid clearly indicates the extra information not available from the spherical harmonics coefficients of degree and order 16.

In using averaged surface free-air anomalies in the inner area and those obtained from the spherical harmonic coefficients for the outer area, one must be particularly careful on two accounts. One, that the same reference ellipsoid must be used in both cases. We have used the International Ellipsoid (with flattening 1/297.0). Secondly, the areal average of the anomalies shown in Figure 6 must not be different from the areal average of "G and L" gravity. We have compared these averages and find there is a slight difference (of about 1 mgal) in the two areal averages. The systematic error in geoid height corresponding to this difference is negligible and is not considered further. Errors due to uncertainties in the exact dimensions of the reference ellipsoid are inconsequential for this study.

In order to convert the gravity or geoidal height data referred to the International Ellipsoid and refer it instead to ellipsoids of flattening 1/298.25 (best fitting) and hydrostatic (1/299.7) the curves in Figure 11 can be utilized.

Details of Stokes Integration

As discussed above, the Stokes Integration was carried out over the western North Atlantic using the 1x1° and 5x5° free-air gravity average values shown in Figure 6.

The geoidal height N at any point is given by Stokes Formula:

$$N = \frac{1}{4\pi g r} \int_{o}^{S} S(\psi)\delta g \, ds \qquad \text{where}$$

g and r are the mean values of gravity and earth radius over the geoid, ψ is the

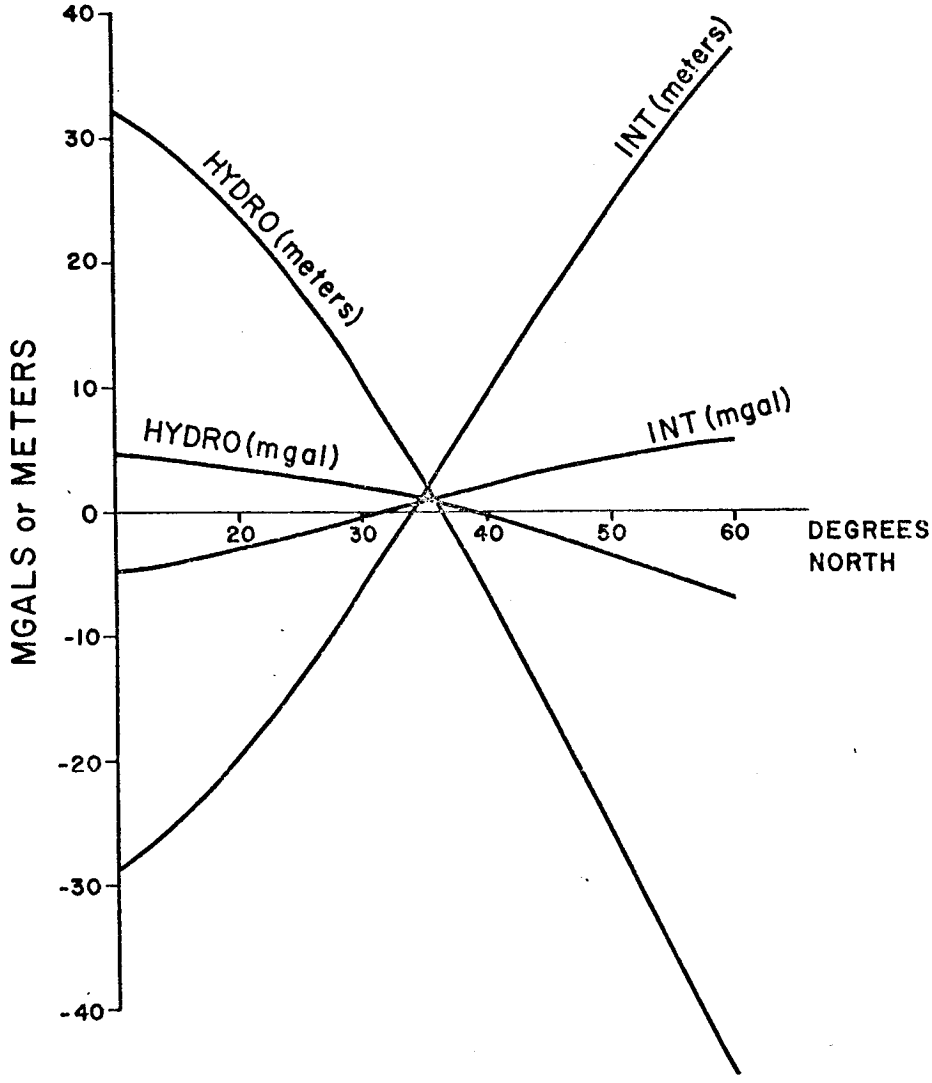

Figure 11. Values from these graphs can be added to convert from geoid or gravity values referred to the best fitting geoid (flattening 1/298.25) to geoid or gravity values referred to the International Ellipsoid (flattening 1/297.0), or the hydrostatic ellipsoid (flattening 1/298.7).

angular distance from the point of computation of an element of area ds with gravity anomaly δg, and Stokes function $S(\psi)$ is given by

$$S(\psi) = \frac{2}{\sin\psi} F(\psi)$$

where

$$F(\psi) = \cos \tfrac{1}{2}\psi + \tfrac{1}{2} \sin\psi \, [1-5 \cos\psi - 6 \sin \tfrac{1}{2}\psi - 3 \cos\psi \ln(\sin \tfrac{1}{2}\psi + \sin^2 \tfrac{1}{2}\psi)]$$

In order to reduce computing time, the value of $F(\psi)$ was tabulated in the following way (where ψ is in degrees): For $.1<\psi<1$ it was tabulated at every hundredth of a degree; for $1<\psi<5$ it was tabulated at every tenth of a degree and for $\psi>5$ tabulated at every degree. The value of $F(\psi)$ at any ψ was then obtained by interpolation between tabulated values. For $\psi<.1$ the constant value of 1.007. for $F(\psi)$ was used.

In carrying out the Stokes integration the elements of area were the 1x1° or 5x5° squares. In either case, since $S(\psi)$ changes rapidly near the origin, the effect of a square cannot be obtained for a point of computation very close to the square simply by using the value of $S(\psi)$ corresponding to ψ the distance from the point of computation to the center of the square. The percentage error in such a procedure is plotted as a function of ψ in Figure 12. The square must be subdivided into n smaller squares, the value of $S(\psi)$ being obtained for each of the smaller squares and then averaged for the entire square. In this study we have in all cases calculated geoid heights at <u>corners</u> of squares. Thus the minimum distance from a point of computation is 0.5° to the center of a 1x1° square and 2.5°

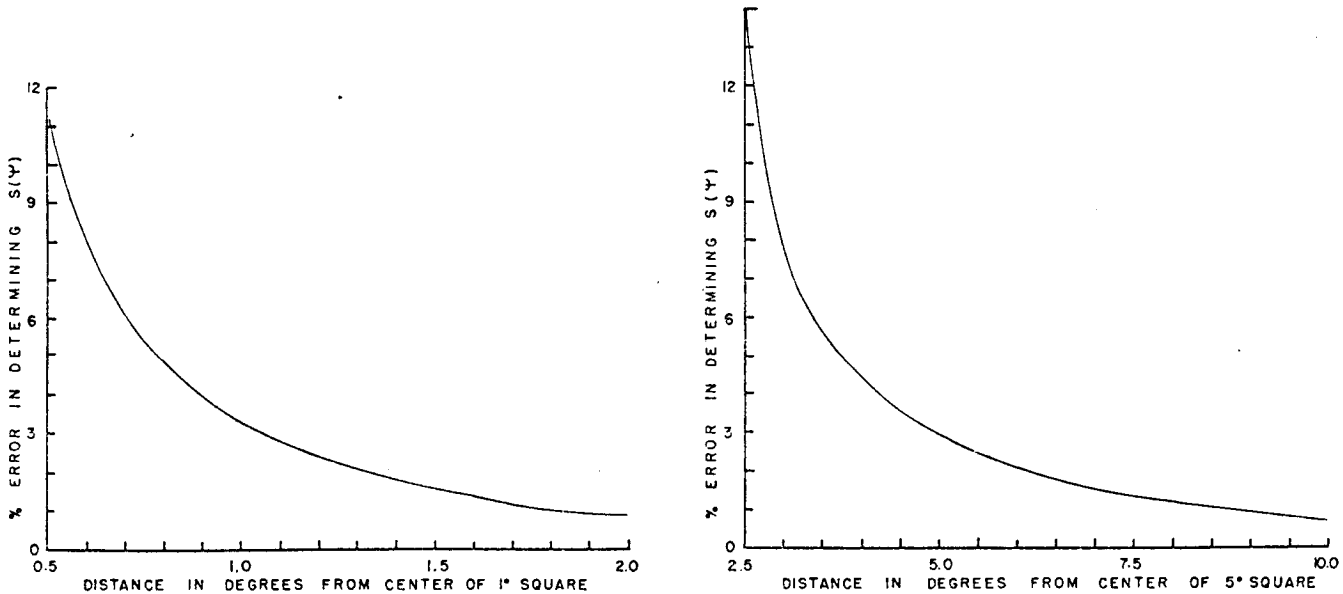

Figure 12. For squares close to the point of calculation Stokes function $S(\psi)$ changes very rapidly. Graphs show percentage error in assuming that the value of the function $S(\psi)$ where ψ is the distance from the point of computation to the center of a 1x1° or 5x5° square, represent the average value of $S(\psi)$ for that square. If the error is large the square has to be broken up into smaller squares (see Table 1) to perform Stokes integration.

to the center of a 5x5° square (even at the farthest north latitudes).

Table 1 gives the value of n versus the angular distance ψ necessary to keep the error in calculating s (ψ), below 1% for both 1x1° and 5x5° squares.

Table 1

5x5° squares		1x1° squares	
ψ>9.5°	n = 1	ψ>2.0	n = 1
9.5>ψ>5.0	n = 2	2.0>ψ>1.1	n = 2
5.0>ψ>4.0	n = 3	1.1>ψ>0.7	n = 4
4.0>ψ>3.5	n = 4	0.7>ψ>0.5	n = 5
3.5>ψ>3.0	n = 5		
3.0>ψ>2.5	n = 12		

Economy in computing time was obtained by combining twenty five 1x1° squares into a single 5x5° square when the angular distance of the point of computation from the center of the 5x5° square was greater than 15°.

10x10' Difference Geoid

In the Caribbean the gravity anomalies and the gravity gradients are so large that we suspected that even gravity anomalies of wavelength less than 200 km (the shortest wavelengths represented in the 1x1° maps) might make significant contributions to the geoid heights. In the Eastern Caribbean we used the values of gravity interpolated at the centers of a 10x10' grid to determine geoidal undulations with wavelengths as short as nearly 40 km. The 1x1° averaged gravity values were subtracted from the 10x10' grid values and were used in a Stokes integration to obtain a "10x10' difference" geoid (Fig. 13). This geoid for the Eastern Caribbean represents the extra short wavelength information present in the 10x10' gravity values. The reference surface is the "1x1°" geoid of Figure 10.

We consider this "10x10' difference" geoid computation a very preliminary one. Having determined that the geoidal undulations corresponding to 10x10' gravity differences are significant, we intend to make a more precise determination of this geoid in the future.

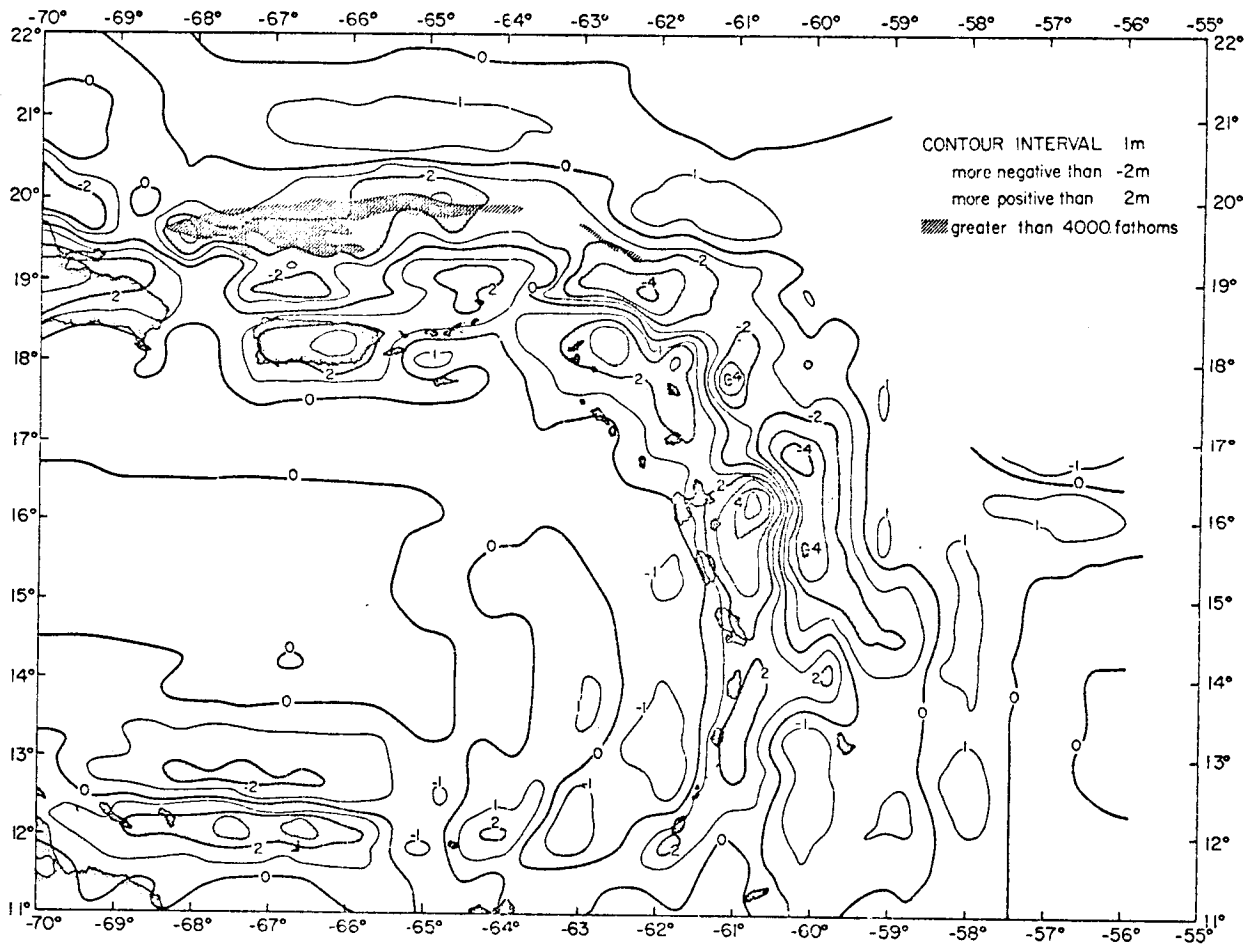

Figure 13. "10x10' difference" geoid. Free-air gravity values in the Eastern Caribbean were interpolated at the corners of a 10x10' grid. 1x1° averaged gravity values (Fig. 6) were subtracted from the 10x10' values to obtain 10x10' difference gravity values. These were used to compute the "10x10' difference" geoid. This geoid represents short wavelength geoid undulations which had been eliminated by the averaging over 1x1° squares in the computation of the geoid of Figures 9 and 10. A "10x10'" geoid can be obtained by adding the "10x10' difference" geoid to the "1x1°" geoid of Figure 10.

5. COMPARISON BETWEEN THE DIFFERENT GEOID MAPS

A basic purpose of this study was to determine whether short wavelength gravity data, in the western North Atlantic, contribute significantly to geoidal undulations. Figure 9, the "1x1° difference" geoid (which is the "1x1°" geoid referred to the "G and L" geoid) shows that these short wavelength undulations are indeed significant. The geoidal height differences exceed 10 m in the western North Atlantic and the Caribbean. A difference of 21.5 m indicated in the Gulf of Mexico may be somewhat exaggerated due to poor gravity data we have used for Mexico (this point is discussed later) but it certainly represents a large and significant departure from the geoid based on Gaposchkin and Lambeck's combination solution. The geoidal differences are further increased when the "10x10' difference" geoid is also considered. The total differences (obtained by summing the "1x1° difference" geoid and the "10x10' difference" geoid) are nearly equal to 20 m. Peak to peak variations associated with such features as the Puerto Rico Trench and the Lesser Antilles negative belt approach 25 m.

The differences between the various geoids are illustrated along a north-south profile from the South American margin across the Venezuelan Basin, Puerto Rico Island and Trench to the North Atlantic in Figure 14 and along an east-west profile from the Venezuelan Basin across the Lesser Antilles into the North Atlantic in Figure 15. In both figures most of the curves are self-explanatory. A "2-D deflection of the vertical" was obtained by computing the horizontal component of the gravitational attraction corresponding to the free-air gravity curve assuming that there were no gravity differences perpendicular to the profile. The "2-D deflection of the vertical" was integrated to get the 2-D geoid profile. The "10x10' difference" geoid (Fig. 13) was added to the "1x1°" geoid to get the "10x10'" geoid. The slope of the "10x10'" geoid gives the "10x10'" deflection curve. Attention is drawn to the large difference between the "10x10'" geoid and the "G and L" geoid in the vicinity of the trench. Significant differences also exist in the Venezuelan Basin and over the South American Margin.

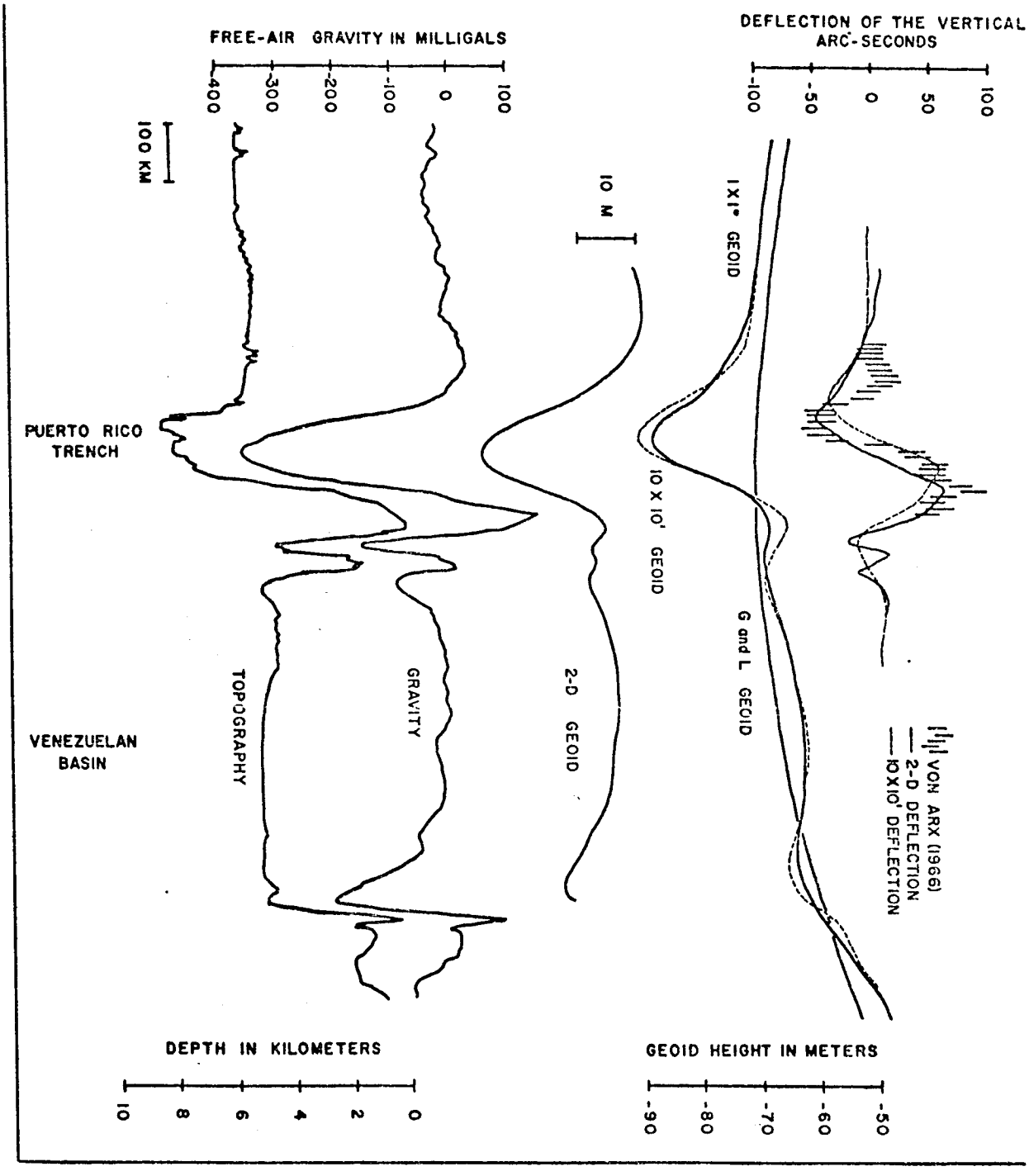

Figure 14. Profiles of gravity, geoid, and deflection of the vertical from the South American margin across the Venezuelan Sea, Puerto Rico, Puerto Rico Trench into the North Atlantic. These profiles are obtained from geoids in Figures 8, 10, and 13. The "2-D geoid" and the "2-D deflection of the vertical" profiles are obtained from the gravity profile with the assumption of two-dimensionality as explained in the text. Von Arx's deflection of the vertical profile was obtained by the astrogeodetic method.

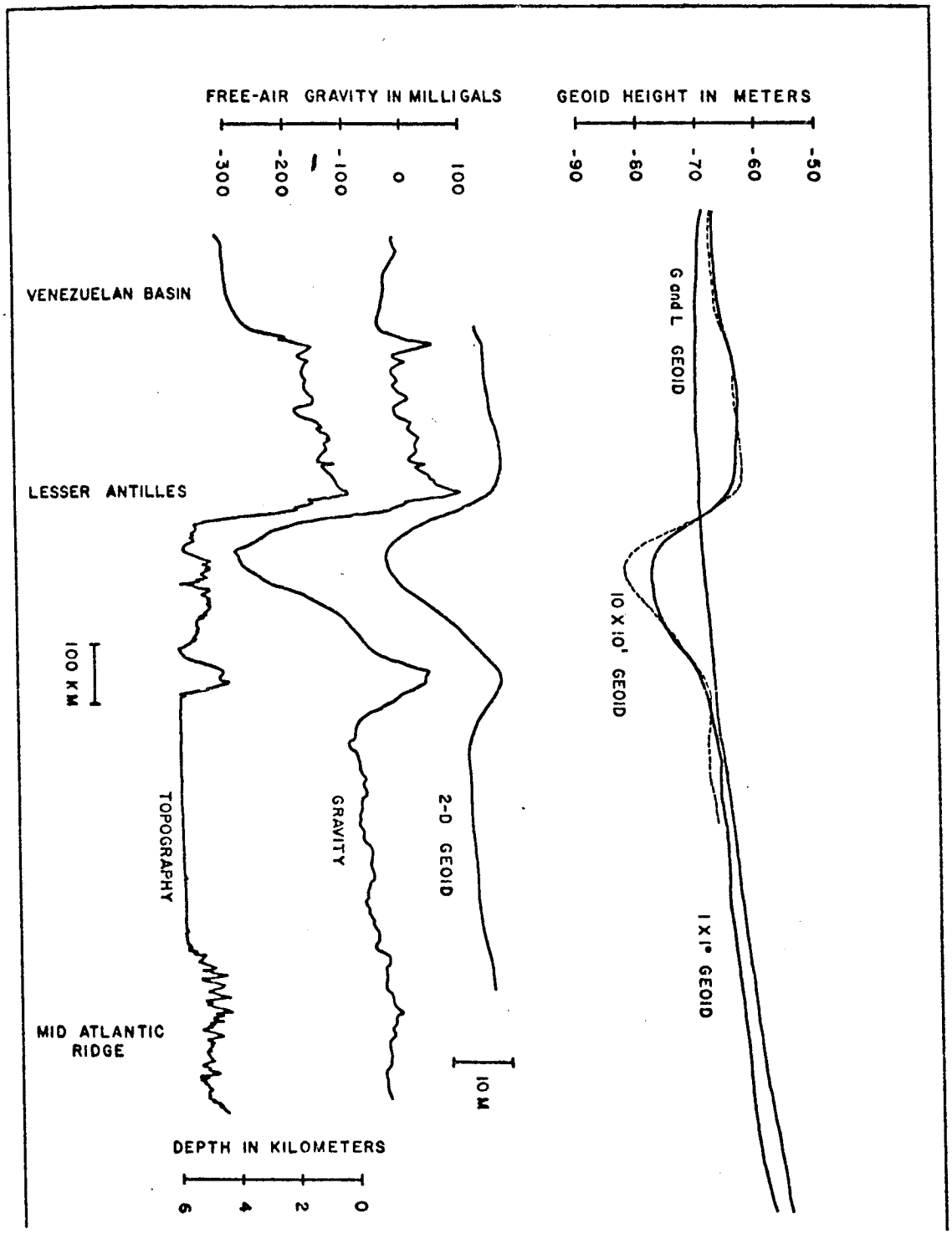

Figure 15. Gravity and geoid profiles from the Venezuelan Basin across the Lesser Antilles and the gravity belt east of the Lesser Antilles into the North Atlantic. These profiles are obtained from geoids in Figures 8, 10, and 13. The "2-D geoid" is obtained from the gravity profile with the assumption of two-dimensionality, as explained in the text.

We have also shown a profile of the deflection of the vertical obtained by Von Arx (1966) by the astrogeodetic method. We are not certain of the cause of the discrepancy between Von Arx's profile and our "10x10'" deflection profile. The difference might possibly arise from Von Arx's distance measurement made with Loran A. Our values might also change with a more precise determination of the "10x10'" geoid than we have been able to do in this preliminary study.

While the gravity anomaly associated with the Puerto Rico Trench is well known, that associated with the Lesser Antilles (Fig. 15) is almost equally important. In the negative gravity belt east of the Lesser Antilles the 10x10' geoid lies about 13 m below the G and L geoid and about 7 m above it over the island platform.

As described earlier, we used land gravity data in the United States and Canada in the construction of the geoids in the western North Atlantic. In this process we also obtained a geoid over North America and we compare it with earlier astrogeodetic measurements of the geoid (Fig. 16). Comparisons are made with a profile along 35°N obtained by Rice in 1970 (Strange et al., 1971) and with a profile along 100°W from Fisher et al. (1967). For all comparisons the geoids were referred to the best fitting ellipsoid of flattening 1/298.25. The "1x1°" geoid, which is referred to an ellipsoid of flattening 1/297.0, was transformed by using the difference curve in Figure 11. For the geoid of Rice and that of Fisher et al. (1967) we adopted the transformations given by Strange et al. (1971) and Gaposchkin and Lambeck (1971) respectively. Systematic differences (which are not of concern to us here) still exist between the "1x1°" geoid and the astrogeodetic geoids. We have added 9 m to the "1x1°" geoid profile along 35°N for comparison with Rice's profile. For the comparison along the 100°W longitude we have removed the systematic difference in plotting the curves a-c and b-c (Fig. 16).

We note that for the 100°W profile agreement of the "1x1°" geoid is excellent

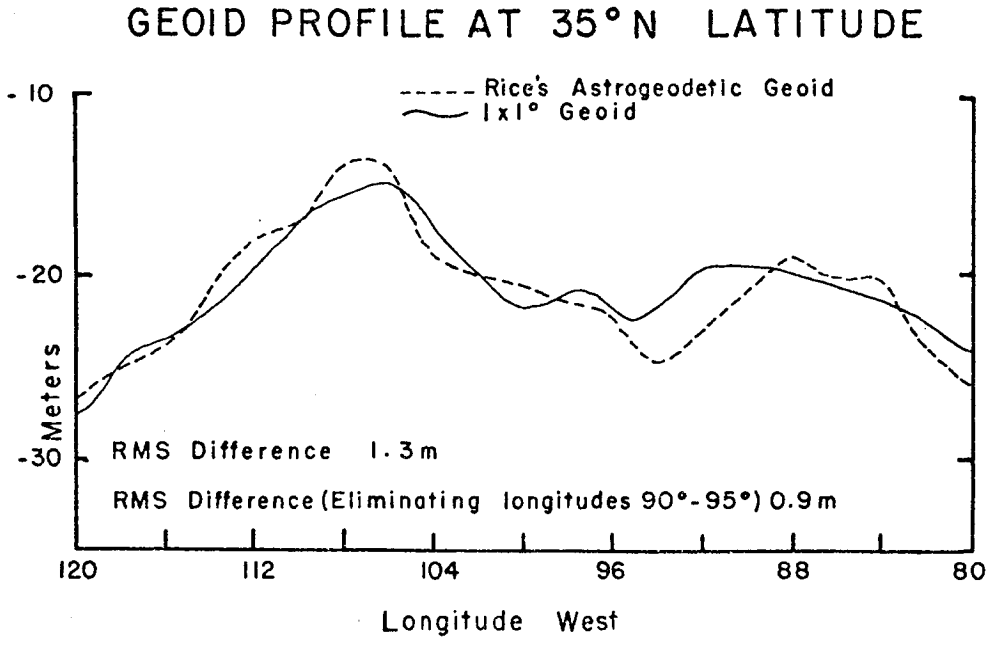

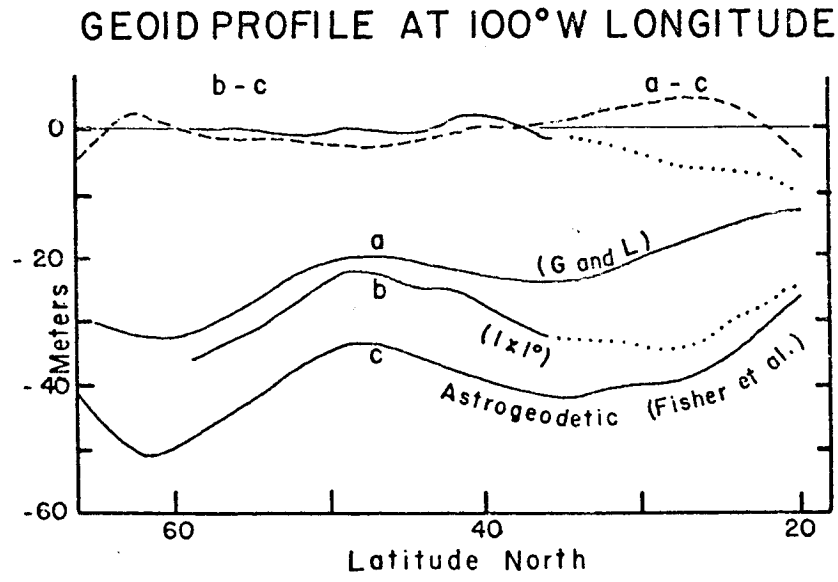

Figure 16. The "1x1°" geoid is compared to the astrogeodetic profiles of Rice along 35°N and Fisher et al. (1967) along 100°W. The "1x1°" geoid is referred to an ellipsoid of flattening 1/298.25 by using graph in Figure 11. For the astrogeodetic geoids the transformations given by Strange et al. (1971) and Gaposchkin and Lambeck (1971) were utilized. The "G and L" geoid profile at100°W referred to an ellipsoid of flattening 1/298.25 is also shown.

with the astrogeodetic profile north of 35°N. South of 35°N the "1x1°" geoid is too low. The "G and L" geoid in this region is too high. We believe that errors in the gravity values used for Mexico are responsible for giving "1x1°" geoid values that are somewhat too low.

The agreement with the profile along 35°N is also good. The RMS difference amounts to 1.3 m. If the noticeably large disagreement between 90°W and 95°W is not considered the RMS difference drops to slightly less than 0.9 m.

6. COMPARISON OF GRAVITY AND GEOID MAPS

We shall discuss the important features of the gravity map of Figure 7 and then examine the geoid map to see which gravity highs and lows can be seen in the geoid map. If, in the future, geoid maps obtained by satellite based radar altimeters are to be used for geophysical purposes, it is of great interest to examine the magnitude of the geoid undulations corresponding to important gravity features.

In comparing the gravity map (Fig. 7) with the geoid maps it would seem at first sight most logical to make the comparison with the "1x1°" geoid map of Figure 10, since both maps are referred to the same ellipsoid. However, the geoid map is much more sensitive to the low order harmonics of the gravity field which account for the large regional gradient in the geoid map. Therefore it is more useful to compare the features in the gravity map with corresponding features in the "1x1° difference" geoid map. The "1x1° difference" geoid, in effect, uses the "G and L" geoid as the reference surface. It thus principally reflects short wavelength gravity features which are also prominent in the gravity map of Figure 7.

In comparing the gravity and geoid maps note that in areas where we have used 5x5° averages the data are generally poor. The contours in such areas are dotted.

A belt of gravity high more than 500 km in width with values ranging in amplitude from 0 to 20 mgal runs along the east coast margin (including the Appalachians and the Coastal Plain) from about 30°N to 40°N. Slightly north of 40° it swings eastwards. Free-air anomalies over the edge of the shelf off Newfoundland exceed 60 mgal Gravity values further to the north in the Labrador Sea also exceed 20 mgal but these values are based on poorer data.

The "1x1° difference" geoid clearly shows a similar marginal high with values exceeding 5 m east of Newfoundland.

In the western North Atlantic Basin the geoid shows two prominent lows. One lies just seaward of the continental margin. This low runs roughly northwards from Hispaniola (between 68°W and 76°W), has a minimum slightly more negative than -10 m south of 35°N, and then turns northeast with values between 0 and 5 m. This geoid low includes the area of the Hatteras Abyssal Plain. There is a similar low in the gravity map with minima more negative than -40 mgal. Between 25°N and 30°N and along about 73°W there is a relative gravity high. This high is associated with the Blake Bahama Outer Ridge, a sedimentary ridge. If we had used a -6 m contour map for the geoid this relative high would have been delineated quite clearly. The relative high of -5.4 m is an indication of this high over the Outer Ridge.

The second prominent geoid low in the western North Atlantic is centered near 25°N 55°W and clearly correlated with low gravity values of the western North Atlantic Basin. This low lies over the eastern part of the Nares Abyssal Plain and over the abyssal hills to the east of it. In between the two lows the gravity values, as well as the geoid heights, increase, reflecting the influence of the "Outer High" seaward of the Puerto Rico Trench. This gravity and geoid high continues northwards with a geoid maximum of 1.8 m over the Bermuda platform. The other two closed geoid highs are over the Kelvin Sea Mount chain.

As the Mid-Atlantic Ridge crest is approached east of 45°W between 25°N and 35°N the gravity anomalies and the geoid heights attain positive values. The closed geoid high with a maximum of 0.6 m at 45°N 45°W is also over the Mid-Atlantic Ridge crest. A geoid low with a minimum of -7.2 m is centered near 41°N 42°W over the Newfoundland Basin.

In the Caribbean area the prominent negative belts associated with the Puerto Rico Trench and its eastern extension around the Lesser Antilles and into Barbados (12.5°N 59.5°W) are clearly reflected in the geoid map. The negative belt along the northern coast of South America is also associated with a low in the geoid. Gravity as well as geoid highs lie over the islands of the Hispaniola and Jamaica and southeast Cuba and continue southwest along the Nicaraguan Rise into Middle America.

The "10x10' difference" geoid map (Fig. 13) helps to resolve the gravity features even further. A high is apparent over the island of Puerto Rico and lows over the Anegada Trough (east of Puerto Rico) and Dominican Trench (south of Puerto Rico) are resolved. A geoid high lying roughly between 12° and 16°N and 63° and 64°W resolves the Aves Swell. Along the South American margin both the gravity highs over the Dutch Antilles and Las Rocques etc. as well as the marginal lows are seen in the geoid maps.

A value of -21.5 m in the Gulf of Mexico in the "1x1° difference" geoid indicates the largest departure from the "G and L" geoid. The gravity contours in Figure 7 indicate large negative values. The contours west of 95°W in the Gulf of Mexico are based on reliable sea values even though they are dotted (because they lie in a square where 5x5° average rather than 1x1° average values were used). However, the values in Mexico are few and unreliable. We also note that the astrogeodetic geoid along 100°W in Mexico (between 20°N and 35°N) lies below the "G and L" geoid, (when adjusted for systematic differences) but above the 1x1° geoid. We know from the newer data of Woollard et al. (1969) which we have

not used in this study that the gravity anomalies in the 5x5° square centered at 22.5°N 100.5°W and in the 5x5° square to the north are higher than the values used in these calculations. The use of corrected values will raise the geoid over Mexico and to a smaller extent in the Gulf of Mexico. Qualitatively we would expect the -10 m and -15 m contours to shift eastwards and the lowest value in the Gulf of Mexico to become slightly less negative.

In summary, we see that the "1x1° difference" and the "10x10' difference" geoids give large differences in the short wavelengths from the "G and L" geoid based on the 1969 SAO Standard Earth. These difference geoids correlate well with gravity features in the map in Figure 7. The association of geoid features with physiographic features in the North Atlantic clearly points out the usefulness of accurate geoid maps in learning the details of the gravity field in the short wavelength range used for crustal studies.

ACKNOWLEDGMENTS

Drs. J. L. Worzel and D. E. Hayes read the manuscript critically. This work was supported by the Office of Naval Research through contracts N00014-67-A-0108-0004 and Nonr 266(79); and by grants from the National Science Foundation including grants GA17761 and GA27281.

REFERENCES

Caputo, M., R. Masada, M. Helfer, and C. L. Hager (1964), Gravity measurements in the Atlantic, Pacific, and Indian Oceans, May 1962 - August 1963 (R.V. Argo). Interim Rept. Univ. Calif. Inst. Geophys. Planetary Phys. 7, 20 pp. Unpublished manuscript.

Dehlinger, P., and B. R. Jones (1965), Free-air gravity anomaly map of the Gulf of Mexico and its tectonic implications, 1963 edition, Geophysics 30, 102-110.

Emery, K. O., E. Uchupi, J. D. Phillips, C. O. Bowin, E. T. Bunce, and S. T. Knott (1970), Continental rise off eastern North America, Am. Assoc. Petrol. Geol. Bull. 54, 44-108.

Fischer, I., M. Slutsky, R. Shirley, and P. Wyatt (1967), Geoid charts of North and Central America, Army Map Service Tech. Rept. 62.

Gaposchkin, E. M., and K. Lambeck (1971), Earth's gravity field to the sixteenth degree and station co-ordinates from satellite and terrestrial data, J. Geophys. Res. 76, 4855-4883.

Gaposchkin, E. M., and K. Lambeck (1970), 1969 Smithsonian Standard Earth (II), Smithsonian Astrophys. Obs. Special Rept. 315, 93 pp.

Goodacre, A. K. (1964), A shipborne gravimeter testing range near Halifax, Nova Scotia, J. Geophys. Res. 69, 5373-5381.

Keen, M. J., B. D. Loncarevic, and G. N. Ewing (1971), Continental margin of Eastern Canada: Georges Bank to Kane Basin, in The Sea, vol. 4, part 2, edited by A. E. Maxwell, pp. 251-291 (John Wiley and Sons, Inc., New York, N. Y.).

LaCoste, L. J. B., and J. C. Harrison (1961), Some theoretical considerations in the measurement of gravity at sea, Geophys. J., 5, 89-103.

Orlin, H., B. G. Bassinger, and C. H. Gray (1965), Cape Charles - Wallops Island, Virginia, off-shore gravity range, J. Geophys. Res. 70, 6265-6267.

Rabinowitz, P. D., and M. Talwani (1969), Gravity anomalies in the western North Atlantic Ocean (abstract), Geol. Soc. Am. Abstr. Progr. Pt. 7, p. 189.

Shurbet, G. L., and J. L. Worzel (1957), Gravity measurements in Oriente Province, Cuba, Geol. Soc. Am. Bull. 68, 119-124.

Strange, W. E., S. F. Vincent, R. H. Berry, and J. G. Marsh (1971), A detailed gravimetric geoid for the United States, Goddard Space Flight Center Rept. X-552-71-219.

Strange, W. E., and G. P. Woollard (1964), The use of geologic and geophysical parameters in the evaluation, interpretation, and prediction of gravity, Hawaii Inst. of Geophys. Rept. HIG-64-17.

Talwani, M. (1959), Gravity anomalies in the Bahamas and their interpretation: Ph.D. thesis, Columbia University, New York, p. 1-89.

Talwani, M., W. P. Early, and D. E. Hayes (1966), Continuous analog computation and recording of cross-coupling and off-leveling errors, J. Geophys. Res. 71, 2079-2090.

Talwani, M., and X. LePichon (1969), Gravity field over the Atlantic Ocean, The Earth's Crust and Upper Mantle, ed. P. J. Hart, pp. 341-351, AGU, Washington, C. C.

Talwani, M., and H. Poppe (1968), Gravity field of the Caribbean Sea, presented at Fifth Caribbean Geological Conference.

Vening, Meinesz, F. A. (1948), Gravity Expeditions at Sea 1923-1938, IV, publ. Netherlands Geodetic Commission, Delft.

Von Arx, W. S. (1966), Level-surface profiles across the Puerto Rico Trench, Science 154, 1651-1654.

Walcott, R. I. (1970), Isostatic response to loading of the crust in Canada, Can. J. Earth Sci. 7, 716-727.

Woollard, G. P., L. Machesky, and J. M. Caldera (1969), A regional gravity survey of northern Mexico and the relation of Bouguer anomalies to regional geology and elevation in Mexico, Hawaii Inst. of Geophys. Rept. HIG-69-13.

Worzel, J. L. (1965), Pendulum Gravity Measurements at Sea, (John Wiley and Sons, Inc., New York, N. Y.).

Comments on Ocean Circulation with Regard to Satellite Altimetry

Wilton Sturges

University of Rhode Island

Abstract

Basic features of sea-surface topography are reviewed, to show those oceanographic results which may be of value to a geodetic satellite program: (1) the shape and magnitude of the large-scale features of the mean sea surface, relative to a level surface; (2) the position and magnitude of the slopes across the western boundary currents, from a variety of data; (3) an estimate of the position of the Geoid, tied into the U.S. leveling network (4) a documented change of 60 to 70 cm in mean sea level, with respect to the Geoid, between the U.S. east and west coasts. Presents maps of item (1) are accurate to about 30 cm, but this accuracy could be improved to about 10 cm with existing data. Some oceanographic problems which seem compatible with the capabilities and advantages of satellite altimetry are; (1) to locate the positions of the major western boundary currents, particularly the meandering portions, to obtain data for a variety of questions; (2) to determine the status of currents whose existence or position depends on climatological factors either not well understood or not easily measured; (3) to resolve the present conflict between oceanographic and land levelling with regard to the north-south slope of sea level along the coasts; (4) to track, insofar as possible, the mid-ocean eddies which are roughly 100 km in horizontal extent.

This paper is about several aspects of the large-scale ocean circulation, particularly as they relate to data that

can be obtained from an altimeter in an orbiting satellite. It seems appropriate to review several ways in which oceanographers can contribute information of value to the geodesists, and then to discuss some ways in which the satellite altimeter can contribute information of interest to the oceanographers. There have been other recent reviews of this topic in the so-called "Williamstown Report" by von Arx (NASA, 1969), and by Greenwood, Nathan, Neumann, Pierson, Jackson, and Pease (1969). I should emphasize that the topics discussed here are not selected on the basis of the precision of present altimeters; rather, I will try to emphasize oceanographic problems that seem to lend themselves well to a satellite program.

A useful result for the present purpose is the geopotential anomaly of the sea surface, relative to a deep pressure surface, computed from the observed density distribution. Maps of geopotential anomaly represent, to a good approximation, the shape of the physical sea surface, relative to a level surface. A map of the world ocean, Figure 1, has been given by Stommel (1964, chart 1; or 1965, fig. 96c). The principal features are the high regions associated with the tropical anticyclonic circulations, and the low areas at high latitudes. From the highest point, near Japan, to the Antarctic, the total relief is 2 m. It also is evident that the Pacific Ocean is somewhat higher than the Atlantic Ocean.

Montgomery (1969) has discussed ways in which the map could be improved, through use of a deeper reference surface and more modern data. The details of this map could be changed, but the basic features are not likely to be in error by more than about 30 cm. This error estimate will be discussed below.

The primary reason oceanographers have developed maps such as this one is to learn something about the average surface currents. For the simplest, steady flow, called geostrophic motion, the horizontal momentum balance is between

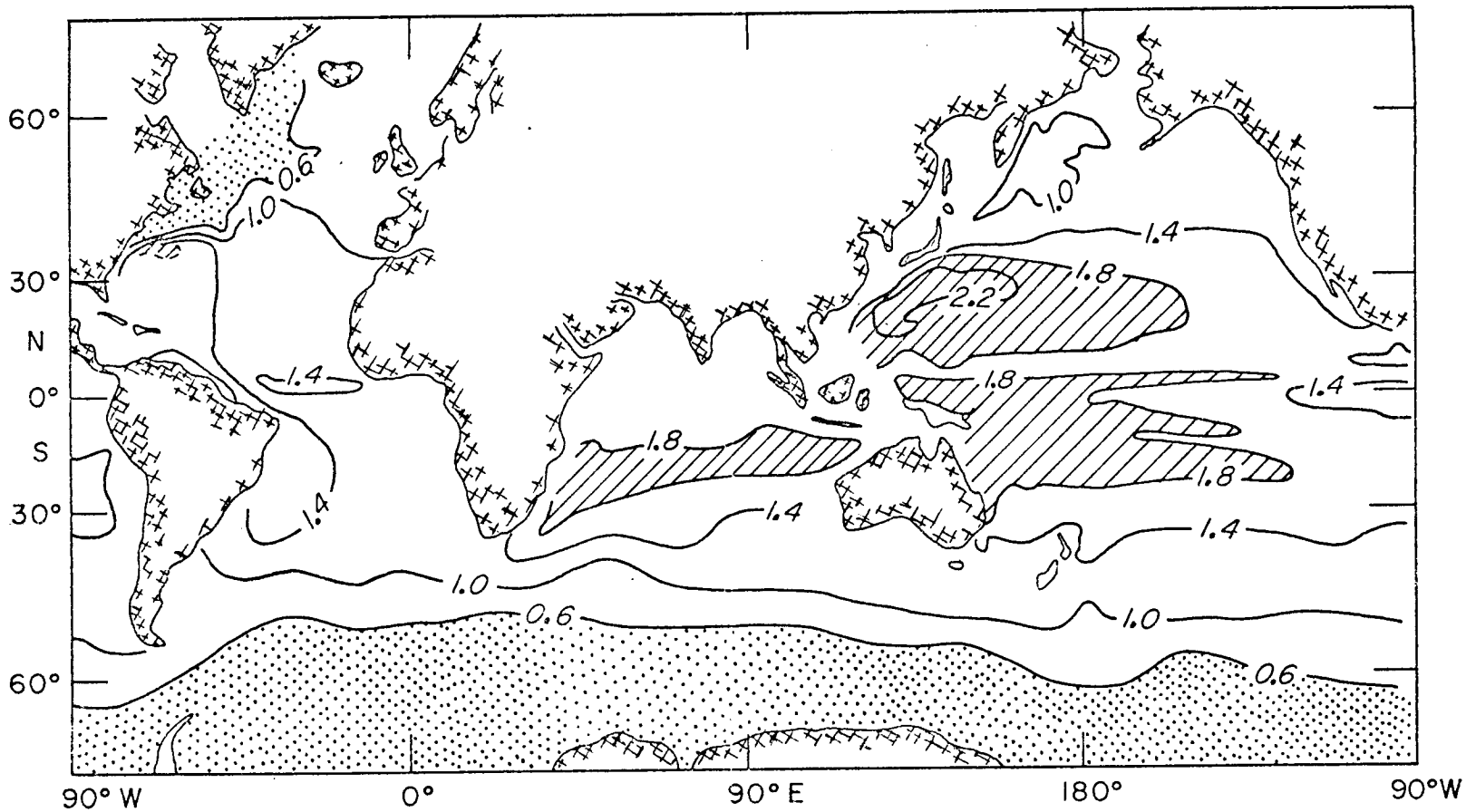

Figure 1. Dynamic topography of the sea surface relative to the 1000 decibar surface. The contours show geopotential anomaly in "dynamic meters", or $10^5 cm^2 sec^{-2}$. If the 1000 decibar surface is within 10 cm of a level surface, the contours represent approximately the elevation of the sea surface in meters, relative to a level surface. From Stommel, 1964.

the downstream velocity, v, and the horizontal pressure gradient caused by the cross-stream slope, i, of the sea surface:

$$(2\Omega \sin \varphi\ )\ v = ig \qquad (1)$$

where Ω is the earth's rate of rotation, φ is latitude, and g is gravity. The term in parenthesis is the Coriolis parameter, and has a magnitude 10^{-4} sec^{-1} at 43°. In a strong steady current, it is believed that the geostrophic relation, equation (1), is in error by no more than 10%. In the major currents it is observed that the surface currents, as determined from ship drift, are in essential agreement with the currents inferred from maps of geopotential.

There are some areas, however, where it is obvious that the observed surface current is not parallel to the isobars shown in Figure 1; the outstanding example is the 1.0 contour in the Atlantic Ocean which goes straight into the coast. Recent work by Anati (1971), based on the IGY data in the Atlantic, gives the same result as shown on the old map. The reason for this apparent conflict is that in this part of the ocean the currents are weak and the slope of the sea surface is small. As a result, the effect of the wind stress on the sea surface (not included in the geostrophic approximation, eqn. 1) is large enough to contribute an effect that can be seen on these maps. Anati has shown, for this region, that the differences between the observed surface currents and the direction of the isobars on this map can be quite well reconciled by taking the effects of wind stress into consideration. Reid (1961) has also shown a similar correspondence between the "geostrophic failures" in the Pacific Ocean and the mean wind stress.

In other words, the comparison with observed currents shows that the maps are correct in regard to the physical shape of the sea surface. Adjustments for the effects of wind stress are required only for the purpose of inferring currents through the geostrophic relation. We conclude that, qualitatively, the general features shown on these maps are correct.

For an estimate of the accuracy of these results, consider the topography near a western boundary current. Sturges (1968) has calculated the sea-surface topography between Bermuda and the east coast of the United States, using ship-drift observations to describe the velocity field, as shown in Figure 2. The results are not for an instantaneous current, but represent a climatological mean. This topography is important because it represents a result similar to the previous figure, and the two are independent. If we examine the annual mean of the absolute difference in sea level between the east coast of the United States and the offshore edge of the Gulf Stream by the two methods, the change in level is 100 cm; the two independent estimates agree to within 10 cm. The calculated annual mean effect of wind on the sea-surface topography between Bermuda and the U.S. coast is 4 cm, which can only be considered an order-of-magnitude estimate.

The numerical values of the contours in Figure 2 are based on an arbitrary mean value of 200 cm at Bermuda. These contours can be reconciled with those of Fig. 1, which is based on geopotential anomaly relative to 1000 db. The annual mean geopotential anomaly of the sea surface at Bermuda, relative to 1000 db, is 157 cm. Therefore, by subtracting 43 cm from the contours of Figure 2, they become equivalent with those in Fig. 1.

The primary uncertainty in interpreting the topography shown in Figure 1 as the physical sea surface, to high accuracy, arises from the question of whether the 1000 decibar surface is a level surface. Certainly at 1000 meters depth the currents are much weaker than at the sea surface, so the 1000 db surface should be much more nearly level than the sea surface. The 2000 db surface will be a better reference level, as has been discussed by Montgomery (1969). We know something about the velocity distribution at 1000 to 2000 meters. Away from strong boundary currents, there are amplitudes of 10 to 15 cm/sec as transients, but the

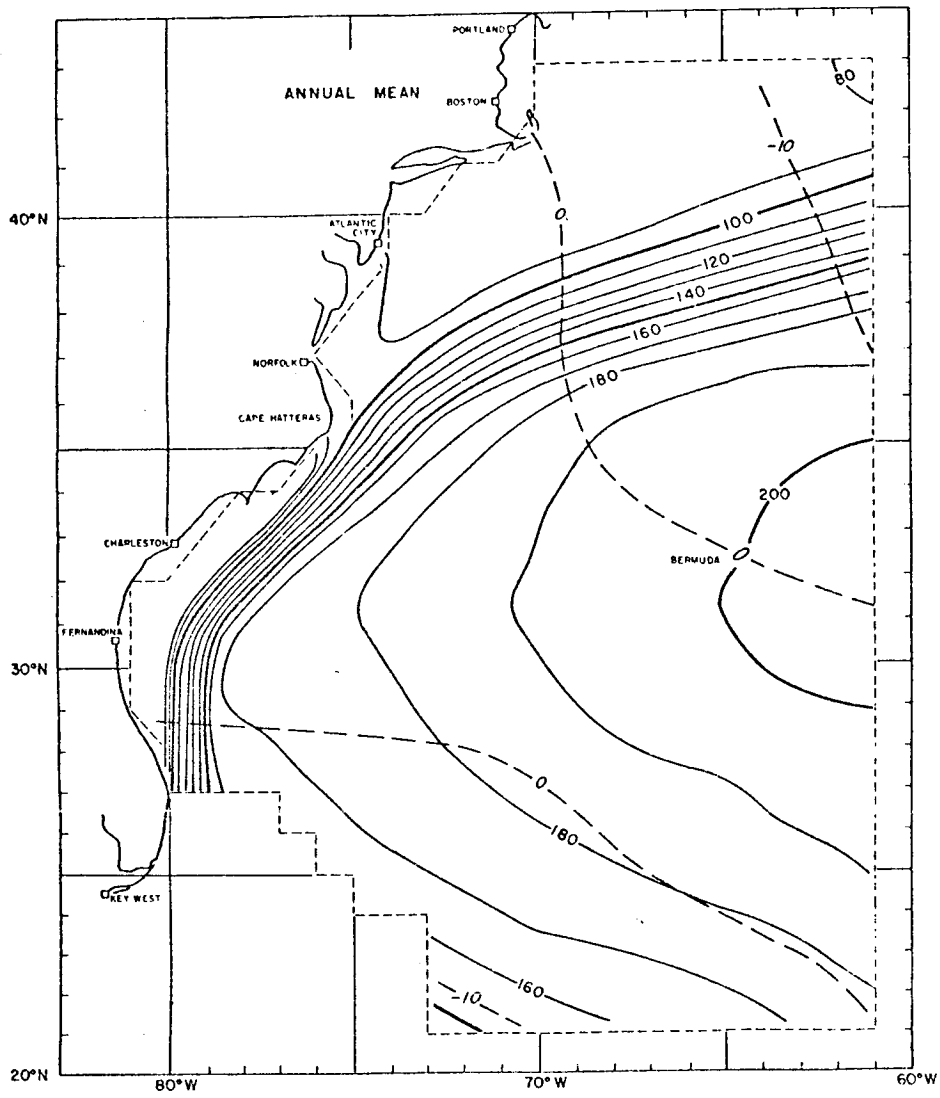

Figure 2. Sea-surface topography from ship drift: annual mean. The continuous contours show topography of the sea surface in cm based on heights calculated from ship drift; the numerical values are relative to an annual mean of 200 cm at Bermuda. The dashed contours are an estimate of the part of the computed ship-drift topography caused by the wind alone. The contour interval is 10 cm; the scale is $1:20 \times 10^6$ at 30° on Mercator projection.

average speeds are at least an order of magnitude smaller. Within the Gulf Stream, however, the speeds are consistently large enough to be measured. Observations with neutrally buoyant floats (Warren and Volkmann, 1968) or by moored current meters or transport floats (Richardson and Knauss, 1971) show clearly that an average speed of 10 cm/sec at 2000 meters in the Gulf Stream is a reasonable upper limit. Such speeds lead to a slope of the 2000 db surface of only 10 cm across the stream, with the inshore edge lower than offshore. The change in level of the 1000 db surface across the Gulf Stream is about 20 cm. That is, if the results shown in Figure 1 were to be interpreted as the physical sea surface, they could be improved slightly by compensating for the slope of the reference surface in the major boundary currents.

Anati (1971) has mapped the 1000 db surface relative to the 2000 db surface, and shows that over most of the Atlantic Ocean the total relief is less than 10 cm. We may conclude that errors of the order of 10-20 cm are to be expected in Figure 1, from a slope of the reference surface. Seasonal effects contribute about 10 cm (see,for example Donn, Pattullo, and Shaw 1964) so that an uncertainty of 30 cm would be a reasonable estimate of accuracy. If known slopes of the reference surface (e.g. beneath the Gulf Stream) are compensated, and seasonal effects are removed, good coverage with modern data could reduce the absolute error of a map, based on 2000 db, to approximately 10 cm.

Montgomery (1969) has shown that the 1.3-m surface in Fig. 1 lies near the Geoid, and is the surface which coincides with mean sea level along the Pacific coast of the United States. More work and more recent data could probably improve the details of this result, but it seems unlikely that this average value could be in error by more than 10 to 20 cm.

The arguments above concerning the shape of the sea surface refer to a surface which is assumed to be a constant

pressure surface, as this is appropriate for velocity calculations. For these results to be compared with direct measurements of the physical sea surface, as from a tide gauge, altimeter, etc. it is necessary to subtract the local variation of atmospheric pressure. It should be recognized that atmospheric pressure over the ocean must be known at least as well as the resolution demanded of the sea-surface topography. The average effect of atmospheric pressure has a range of about 30 cm; daily values are considerably larger.

Some Oceanographic Problems

Before the use of the Swallow float (or neutrally-buoyant float), or the wide-spread use of moored, recording current meters, one of the classical problems in oceanography was the "level of no motion", i.e., the question of the slope of a reference pressure surface for performing geostrophic calculations. From the density field, velocities can be calculated only relative to the velocity at some reference pressure surface, whose slope is unknown. This difficulty leads to relatively small errors in velocity at the sea surface in the Gulf Stream, for example, but to large errors in the total mass (or heat, etc.) transport.

It has been suggested that satellite altimetry could determine the slope of the sea surface well enough to be of some value in connection with the level-of-no-motion problem in the major boundary currents. The slope of the 2000 db surface beneath the Gulf Stream, however, as discussed above, is only about 10 cm across the entire stream. To be useful, therefore, the satellite data would have to provide information referred to a level surface at an accuracy considerably better than 10 cm. Furthermore, the use of moored current meters in this application is preferable to a knowledge of sea-surface slope, for two reasons. We need to know a time history of the currents, detailed enough to resolve tidal-period motions, and long enough to average over the time scale of the density measurements. It would also be preferable to have information about the reference

surface near the middle of the water column, rather than at the sea surface, where the effects of wind stress may be important. It seems likely that the capabilities of the satellite altimeter program can be used much better in ways other than solving the level-of-no-motion problem.

Position of boundary currents and meanders. For many years it has been known that the Gulf Stream follows a complex, twisted path. Figure 3, from Corton (1970) shows the positions of the inshore edge of the Gulf Stream as determined by an infra-red thermometer flown in an airplane. The inshore edge is the region of strong horizontal temperature gradient which shows up so well by this technique. The instantaneous Gulf Stream is approximately 100 km wide. The meanders generally seem to grow larger, as shown by Hansen (1969). At approximately 60° W, the meanders may be 500 kilometers in horizontal extent, and perpendicular to the stream.

A realizable goal for the satellite program would seem to be finding the strong boundary currents. The satellite technique offers promise of locating, on an ocean-wide basis, the major western boundary currents of the entire world ocean for the first time. Pointing out their locations, world-wide, would be a worthy result. How far from the continental masses do the currents retain their identity? What is the persistence of the meanders? How often do meanders grow large enough to spawn eddies that detatch from the stream and drift away? Are the answers to these questions the same in the Gulf Stream, Kuroshio, Brazil Current, and others? Does bottom topography affect the meanders? These are questions which could be answered at present with infra-red thermometers from airplanes, but with satellites it would become feasible on a large geographic scale. The infra-red techniques are strongly limited by cloud cover, so the altimeter would be an improvement. A logical question seems to be that if the infra-red techniques could find a meander, could the satellite altimeter continue to track it? There are other currents that meander, such as the path of the main flow in the Gulf of Mexico, which is

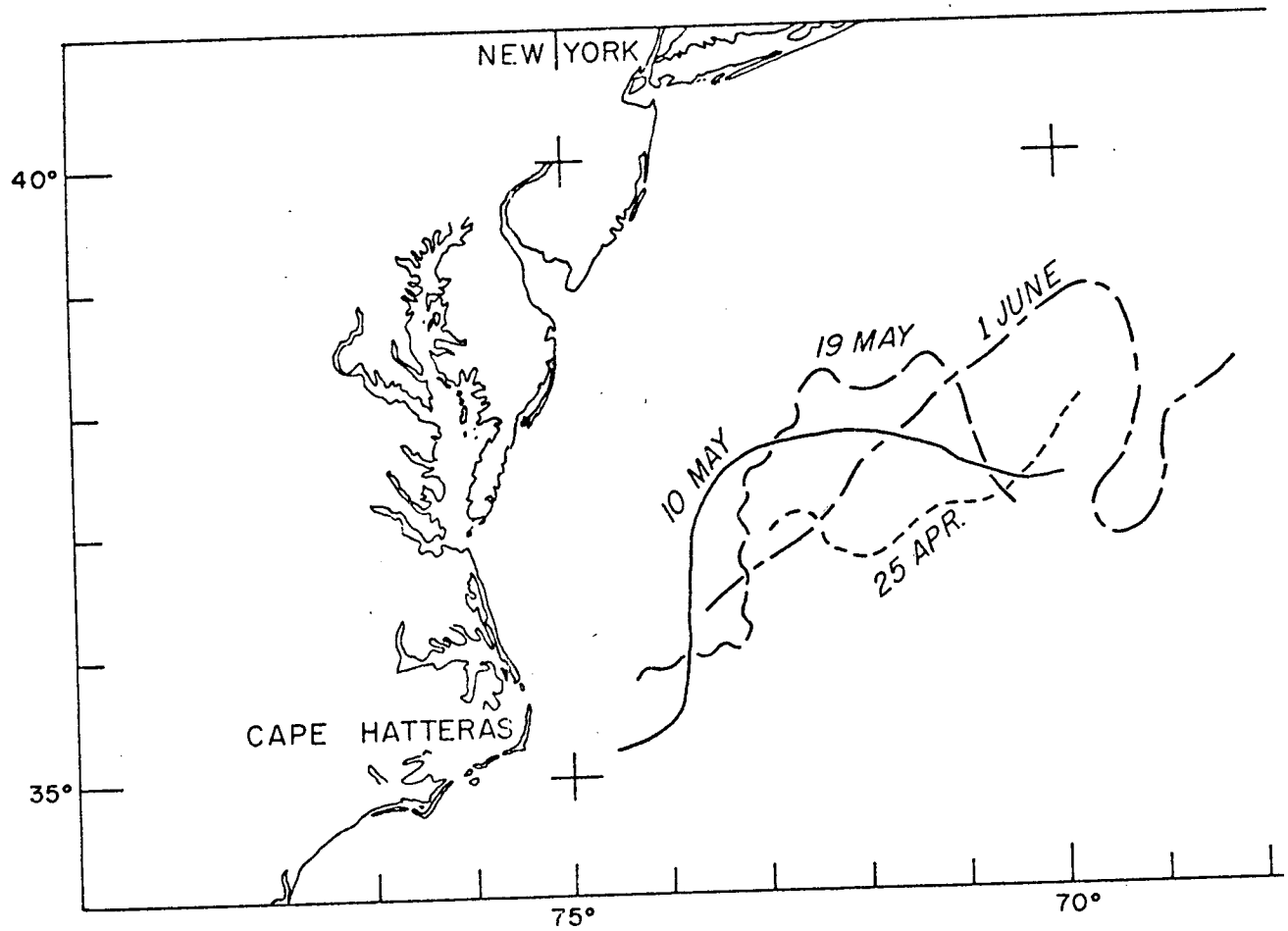

Figure 3. Position of the inshore edge of the Gulf Stream as determined by aerial infra-red observations, April-May 1970 (after E.L. Corton, Gulf Stream Summary, 1970).

quite irregular (it sometimes leads to a "Loop Current"). Presumably satellites could determine the onset of the Somali Current, and others.

It has been pointed out by Greenwood et al. (1969) that a satellite leaving the east coast of the United States passes over strong topography of the Geoid. A Gulf-Stream "signal", one meter in elevation and 100 km wide, will be superposed on the much larger features of the Geoid. Where the Gulf Stream is close to the coast and more nearly constant in position, the airborne infra-red surveys can point out its position. Farther from the coast, however, the large meanders will be not steady features. Over the course of many satellite passes these time-dependent features will be separable from the "background" shape of the Geoid. Although the meanders can remain in a fixed position for short times, they usually change position substantially during a time scale of perhaps two weeks. It is apparent that the satellite must reach latitudes as far north as 40° to 42° to be useful for this purpose.

Eastern boundary currents, such as the California Current, have a much smaller signal than western boundary currents, so that it may not be feasible to track them by the altimeter; it would be interesting to try. The change in level is only about 1/3 that of a western boundary current, and the width is 5 to 10 times greater. Wooster and Reid (1963) give averages of 34 cm and 1000 km for the change in elevation, and width.

Slope of sea level along coasts. The next area in which the satellite altimetry results could make contributions to oceanography concerns the problem of the slope of sea level along the coasts. Since the 1920's it has been known from precise leveling on land that mean sea level appears to rise from south to north. Braaten and McCombs (1963) have shown the results of a special leveling adjustment. They found that the coastal rise of sea level, as indicated by the leveling, is approximately 60 cm on both the east coast and the west coast of the United States. They also show that mean sea level on the Pacific coast of the U.S.

stands about 60 cm higher than along the Atlantic coast, as shown in Figure 4.

Montgomery (1969) has concluded that the oceanographic results are in good agreement with the leveling results as to the difference in mean sea level between the Atlantic coast and the Pacific coast of the United States. The oceanographic leveling here suffers from the problem of a reference-level assumption, and I have recently estimated (Sturges, 1971) that the uncertainty introduced by the choice of a reference surface is only a few centimeters.

A question that remains unresolved, however, is the apparent slope from south to north as indicated by the leveling results. A slope of 60 cm is a very large signal in terms of ocean currents, so the apparent slope along the coasts is important, in terms of ocean circulation.

The oceanographic result refutes this coastal slope (Sturges, 1967). That is, oceanographically, we expect sea level at San Diego to be some 9 cm higher than at Neah Bay. The leveling results are from a combination of a very large number of short sights. It is possible, therefore, that the presence of an extremely small undetected systematic leveling error in the north-south direction could contribute to a resulting systematic error in the leveling results. The only definite statement we can make is that the two results do not agree. It might be possible to resolve this discrepancy by searching for the systematic error in the leveling results. But the satellite altimetry program offers the promise of being able to determine whether the coastal slopes exist, by an independent method.

This problem is a thorny one in terms of separating a slope of the Geoid from a slope of the sea surface. This aspect of the problem could be side-stepped by using the basic oceanographic results in deep water (as discussed above, concerning Stommel's map). The satellite results could be used only to connect the coastal points to the

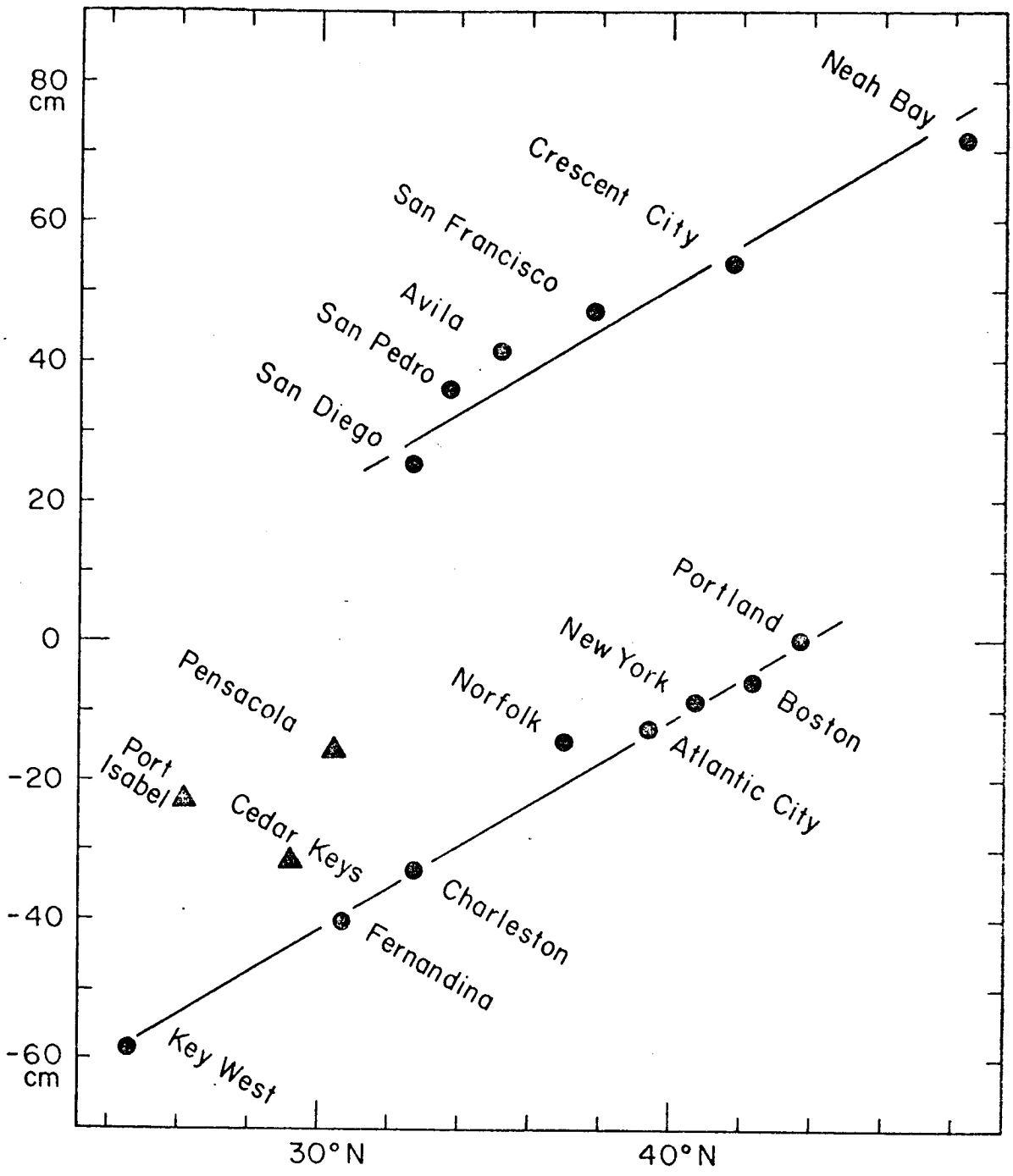

Figure 4. Relative heights of mean sea level vs. latitude based on the Special Leveling Adjustment of 1963 (after Braaten and McCombs 1963). Atlantic and Pacific coast tidal stations are shown by dots; Gulf Coast stations by triangles. The lines have slope 0.28×10^{-6}. Vertical exaggeration is approximately 2×10^{6}.

deep-water results. The uncertainty of the absolute shape of the Geoid remains, but it enters the problem in a different way. The satellite must reach latitudes as far north as 44° in order to provide useful information on this problem.

Tracking eddies. The third way in which the satellite program could contribute to our knowledge of ocean circulation is through the tracking of eddies in mid-ocean. Meteorologists know that to understand the dynamics of atmospheric circulation they have to track the numerous high - and low-pressure cells as they move across the continent. Oceanographers, however, at present must rely almost entirely on steady-state models of the circulation, in which the eddy processes are represented in only a parametric way by the so-called Eddy coefficients. Unfortunately we do not really know how important the eddies are, in the dynamics of ocean circulation. We do know that we need to find out; and in fact this is the goal of a large cooperative venture called "MODE", for Mid-Ocean Dynamics Experiment. If the satellite program could find and track a large number of eddies over a period of several years (perhaps indefinitely, if we are to talk about ocean weather) it would provide a very valuable contribution.

It will probably be only the larger eddies that can be found by the altimeter. Eddies that have been spawned from the Gulf Stream will have a relatively large signal -- initially as large as 1 meter. A typical eddy near the stream may have speeds of 3 knots and be 100 kilometers across, to give a topographic relief of 35 centimeters, at 40 degrees latitude. At lower latitudes, the geostrophic balance is achieved with smaller slopes. The more common eddy, far removed from a major boundary current, and produced by a variety of mechanisms, may have speeds closer to 5 cm/sec and a width of 200 km, to produce a topographic relief of only 5 cm. I suspect that this signal will be beyond the reach of the altimetry program.... but we do not know to what extent the topographic signals coincide with temperature signals, or how large the signals really are. At middle

latitudes even a small eddy, once found by any technique, might be tracked by a system with marginal resolution. It is necessary to point out, however, that a knowledge of atmospheric pressure would be crucial in this program. A 10 mb weather disturbance will have a topography identical to a 10 cm isobaric disturbance caused by an oceanographic eddy.

One further point deserves mention. Present discussions suggest that the Geos - C satellites will be launched into orbits having inclinations of perhaps 50° to 60°. This inclination, while quite appropriate, will place the satellites systematically over the higher portions of the ocean, as can be seen on Stommel's map (Fig. 1). If an accurate determination of the absolute position of the Geoid is desired, this difference should be taken into consideration.

ACKNOWLEDGMENTS

The preparation of this article was supported in part by the Office of Naval Research.

References

Anati, David A. (1971) Some aspects of the relative geostrophic flow in the North Atlantic Gyre. Deep-Sea Res. in press.

Braaten, N.F. and C.E. McCombs (1963) Mean sea level variations as indicated by a 1963 adjustment of first-order leveling in the United States. Unpubl. Tech. Rep., U.S. Coast and Geodetic Survey.

Corton, E.L. (1970) The Gulf Stream, Monthly Summary 5(5) U.S. Nav. Ocean. Office, Washington.

Donn, William L., June G. Pattullo, and David M. Shaw (1964) Sea-level fluctuations and long waves, chapter 10, in Research in Geophysics, vol. 2, edited by Hugh Odishaw, Massachusetts Institute of Technology Press, Cambridge, Mass.

Greenwood, J.A. et al. (1969) Oceanographic applications of radar altimetry from a spacecraft. Remote Sensing of Environment 1, 71-80 Elsevier, New York.

Hansen, Donald V. (1970) Gulf Stream meanders between Cape Hatteras and the Grand Banks. Deep-Sea Res. 17, 495-511.

Montgomery, R.B. (1969) Comments on oceanic leveling. Deep-Sea Res. 16, suppl, 147-152.

National Aeronautics and Space Administration (1969) The terrestrial environment, solid earth and ocean physics, application of space and astronomic techniques. Report of a study at Williamstown, Mass.

Reid, J.L., Jr. (1961) On the geostrophic flow at the surface of the Pacific Ocean with respect to the 1,000-decibar surface. Tellus, 13, 489-502.

Richardson, P.L. and J.A. Knauss (1971) Gulf Stream and Western Boundary undercurrent observations at Cape Hatteras. Deep-Sea Res. in press.

Stommel, Henry (1964) Summary charts of the mean dynamic topography and current field at the surface of the ocean, and related functions of the mean wind-stress. Tokyo. Studies on oceanography dedicated to Professor Hidaka, pp. 53-58.

Stommel, Henry (1965) The Gulf Stream. 2nd edn. Berkeley, University of California Press. 248 pp.

Sturges, Wilton (1967) Slope of sea level along the Pacific coast of the United States. J. Geophys. Res., 72, 3627-3637.

Sturges, Wilton (1968) Sea-surface topography near the Gulf Stream. Deep-Sea Res., 15, 149-156.

Sturges, Wilton (1971) Comparison of geodetic and oceanic leveling; comment on accuracy. J. Geophys. Res. in press.

Warren, B.A. and G.H. Volkmann (1968) A measurement of volume transport of the Gulf Stream south of New England. J. Mar. Res., 26(2) 110-126.

Wooster, W.S., and J.L. Reid, Jr., Eastern boundary currents, chapter 11, in The Sea, vol. 2, edited by M.N. Hill, pp. 253-280, Interscience Publishers.

THE ENERGY BALANCE OF WIND WAVES AND THE REMOTE SENSING PROBLEM

K. Hasselmann*

Institute of Geophysics
University of Hamburg

ABSTRACT

Measurements of wave growth during the Joint North Sea Wave Project (JONSWAP) indicate an energy balance of the wave spectrum governed primarily by input from the atmosphere, nonlinear transfer to shorter and longer waves, and advection. The pronounced spectral peak and sharp low frequency cut-off characteristic of fetch-limited spectra are explained as a self-stabilizing feature of the nonlinear wave-wave interactions. The momentum transferred from the atmosphere to the wind waves accounts for a large part of the wind drag. Phillips' 'constant' is found to vary appreciably with fetch and wind speed, the ω^{-5} range of the spectrum representing (for intermediate frequencies not too far from the peak) an equilibrium between atmospheric input and nonlinear transfer rather than a saturation spectrum governed by wave breaking. These findings are relevant for remote microwave sensing of the sea surface by backscatter

---

*Presently at Woods Hole Oceanographic Institution
Woods Hole, Massachusetts 02543
W.H.O.I. Contribution No. 2843

and passive radiometry methods. To first order time averaged microwave signals contain information only on the short-wave region of the surface-wave spectrum, and can be related to the energy-containing long-wave part of the spectrum (the "wind-sea spectrum") only if the dynamical interrelationships between the two wavenumber ranges are properly understood. Signal signatures directly dependent on the wind-sea spectrum can be derived from higher-order backscatter (or emissivity) models, but these also are governed by the hydrodynamical coupling between short and long waves. Delay-time measurements appear to be more closely connected to significant sea-state characteristics. If the illuminated area is large compared with the characteristic wavelength of the surface (the usual case for satellite altimeters), the mean shape of the backscattered radar pulse can be related to the mean square wave height, and further sea state parameters can probably be inferred from a more detailed analysis of the pulse statistics. Interactions between short and long waves are also important in radar altimetery in producing higher-order modifications of the pulse shape which could introduce systematic errors in the measurement of mean sea level. Although JONSWAP demonstrated the significance of wave-wave interactions for the overall energy balance of the wind-sea spectrum, many

details of the spectral equilibrium in the range of high wavenumbers responsible for microwave backscattering still remain to be clarified before microwave techniques can become a reliable tool for the measurement of sea state or the determination of mean sea level to the decimeter accuracies needed for oceanographic applications.

1. INTRODUCTION

Miles' (1957) and Phillips' (1957) important work on wind-wave generation marked the beginning of a fruitful period of theoretical research in ocean wave dynamics. A number of alternative mechanisms of wave growth have since been proposed (e.g. [14] [15] [19] [21] [22] [28] [29] [44] [50]), many of which take more detailed account of the turbulent response characteristics of the atmospheric boundary layer than these first theories. Further theoretical investigations have been concerned with the effects of wave-wave scattering ([20a,b,c] [42] [54] [56]), interactions of waves with currents ([26] [31] [32] [33]), the coupling between short waves and long waves ([24] [29] [43]), white capping ([29] [4]), and other processes. A general summary of most of this work can be found in Phillips' (1966) comprehensive monograph; a more specialised presentation from the viewpoint of weak interaction theory is given in Hasselmann (1968).

Despite these continuing theoretical efforts, however, it is only very recently that field experiments have succeeded in identifying some of the principal features of the overall energy balance of the wave spectrum. Earlier field studies by Snyder and Cox (1966) and Barnett and Wilkerson (1967) revealed that Phillips' and Miles' mechanisms were too weak by almost an order of magnitude to explain the observed wave growth rates. On the basis of a series of wave growth measurements in Hakata Bay and a wind-wave tank, Mitsuyasu ([36a,b] [37] [38]) concluded later that the evolution of the spectrum was strongly influenced by wave-wave interactions as well as the energy transferred from the wind. Extensive large-scale measurements of spectral growth during the Joint North Sea Wave Project (JONSWAP, [5]) have recently confirmed Mitsuyasu's interpretation quantitatively; the characteristic, sharply peaked form of developing wave spectra and the associated rapid growth rates on the forward face of the spectrum could be explained as a self-stabilizing feature of the nonlinear wave interactions. Indirectly, the measurements also yielded an estimate of the energy and momentum transferred from the wind to the waves. The discussion of the energy balance of wind-wave spectra in the first part of this review will accordingly be based primarily on the picture that has evolved from the analysis of the JONSWAP data.

The question of the surface-wave energy balance turns out to be closely related to the problem of remote sea-surface sensing, which is considered in the second part of this paper. One of the goals of remote measurements from satellites is to obtain synoptic data of sea state and, if possible, surface winds as input for wave and weather forecasts. The quality of data needed for this purpose is determined by the numerical prediction model used, which in the case of surface waves is governed by the structure of the spectral energy balance. More importantly, the interpretation of microwave signals emitted or scattered from the sea surface is intimately dependent on the details of the dynamical interactions affecting the energy balance of the wave spectrum. This applies both to measurements of the sea state itself as also to the determination of the wave-induced noise in measurements of other properties of the sea surface, such as the microwave temperature or the mean surface elevation.

The relevance of dynamical processes for the — apparent purely kinematical — problem of determining sea state results from a basic difficulty besetting microwave measurements: the pronounced wavelength mismatch between the sensing radiation and the wave field being sensed. This precludes determining the surface wave spectrum directly by

standard linear scattering methods. To lowest order the backscattered signals (for finite angles of incidence) yield information only on the cm-dm wavelength components of the spectrum. The "wind-sea spectrum" itself (using the term here to denote the wavelength region of the spectrum between about 5 m and 500 m which contains most of the surface wave energy) is accessible to measurement only indirectly through higher order signal characteristics arising from hydrodynamic and electromagnetic interactions between the short scattering waves and longer waves.

We are still far from a complete understanding of the many processes contributing to this coupling. The JONSWAP results indicate that most of the energy received by the short waves is transferred across the spectrum from the longer waves, rather than directly from the atmosphere. Unfortunately, the measurements did not extend to the very short waves in the cm-dm range responsible for microwave scattering. Moreover, this range of the spectrum poses theoretical difficulties in that the coupling of very short waves to the wind-sea spectrum cannot be treated by the resonant interaction theory applicable within the wind-sea spectrum itself (cf. [24]). In particular, it appears that, in contrast to resonant interactions, a consistent treatment of short-long wave interactions must include dissipation and the coupling with the wind. To achieve quantitative microwave measurements of sea state, surface winds, or other sea-

surface properties affected by wave noise, detailed experiments will be needed to extend the picture of the spectral energy balance derived from JONSWAP to the higher wavenumbers in the Bragg scattering range.

2. THE RADIATIVE TRANSFER EQUATION

It is known that to a good approximation wind-generated ocean waves obey the linearized hydrodynamic wave equations for irrotational flow. Linearity implies that the wave field is closely Gaussian [21] and can be fully characterized by its two-dimensional energy spectrum $F(\underset{\sim}{k})$ with respect to horizontal wavenumber $\underset{\sim}{k}$, where

$$\iint_{-\infty}^{\infty} F(k)\, d\underset{\sim}{k} \quad = \text{mean square wave height } \langle \zeta^2 \rangle$$

$$(= \text{wave energy/g.})$$

Experimentally, wave spectra are usually determined through frequency analysis of surface displacements measured at a fixed position, and it is therefore convenient to introduce also the two dimensional spectrum $E_2(f,\theta)$ with respect to frequency $f = \omega/2\pi$ and propagation direction θ, $E_2(f,\theta)\, df d\theta = F(\underset{\sim}{k})\, d\underset{\sim}{k}$. The transformation Jakobian follows from the (deep-water) dispersion relation $\omega = (gk)^{\frac{1}{2}}$: $df d\theta = 2\pi k v^{-1}\, d\underset{\sim}{k}$, where $v = \frac{1}{2}(g/k)^{\frac{1}{2}}$ is the modulus of the group velocity $v_\alpha = \partial\omega/\partial k_\alpha$ $(\alpha = 1,2)$. Integration over the propaga-

tion directions yields the one-dimensional frequency spectrum $E(f) = \int_{-\pi}^{\pi} E_2(f,\theta)d\theta$

Since each "wave packet" of the spectrum propagates with a group velocity appropriate to its wavenumber $\underset{\sim}{k}$, densities at different times t and positions $\underset{\sim}{x}$ in the ocean are interrelated through the spectral energy balance or radiative transfer equation (neglecting refractive effects)

$$\frac{dF(\underset{\sim}{k};\underset{\sim}{x},t)}{dt} \equiv \frac{F}{t} + \underset{\sim}{v}\cdot\Delta F = S \quad . \qquad (1)$$

The left-hand side of the equation expresses the conservation of spectral energy density along the path of a wave group, in accordance with the conservation of energy of individual wave packets as given by the linear, free-wave theory, while the right hand side S represents the net change in energy of the component $\underset{\sim}{k}$ due to all dynamical processes not included in the linear theory. The source function can be represented generally as a superposition

$$S = S_{in} + S_{tr} + S_{ds}$$

of the input S_{in} due to air-sea interactions, a transfer term S_{tr} representing a redistribution of energy within the spectrum conserving total wave energy and momentum, and a dissipation term S_{ds}.

Once the dependence of S on the wave spectrum and

the local wind has been established, the problem of wave prediction for a given wind field reduces to the numerical integration of the radiative transfer equation under appropriate initial and boundary conditions for the wave field. Until recently, however, forecasting methods based on this approach ([2] [3] [18] [45] [47]) have been severely handicapped by lack of quantitative measurements of the wave energy balance, which have made it difficult to decide between a number of strongly differing proposed source-function models, cf [22].

3. THE JOINT NORTH SEA WAVE PROJECT

One of the purposes of JONSWAP was to obtain information about the source function suitable for the needs of practical wave forecasting. A second goal was to gain insight into the relative significance of the various interaction processes contributing to the overall energy balance of the wave field.

To determine rates of change of the wave spectrum, simultaneous wave measurements were made at 13 stations along a 160 km profile extending westward from the island of Sylt in North Germany (Figs. 1 and 2). Half-hourly recordings were made six to twelve times daily for a period of 10 weeks in July-August of 1969; additionally, 4 weeks of data were obtained in September 1968 during a pilot experiment with a

F

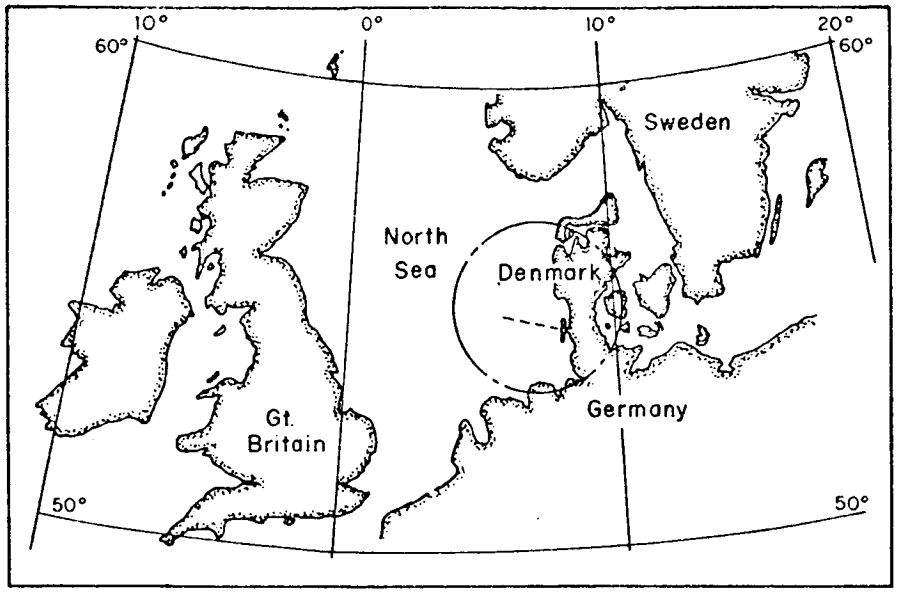

Figure 1. Site of Joint North Sea Wave Project.

STATION	INSTRUMENT	INSTITUTE
1, 2, 3, 5,	WAVE POST	DHI, HAMBURG
4	6 INSTRUMENT WAVE ARRAY	WESTINGHOUSE, SAN DIEGO
7, 9, 10	WAVE RIDER	KMNI, DE BILT
6, 10, 11 12, 13	PITCH AND ROLL BUOY	DHI, HAMBURG NIO, WORMLEY
8	HOT WIRE, CUP AND VANE ANEMOMETERS WAVE POST	GI, HAMBURG DHI, HAMBURG

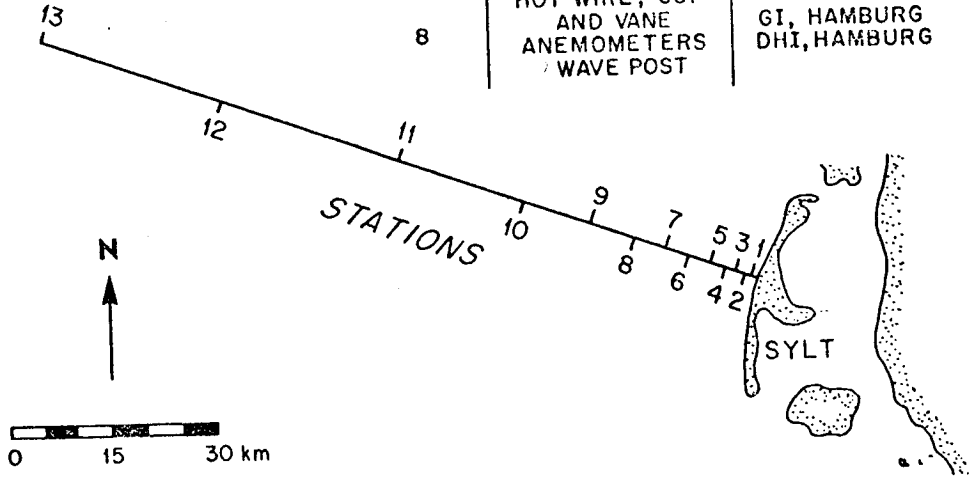

Figure 2. The JONSWAP profile.

reduced profile. A variety of wave recorders, about half of which yielded directional resolution as well as wave heights, were deployed (cf. table, Fig. 2). Extensive measurements were made also of winds, currents, temperatures and other environmental parameters (for a summary of the objectives and logistics of the experiment, cf. Barnett (1970)).

Optimal conditions for studying wave growth obtained when the wind was blowing offshore in a direction parallel to the profile. In this case, cross-profile variations of the wave field were small, and the source function could be evaluated by differentiating the observed spectra with respect to time and the spatial coordinate parallel to the profile.

Figure 3 shows a typical series of one-dimensional spectra measured under these conditions. To summarize the observed growth behavior, the spectra were parametrized by best-fitting an analytic function containing five free parameters. The frequency scale of the fitting function was defined by the frequency f_m at the spectral peak, the ordinate scale α . by adjusting a Phillips (1958, 1966) saturation spectrum $\alpha g^2 (2\pi)^{-4} f^{-5}$ to the high-frequency part of the observed spectrum. The remaining three shape parameters $\sigma_a, \sigma_b, \gamma$ characterized the form of the narrow peak in the transition zone between zero energy at low frequencies and the high-frequency f^{-5} regime.

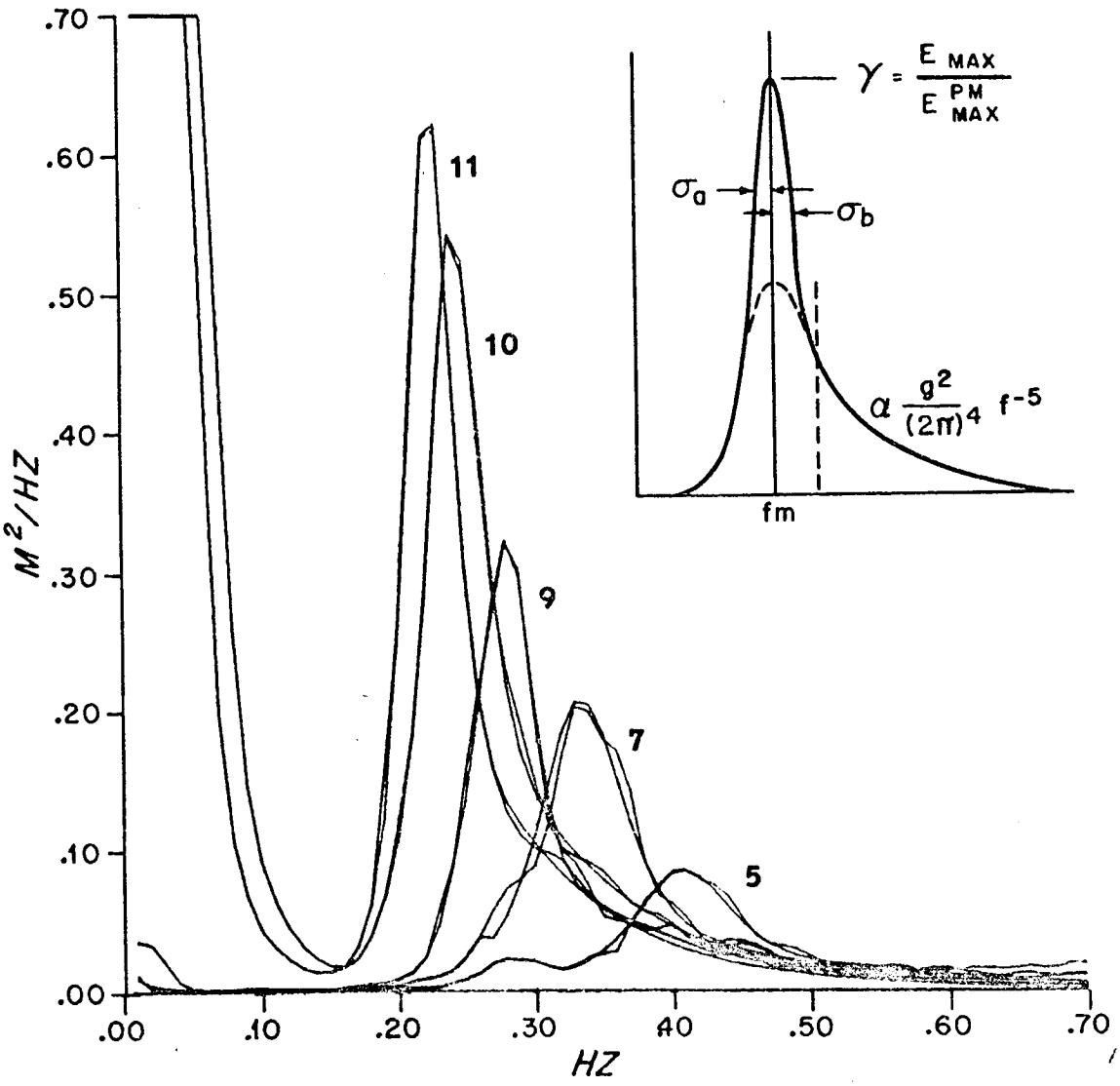

Figure 3. Growth of wave spectra for offshore (east) wind conditions. Fetch increases from Station 5 through Station 9. Best-fit analytic shapes are superimposed on the observed spectra; the five free parameters f_m, α, δ_a, δ_b and $\gamma = E_{max}/E^{P-M}_{max}$ (PM ≡ Pierson-Moskowitz) of the fitting function are indicated in the inset.

In most of the generation cases studied, the time derivative in the energy balance equation was small compared with the convective term. By dimensional arguments, Kitaigorodskii (1962) has shown that the nondimensional wave spectrum $\hat{E}(fu_*/g) = g^{-3}u_*^5 E(f)$ should reduce in this case to a universal function of the nondimensional fetch $\hat{x}$ = (fetch) $\cdot g/u_*^2$, where the friction velocity u_* = (momentum τ transferred across the air-sea interface/density of air)$^{\frac{1}{2}}$. The dependence of the scale parameters on $\hat{x}$ is shown in Fig. 4. Note that α decreases with $\hat{x}$, in contrast to Phillips' original dimensional argument, which predicts a universally constant α. This is in accordance with the interpretation of the source function given below which indicates that the f^{-5} dependence in this part of the spectrum is not dominated by white capping, as assumed by Phillips, but rather by a balance between the energy input from the atmosphere and the energy transfer to other wave components through wave-wave interactions.

The shape parameters showed considerable scatter, but no systematic variation with fetch [5]. Within the uncertainties of this variability (attributed to the gustiness of the wind), the wave spectra could be regarded as self similar over the range of fetches of the experiment.

The smoothed dependence of the five spectral parameters on nondimensional fetch $\hat{x}$ defined a mean evolution of

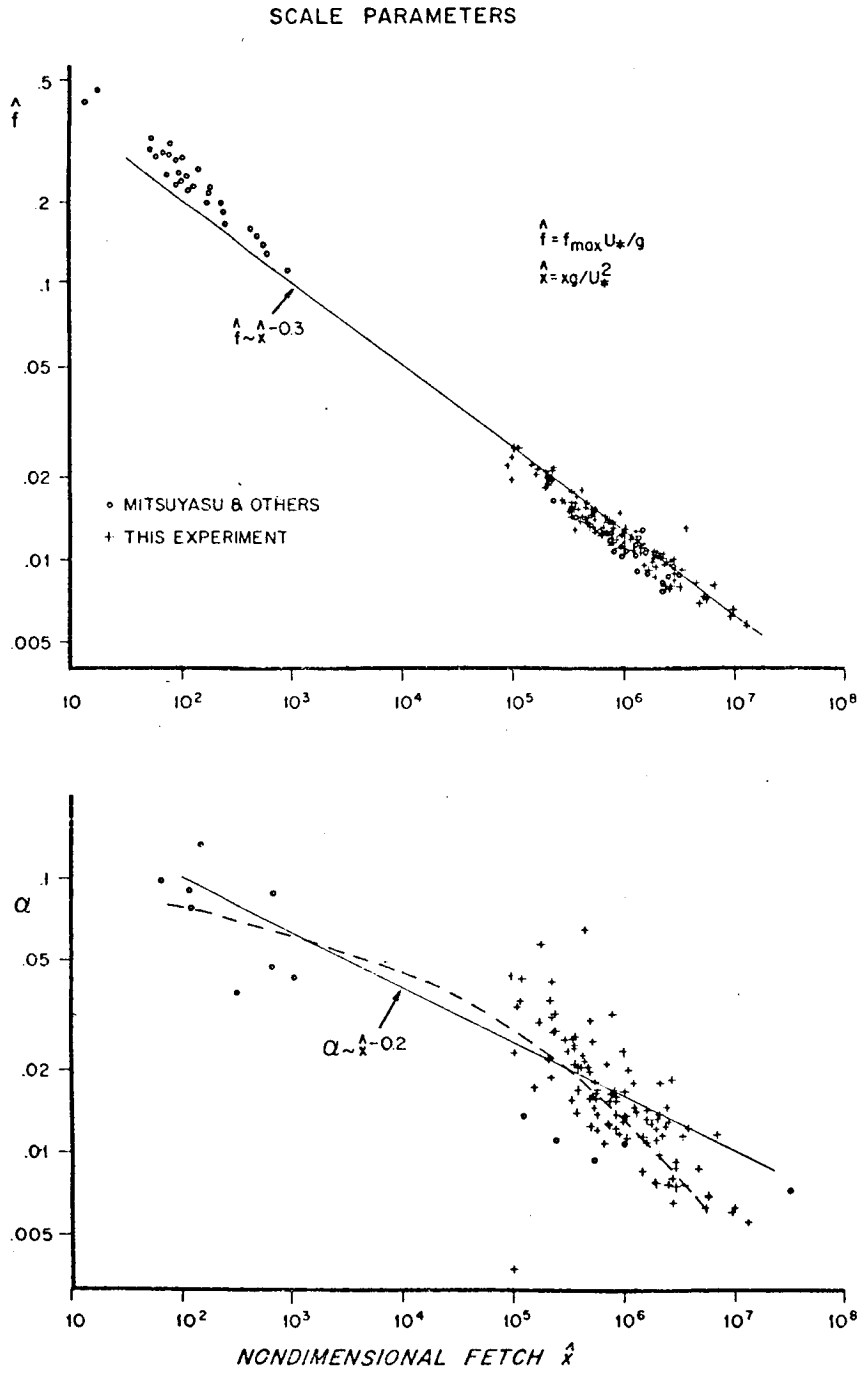

Figure 4. Variation of scale parameters with nondimensional fetch. The friction velocity is taken as $u_* = (1.2.10^{-3})^{\frac{1}{2}} U_{10}$. ($U_{10}$ = wind speed at 10 m height above the mean surface.)

of the spectrum, from which a mean source function was then determined through the energy balance equation (1). The characteristic +- distribution of the source function (cf. Fig. 5) is due to the shift of the spectral peak towards lower frequencies. The positive lobe corresponds to the rapid wave growth on the forward face of the spectrum; after the peak has passed to lower frequencies, the components on the right of the peak then decay again before approaching a quasi-stationary equilibrium value (cf. also Fig. 3).

4. THE ENERGY TRANSFER DUE TO WAVE-WAVE INTERACTIONS

This "overshoot" phenomenon has been observed independently by several workers in field and laboratory experiments ([6] [7] [36a,b] [37] [53]). Barnett and Sutherland (1968) suggested nonlinear wave-wave interactions as a possible explanation, a conjecture which later found some support by Mitsuyasu's (1968) estimates of the nonlinear transfer rates for a decaying spectrum in a wave tank. The calculations were based on Barnett's (1968) parametrization of the Boltzmann scattering integrals computed in Hasselmann [20c]. Exact computations of the nonlinear transfer integrals for a number of JONSWAP spectra ([5] [50]) have confirmed that the principal features of the observed source function can indeed be explained by resonant wave-wave interactions: Fig. 5 shows that both the overshoot and the

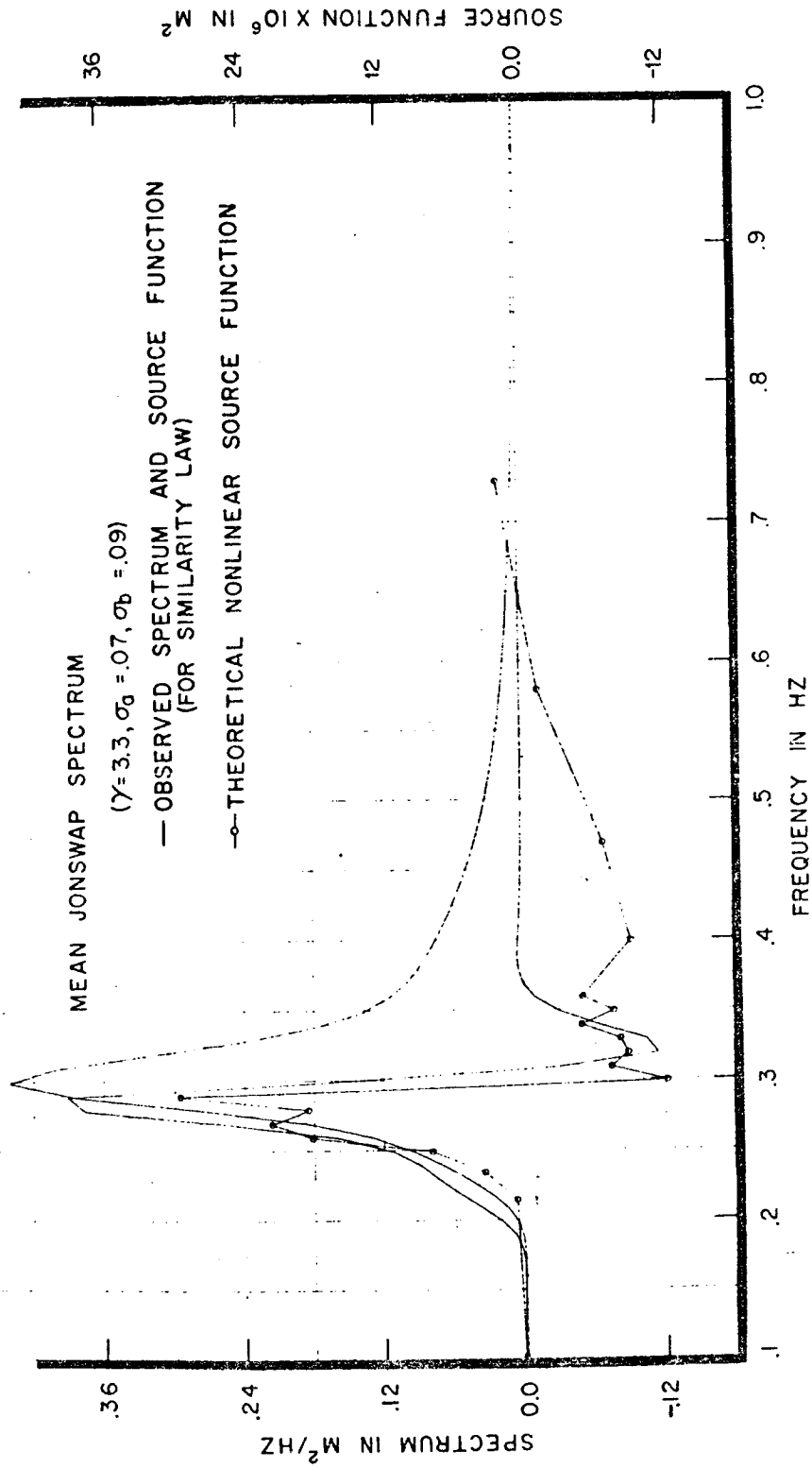

Figure 5. Mean JONSWAP spectrum, empirical mean source function, and the nonlinear energy transfer as computed from the mean JONSWAP spectrum. A $\cos^2\theta$ spreading function was assumed. The curves shown here for a particular windspeed and fetch remain valid for all windspeeds and fetches if the axes are scaled appropriately.

major part of the rapid growth on the forward face of the spectrum can be attributed to the nonlinear transfer.

The basic mechanism of the process is illustrated in Fig. 6. According to the classical theory of lowest order Bragg scattering, an incident wave i can be refracted by a sinusoidal disturbance c (e.g., one of the harmonics of a periodic lattice, or a second wave component) into a scattered wave s, provided some form of nonlinear coupling exists between c and the incident and scattered waves, and the three components satisfy the Bragg relations for constructive interference (resonance)

$$\begin{aligned} \sigma_i \omega_i + \sigma_c \omega_c &= \omega_s \\ \sigma_i k_i + \sigma_c k_c &= k_s \qquad (\sigma_i \sigma_c = \pm) \end{aligned} \tag{2}$$

It can be shown that these conditions cannot be satisfied by three gravity wave components — or in general by any three waves having the same dispersion relation for which the curvature $d^2\omega/dk^2$ is negative throughout. However, Bragg scattering can occur at second order. On account of weak nonlinear interactions, the spectrum of surface displacement continues not only free-wave components (ω, $\underset{\sim}{k}$) but also all combinations of quadratic harmonics ($\omega_1 \pm \omega_2$, $\underset{\sim}{k}_1 \pm \underset{\sim}{k}_2$) generated by pairs of free waves (ω_1, $\underset{\sim}{k}_1$), (ω_2, $\underset{\sim}{k}_2$) (plus cubic and higher order harmonics of correspondingly smaller amplitude).

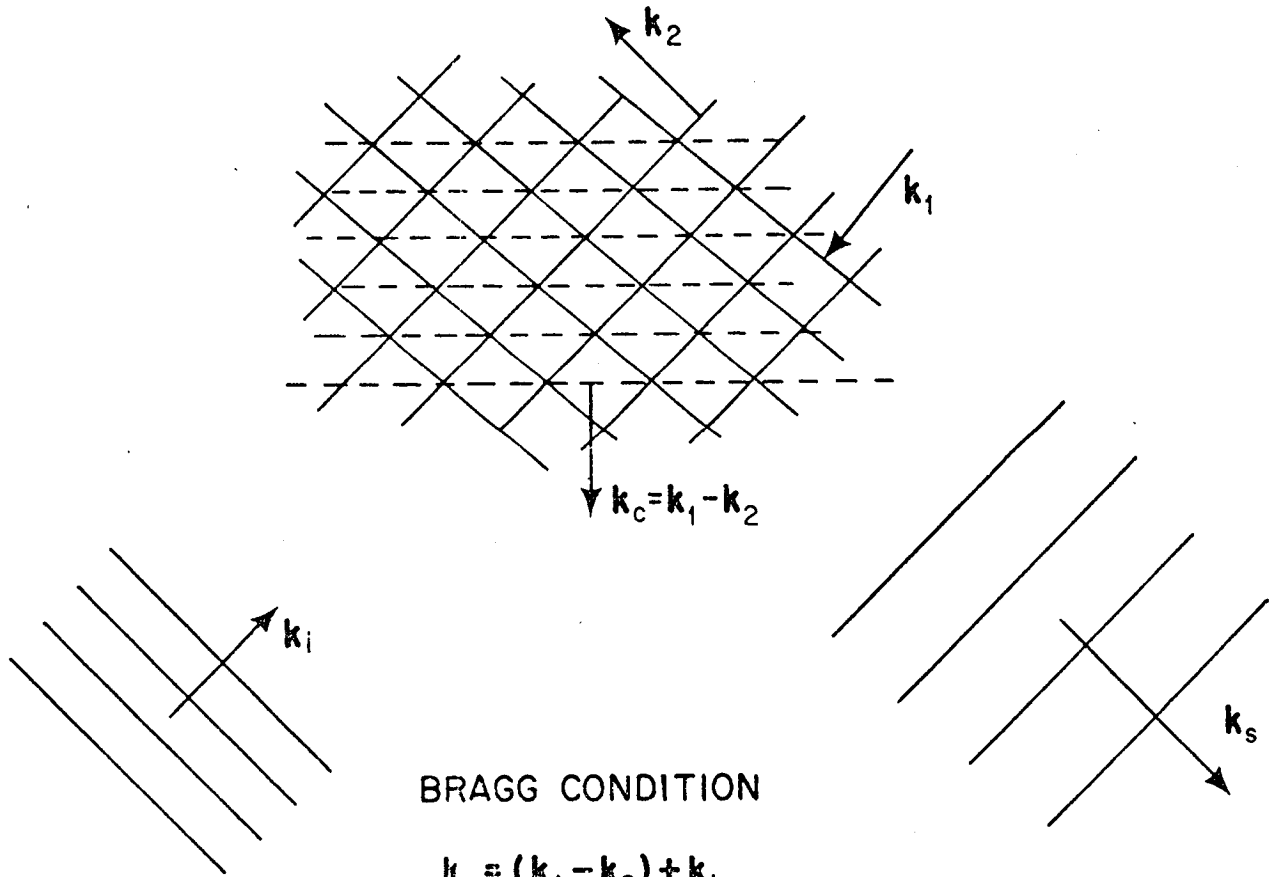

Figure 6. Second-order Bragg scattering (cubic wave-wave interactions).

These forced, non-propagating components can act as the component c in Fig. 6 coupling the free incident wave i to the scattered free wave s . For the lowest order interaction with a quadratic harmonic, the Bragg condition is accordingly given by ([20a] [42])

$$\sigma_i\omega_i + \sigma_1\omega_1 + \sigma_2\omega_2 = \omega_s$$

$$\sigma_i\underset{\sim}{k}_i + \sigma_1\underset{\sim}{k}_1 + \sigma_2\underset{\sim}{k}_2 = \underset{\sim}{k}_s$$

The net coupling is cubic in the wave amplitudes, the scattered wave s being generated by a quadratic interaction between the free incident wave i and the forced wave c , which itself is produced by a quadratic interaction between two free waves 1 and 2. For a continuous spectrum, the summation over all possible interactions of this kind yields an energy transfer rate given by a Boltzmann integral over combinations of cubic products of the spectral densities at the four wavenumbers occurring in each scattering process ([20a]). The structure of the integral is rather complex, and it has not been possible to find a simple explanation for the particular form of the nonlinear transfer rates computed for the different cases shown, for example, in Figs. 5 and 7. The H theorem, which states generally that wave-wave scattering changes the spectrum irreversibly in the direction towards a uniform

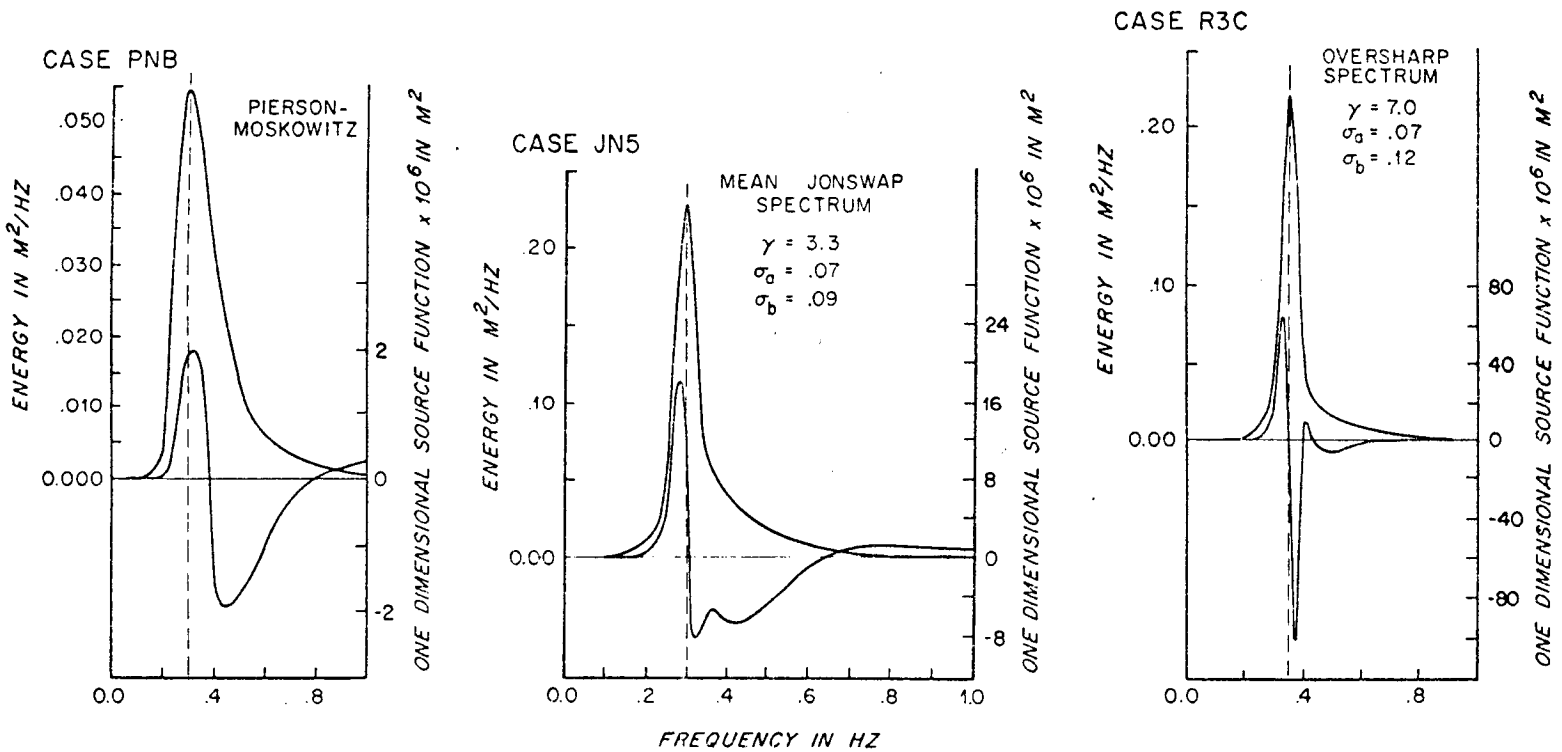

Figure 7. Nonlinear transfer rates computed for three differently peaked spectra. The flatter peak on the left (corresponding to a Pierson-Moskowitz spectrum) is growing, whereas the sharper peak on the right is broadening and shifting towards lower frequencies. The mean JONSWAP spectrum in the center corresponds to the stable case in which the peak shifts without appreciable change in shape. Computations are based on $\cos^2\theta$ spreading factors.

energy distribution in wavenumber space, in conjunction with the constraints of momentum, energy and — in this case — action conservation, explain the general +-+ distribution of the nonlinear source function [20b], but not the positions of the individual lobes, which turn out to be essential for the stability of the spectral shape.

5. THE OVERALL ENERGY BALANCE

It follows from the computed nonlinear transfer rate shown in Fig. 5 that for a spectrum of the general JONSWAP form wave-wave interactions will produce a shift of the peak towards lower frequencies at about the rate observed. However, this says nothing about the origin of the peak, or its persistence once it has been generated. To resolve these questions, computations of the nonlinear energy transfer were made for a series of spectral shapes which were either broader or more sharply peaked than the mean JONSWAP spectrum. It was found that the peak appears to be a self-sustaining feature of the nonlinear energy transfer which evolves from almost any initial spectral distribution, independent of the details of the energy input.

As an example, the left panel in Fig. 7 shows the nonlinear transfer for a spectrum with a less pronounced peak than the mean JONSWAP spectrum. Characteristic for these broader distributions (in this case a Pierson-Moskowitz spectrum) is the position of the positive lobe

of the nonlinear source function directly beneath the spectral maximum, causing the peak to grow. As the peak develops, the positive lobe moves towards the forward face of the spectrum until a stage is reached, corresponding roughly to the mean JONSWAP spectrum, where the peak no longer grows but merely shifts towards lower frequencies without appreciable change in shape (2nd panel). For a still sharper peak, shown in the third example, the source function develops two positive lobes immediately adjacent to a strong negative lobe beneath the spectral maximum, and the peak broadens again.

The evolution of this self-stabilizing spectral shape does not appear to be affected qualitatively by the details of the energy input from the atmosphere or the dissipation; these determine the energy level of the spectrum and the rate at which the nonlinear transfer causes the peak to wander towards lower frequencies, but not the basic form of the energy distribution resulting from the combination of the three source terms.

The probable decomposition of the net source function S into its three constituents S_{in}, S_{tr} and S_{ds} is shown in Fig. 8. Of the four terms in the equation

$$S = S_{in} + S_{tr} + S_{ds}$$

only the terms S (measured) and S_{tr} (computed)

were determined quantitatively. These define also the sum $S_{in} + S_{ds}$, but the further separation into the individual contributions S_{in} and S_{ds} shown in Fig. 8 is somewhat speculative. Fortunately, the ambiguity is somewhat restricted in this case by the side condition that the total momentum transferred from the atmosphere to the wave field cannot exceed the total momentum transferred across the air-sea interface, which is reasonably well known from flux measurements in the atmospheric boundary layer (also made during JONSWAP). Assuming negligible energy dissipation in the main part of the spectrum, as in Fig. 8, the net transfer of momentum from the atmosphere to the wave field is found to account for 50% ±30% of the total momentum lost from the atmosphere. (Since the ratio of momentum to energy for each wave component is equal to $\underset{\sim}{k}/\omega$, the spectral momentum transfer to the waves is given by $S_{in} \cdot \underset{\sim}{k}/\omega \cdot A \cos^2\theta$. angular distribution was assumed in carrying out the integration.) Dobson (1971) and Synder (personal communication) also found that a major part of the momentum lost by the atmosphere enters the wave field. If dissipation is added to the energy balance, the atmospheric input has to be increased accordingly in order for the sum $S_{in} + S_{ds}$ to remain constant. Clearly, a very large dissipation is not acceptable within the limitations set by the total transfer across the air-sea interface.

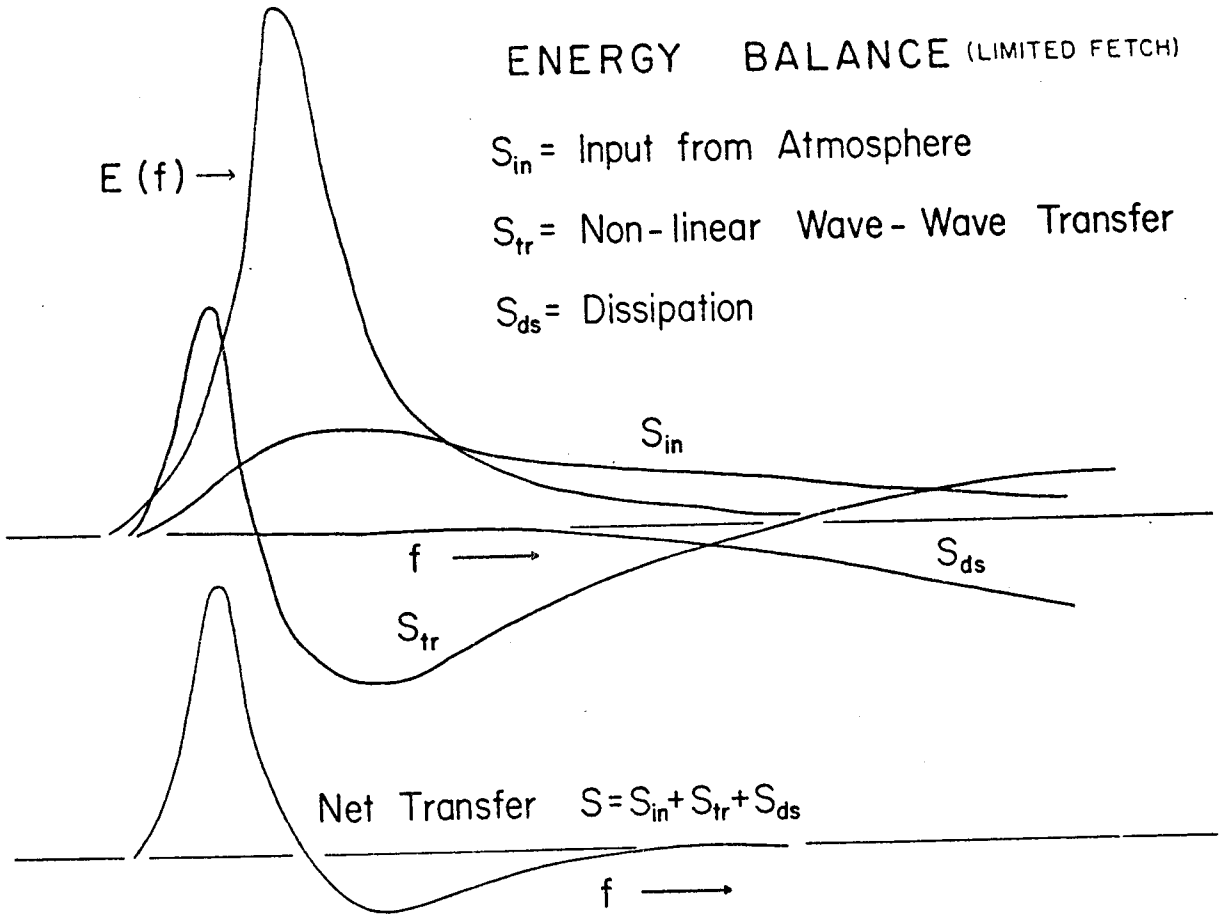

Figure 8. Decomposition of the measured total source function $S = S_{in} + S_{tr} + S_{ds}$ into its individual constituents. S, S_{tr} and $(S_{in} + S_{ds})$ can be either measured or computed, but the separation of $S_{in} + S_{ds}$ into components is tentative (see text).

According to this picture, the development of the wave spectrum for finite fetches is governed primarily by the energy balance between the atmospher input S_{in} and the nonlinear transfer of energy S_{tr} from the main part of the spectrum to lower and higher frequencies. Under stationary conditions the low-frequency energy generated by wave-wave interactions is convected away, $\underset{\sim}{V}\cdot\nabla F \approx S_{tr}$, whereas at high frequencies the energy gain due to the nonlinear transfer and the atmospheric input has to be balanced by some dissipative mechanism. About 10% of the total momentum transferred across the air-sea interface is convected away by the low-frequency waves. This can be deduced from the increase of the total momentum of the wave field with fetch, independent of the source function analysis. Between 15 and 60% of τ is accounted for by the nonlinear transfer* of momentum from the main part of the spectrum to shorter waves (f> 0.7 Hz in Fig. 5), where it is converted to current momentum by dissipation. Again, this estimate is independent of details of the energy balance, following alone from the nonlinear transfer rates computed for the observed spectra. To balance these momentum fluxes, about 50% ±30% of the momentum transferred across the air-sea interface must be entering the wave field in the central region of the spectrum.

---

* The uncertainty reflects the sensitive dependence of these computations on the spectrum.

Several questions remain unanswered in this description. Although the inferred momentum transfer rate from the atmosphere to the wave field can be shown to scale in accordance with a linear process [5], as predicted by the majority of wave-generation theories, and yields a drag coefficient independent of wind and fetch, as generally observed, the actual mechanism of wave generation by wind has not been determined. The existence of an asymptotic, fully developed spectrum at very large fetches is another open point. Without some mechanism for extracting energy from very long waves, the nonlinear transfer would continue to generate longer and longer waves indefinitely. Possible candidates for a long-wave energy sink are the attenuation by the wind of waves traveling at phase speeds exceeding the wind speed, which has found some support in recent laboratory experiments [51], or the transfer of energy from long waves to very short waves (which lie beyond the range of resonant-interaction theory) via WKBJ interactions [24]. The latter process is also relevant for a third unresolved problem, the form of the energy balance at high wavenumbers. Since 70% ±20% of the momentum flux to the waves is transferred to short waves via the long waves and wave-wave interactions, a significant energy and momentum sink is needed at high wavenumbers. Valenzuela (1971) has shown

that for very short waves energy can be rapidly transferred to higher wavenumbers through gravity-capillary interactions, which satisfy the Bragg resonance conditions already at second order (cf. Phillips, 1966). In this case, the energy sink could be viscosity acting on extremely short waves. Estimates indicate that this could remove all the energy supplied to the wave field for wind speeds up to a few m/s, but at higher winds energy is presumably lost over a broader band of wavenumbers through white capping. The resolution of these questions is fundamental for the application of microwave techniques, which sense primarily the very short surface waves and are therefore critically dependent on the ability to predict the energy level in this wavenumber range as a function of the wind-sea spectrum and the local wind speed.

6. STATISTICAL DESCRIPTION OF BACKSCATTER

In order to discuss further the implications of wave dynamics for the remote sensing problem, we first review briefly the concepts and models developed to interpret microwave measurements of the sea surface. It is found that these models lead naturally to the same questions that arose in the consideration of the wave energy balance. For simplicity, we restrict the discussion to active microwave techniques. Microwave temperature measurements are also

strongly influenced by the wave field, but the passive emission problem is rather analagous to the scattering case in the sense that similar interaction models are applicable in both instances.

Space measurements of sea surface backscatter are best made in the cm-dm wavelength band in order to combine good beam resolution with weak transmission losses in the atmosphere. Synoptic coverage of the sea surface over distances extending to several thousand kilometers can also be achieved with land stations using decameter waves reflected from the ionosphere. It has been shown that at these wavelengths the higher-order doppler side bands of the sea echo can be related theoretically to the one-dimensional frequency spectrum of the wave field ([23] [25] [8]). The interactions in this case involve relatively long wind waves and are reasonably well understood. However, we restrict ourselves here to microwave techniques applicable to satellites; unfortunately, these are governed by interactions in the less studied and dynamically more complicated high wavenumber region of the surface wave spectrum.

The backscattered return from pulsed microwave emission contains statistical amplitude, phase and travel time information, which can be largely summarized in terms of the second moments of the signal. In the particular case that the process is Gaussian, these provide a complete statisti-

cal description of the backscattered return. According to the Central Limit Theorem, this will approximately apply (independent of the sea-surface statistics) if the footprint diameter is large compared with the correlation scale of the scatterers — a condition which is often satisfied in satellite applications. However, an interesting technique exploiting non-Gaussian properties of backscattered modulated microwaves [48] is mentioned in §8. In this case the non-Gaussian signature, although small, can be readily filtered out of the much larger Gaussian components. Useful sea-state information can also be obtained from the initial return characteristics of altimeter pulses, which correspond to the non-Gaussian, small footprint limit (§9). The non-Gaussian properties of these signals have not been systematically investigated, but a preliminary inspection indicates that they are related to useful wavelength distributions of the wind-sea not contained in the second moments of the signal.

A backscattered microwave pulse centered at the frequency ω_o may be expressed in the form

$$v(t;\tau) = B(t;\tau)e^{i\omega_o t}$$

where $B(t;\tau)$ is a random complex modulation factor (complex envelope) depending on the delay time t relative to the time of emission τ of the pulse. For fixed τ, $B(t)$ defines the shape of the backscattered pulse, the

(much slower) variation of pulse shape with τ arising then through the time dependence of the backscattering surface. Assuming that the scattering process is statistically stationary with respect to τ and that the phase distribution of B is statistically uniform, the first moment of B vanishes and the second moments are given by

$$\langle B(t_1, \tau'+\tau)\, B^*(t_2,\tau')\rangle = R(t_1,t_2,\tau)$$

$$\langle B(t_1, \tau'+\tau)\, B(t_2,\tau')\rangle = 0$$

The ensemble averages $\langle \cdot \cdot \cdot \rangle$ may be interpreted here also as time means with respect to τ'.

The doppler spectrum of the general second moment is defined as the Fourier transform

$$T(t_1, t_2, \omega) = \frac{1}{2\pi} \int_{-\infty}^{\infty} R(t_1, t_1, \tau) e^{-i\omega\tau} d\tau.$$

T depends on both the shape of the emitted pulse and the statistical properties of the scattering surface. The two effects may be separated by introducing the scattering function, which describes the (input independent) second-moment statistics of the time-varying "channel" representing the backscattering sea surface, cf [17].

In terms of the complex envelope $A(t)$ of the transmitted pulse, the received pulse can be expressed in the

general form

$$B(t, \tau) = \int_{-\infty}^{\infty} x(t', \tau) A(t-t') dt'$$

where the linear filter $x(t, \tau)$ represents the distortion of the pulse due to the backscattering surface. The second moment of the signal is therefore given by

$$R(t_1, t_2, \tau) = \iint_{-\infty}^{\infty} \langle x(t', \tau'+\tau) x^*(t'', \tau') \rangle A(t_1-t') A^*(t_2-t'') dt' dt''$$

For most scattering models (including the ones discussed here) the autocorrelation of the filter function is significantly non-zero only for time differences $t' - t''$ of the order of the carrier period. Hence in integrating over the much longer pulse duration the second moment of x may be approximated by a σ -function,

$$\langle x(t', \tau'+\tau) x^*(t'', \tau') \rangle = P(t', \tau) \delta(t'-t'')$$

which yields

$$R(t_1, t_2, \tau) = \int_{-\infty}^{\infty} A(t_1-t') A^*(t_2-t') P(t', \tau) dt'$$

or, in terms of the doppler spectra,

$$T(t_1, t_2, \omega) = \int_{-\infty}^{\infty} A(t_1-t') A^*(t_2-t') S(t', \omega) dt'$$

where

$$S(t, \omega) = \frac{1}{2\pi}\int_{-\infty}^{\infty} P(t,\tau)e^{-i\omega\tau}d\tau$$

is the scattering function.

Neither measurements nor a comprehensive theoretical analysis of the complete doppler spectrum or scattering function for a random sea surface appear to have been attempted. Published investigations have considered either the scattering cross sections i.e., the mean power of the backscattered pulse

$$\sigma = \iint T(t,t,\omega)dt\ d\omega$$

and its doppler decomposition

$$f(\omega) = \int T(t,t,\omega)dt\ ,$$

both of which average out the travel time information (and can therefore be determined from CW-type measurements), or alternatively the mean pulse power

$$I(t) = \int T(t,t,\omega)d\omega$$

as a function of delay time, which makes no use of the doppler information.

Cross-section and doppler measurements are normally made at finite angles of incidence, whereas travel-time data has been obtained largely from altimeters operating at near normal incidence. Different scattering models are

found to be valid in each of these ranges of incident angle, so that the following discussion of backscatter models will naturally tend to emphasize the type of measurement associated with a given model. However, it is conceivable that a more detailed investigation of the properties of the complete doppler spectrum or scattering function would reveal valuable additional sea state signatures not discernible in the usual measurements but nonetheless accessible by standard linear signal processing techniques.

7. THE SPECULAR REFLEXION AND BRAGG SCATTERING MODELS

The simplest description of surface scattering is the specular reflexion of an ensemble of rays by a statistical distribution of infinitesimal surface facets, as originally applied by Cox and Munk [12] [13] to the analysis of sun glitter from the sea surface. For microwaves, the model is applicable for angles of incidence less than about 20° from the vertical. At larger angles, specular reflexion becomes negligible and the backscatter is dominated by first-order Bragg interactions in accordance with the resonance conditions (2). These define two backscattering surface-wave components with wavelengths equal to half the horizontal wavelength of the incident radiation, propagating towards or away from the microwave source.

Both models are found to be in good accord with obser-

vations in their regions of theoretical validity (cf [9] [10] [49] [57]), but yield only limited information on the wind-sea spectrum in terms of the cross sections and doppler spectra, cf. table 1 (the application of the specular reflexion model to altimeter data is discussed in §9). The Bragg model determines only the wave spectrum at the two (very high) Bragg wavenumbers. The specular reflexion model yields the mean square wave slope and vertical orbital velocity, of which only the latter moment (determining the doppler bandwidth) is significantly dependent on the principal wind-sea components. However, it should be noted that the theoretical doppler spectra apply to the idealized case of a parallel incident beam. In operation from a moving satellite, the finite beam angle of a real scatterometer would lead to variable doppler shifts due to the platform motion which would normally mask the wave-induced doppler spectrum.

Two courses may be pursued to overcome the limitations of the lowest-order models. Firstly, interrelationships may be established between the accessible high wavenumber range of the spectrum, the wind-sea spectrum and the local surface wind. In this respect it is encouraging that the high-frequency range of the spectrum does not appear to represent a universal equilibrium governed solely by white-capping, but contains a free energy factor governed, among other processes, by the coupling to the principal wind-sea

Table 1

	geometric reflexion	Bragg scattering
Cross section σ	$\dfrac{\exp\{-\phi^2/2\langle n_{/\!/}^2\rangle\}}{2\pi\ \lvert\langle n_\alpha n_\beta\rangle\rvert^{/\!/2}}$	$k_3^4\ T(\phi)\,[F(\underset{\sim}{k}_g)+F(-\underset{\sim}{k}_g)]$
Doppler spectrum $f(\omega)$	$\dfrac{\phi\ \exp\{-\omega^2/8k_3^2\langle u_3^2\rangle\}}{(8\pi k_3^2\langle u_3^2\rangle)^{\frac{1}{2}}}$	$k_3^4 T(\phi)\,[F(\underset{\sim}{k}_g)\,\delta(\omega-\omega_g)+ F(-\underset{\sim}{k}_g)\,\delta(\omega+\omega_g)]$

ϕ = angle of incidence

k_3 = vertical wavenumber component of incident wave

$n_\alpha = \dfrac{\partial\zeta}{\partial x\alpha}$ = wave slope , $\langle n_\alpha n_\beta\rangle = \int F(\underset{\sim}{k})\,k_\alpha k_\beta\,d\underset{\sim}{k}$

$n_{/\!/}$ = wave slope parallel to horizontal direction of incident ray

$\underset{\sim}{k}_g = -2\underset{\sim}{k}_i$ = wavenumber of Bragg scattering surface waves

$\omega_g = (gk_g)^{\frac{1}{2}}$

u_3 = vertical orbital velocity

$\langle u_3^2\rangle = \int F(\underset{\sim}{k})\,gk\,d\underset{\sim}{k}$

components. As pointed out in §5, however, many details of the spectral energy balance at very high wavenumbers still need to be resolved. Several of the inconsistencies in the reported wind dependences of microwave and acoustic cross-sections or in the values of Phillips' constant are presumably due to inadequate consideration of all factors influencing the high-wavenumber equilibrium (cf. [1] [11] [29] [34] [39] [44] [46] [55]).

It has not always been sufficiently appreciated in this context that an observed wind dependence of backscatter cross-sections or Phillips' constant necessarily implies a dependence on further parameters by dimensional arguments alone, independent of detailed dynamical considerations. If the surface-wave spectrum is expressed in terms of a generalised Phillips' form $E_2(f,\theta) = \alpha(f,\theta) g^2 (2\pi)^{-4} f^{-5}$,

the non-dimensional form factor α can depend (besides on the non-dimensional direction θ) only on non-dimensional combinations of f and various external parameters such as the wind speed u , the fetch x , and g . Thus if it is assumed that these are the only relevant external variables and α is observed to be independent of f (Phillips' power law), it can be a function only of the non-dimensional combination xg/u^2 (Kitaigorodskii's similarity relation); the determination of wind dependence is meaningful in this case only if the fetch is defined.

For large fetches, α should then attain an asymptotic value independent of wind speed. If a variation of α with wind speed is nevertheless observed for large fetches, this implies either that Phillips' power law is invalid (the wind dependence corresponding in this case to an inverse frequency dependence through the dimensional condition $\alpha = \alpha(uf/g)$, or that additional dimensional factors (e.g. surface tension or contamination) are involved. It follows generally that the wind dependence cannot be investigated consistently without regard to the other parameters which determine the energy level of the wave spectrum at high wavenumbers.

The second, more direct course is to develop higher-order interaction models which predict backscatter signatures dependent not only on the short scattering waves, but also on the longer wind-wave components. Progress in this direction may indeed be a prerequisite for the success of the first approach, for even after the interrelationship between the high-wavenumber energy, the wind-sea spectrum and the wind speed has been clarified, knowledge of the high wavenumber range of the spectrum alone will probably prove insufficient to solve for the remaining two factors determining the equilibrium without additional data on the longer wind-sea components.

C2

8. THE WAVE-FACET INTERACTION MODEL

Two straightforward generalisations of the lowest order scattering models have been investigated. In the first case, the perturbation expansion in terms of surface wave height, which yields Bragg scattering to first order, is extended to quadratic and higher powers. The second order wave-wave interaction theory yields a useful description of backscatter at decameter wavelengths or longer([23] [25] [8]), but is of only limited value in the microwave band, since for short wavelength radiation the principal wind-sea components violate the basic interaction condition (surface wave height)/(electromagnetic wavelength) << 1.

This difficulty is avoided in the composite-wave or wave-facet interaction model, which is based on an alternative two-scale expansion method (cf [9] [10] [49] [57]). In this case the Bragg scattering waves are assumed to be superimposed on a random ensemble of longer carrier waves (the wind sea), which are represented locally by plane facets of dimension small compared with the wind-sea wavelength but large compared with the wavelength of the Bragg waves. It is then assumed that Bragg theory can be applied as before in the local reference system of the moving, inclined facet. Modifications of the Bragg return arise both through changes in the angle of incidence and the orientation of the polarisation planes relative to the local

facet normal (electromagnetic interactions) and through the amplitude and wavelength modulation of the Bragg scattering waves as they propagate through the variable orbital currents and vertical accelerations of the carrier waves (hydrodynamic interactions). The model is meaningful only if these modifications are large compared with the errors incurred through the indeterminacy relations (i.e. the Fraunhofer patterns) in restricting the area of the Bragg scattering waves to a finite facet rather than an infinite plane. The condition may be expressed as $k_3 \zeta >> |$ [25] where k_3 is the vertical wavenumber component of the incident radiation and ζ is the wave height.

Theoretical investigations of the wave-facet model have been restricted hitherto to the electromagnetic interactions. Except for rather low grazing angles (less than about 20°), these are not found to appreciably affect the backscatter cross-sections. Moreover, the modifications are proportional to the mean square wave slopes, which are only weakly dependent on the main part of the wind-sea spectrum. Stronger effects are found in the doppler spectra, the wind-sea signatures here being determined by the mean square orbital velocities and the mean products of the orbital velocities and wave slopes [25], both of which represent spectral moments weighted towards the principal components of the wind-sea spectrum. In prin-

cipal, doppler measurements could therefore yield independent estimates of, say, the mean wave height and mean period of the sea. However, apart from the aforementioned difficulties in resolving wave-induced doppler shifts from satellites, the theoretical predictions must be regarded as qualitative until the hydrodynamic interactions, which are generally of order comparable with the electromagnetic interactions, are incorporated in the model. This would not only be useful for the interpretation of the doppler spectra, but may also enhance the value of cross-section data by the prediction of new types of signatures (such as the upwind/downwind asymmetry, cf. [24]), which may be more readily distinguishable from the unmodulated Bragg return than the modifications induced by electromagnetic interactions alone.

Perhaps the strongest argument for developing a quantitative wave-facet interaction model including both types of interaction is the recent interesting proposal to determine the complete wind-sea spectrum by means of sinusoidally modulated microwaves (Ruck et al, (1972) — a similar suggestion was made also in an earlier unpublished communication by W.S. Ament). The power emitted by a microwave beam consisting of the superposition of two monochromatic waves with closely neighboring frequencies and horizontal wavenumbers (ω_1, $\underset{\sim}{k}_1$) and (ω_2, $\underset{\sim}{k}_2$),

respectively, may be represented as a D.C. term and a superimposed sinusoidal modulation at the difference frequency and wavenumber ($\omega_m, \underset{\sim}{k}_m$) = ($\omega_1 - \omega_2, \underset{\sim}{k}_1 - \underset{\sim}{k}_2$). (It is assumed here that the power is averaged over a period large compared with ω_1^{-1} but small compared with ω_m^{-1} .) On account of its finite frequency ω_m , the modulation term can be readily filtered from the mean power. Thus separated, the value of the fluctuating beam as a wave probe follows primarily from its sinusoidal spatial variation. Assuming that the Bragg scattering surface waves were essentially homogeneous over scales large compared with the modulation wavelength $\lambda_m = 2\pi/|\underset{\sim}{k}_1 - \underset{\sim}{k}_2|$, the modulated backscattered return, integrated over an illuminated area of dimension large compared with λ_m , would average to effectively zero. However, if the Bragg-scattering surface waves are themselves modulated by long wind-sea components, the product of the modulated incident power and the modulated backscatter cross-section yields a non-vanishing contribution on integration over the illuminated area. If the modulation of the Bragg scattering waves is linear with respect to the wind sea, which appears a reasonable first approximation, the modulated microwave acts as a filter extracting the modulating wind-sea component at the wavenumber $\underset{\sim}{k}_m$. Since the effect is linear in the (statistical) surface wave amplitudes, the ensemble average of

the backscattered power at the frequency ω_m would still vanish. (The filter separating the modulated power from the D.C. term must, of course, be sufficiently wide to include the small doppler broadening due to the waves — or the platform motion.) However, the mean square power at ω_m is non-zero and is proportional to the wind-sea energy spectrum at $\underset{\sim}{k}_m$. (It may be noted that this corresponds to a mean fourth product of the signal amplitudes which could not be inferred from mean quadratic quantities — essentially the mean power — and must therefore represent a non-Gaussian effect. In accordance with the Central Limit Theorem it can be shown that for large areas of illumination the modulated term is small compared with the D.C. term, which has Gaussian statistics.)

By varying the difference frequency and azimuth angle, the technique basically provides a measurement of the complete two-dimensional wind-wave spectrum, with the exception of a sign ambiguity in the direction of wave propagation. However, the method is critically dependent on the determination of the coupling coefficients characterising the modulation of the Bragg return by the spectral components of the wind-sea. The electromagnetic contribution to these interactions can be readily calculated, but the hydrodynamic terms are governed by the same long-short wave interactions that arose in discussions of the energy

balance in §§5 and 7. They can be treated formally by the WKBJ method appropriate to the two-scale approximation of the wave-facet model (cf.[24]), but as pointed out above, a basic difficulty of the theory is that a complete analysis requires, among other processes, the inclusion of dissipative losses due to white capping and the regeneration of short waves by wind, both of which are only poorly known. As before, we conclude that significant progress in the determination of sea state from cross-section data requires detailed experiments to clarify the various processes determining the short-wave energy balance.

9. RADAR ALTIMETRY

The analysis of microwave backscatter signals with respect to delay time yields wave information of a basically different nature from that obtained from time-averaged cross-section or doppler data. Thus with the simplest form of signal treatment, altimeters provide a measurement of the mean square wave-height, a basic characteristic of the wave field which was not accessible to direct measurement by CW methods.

On reflection from the sea surface, an initially step-function pulse is transformed to a pulse with the familiar average shape shown in Fig. 9. If the sea surface is almost calm (except for very small slope variations which broaden the average reflection of a unidirectional ray into

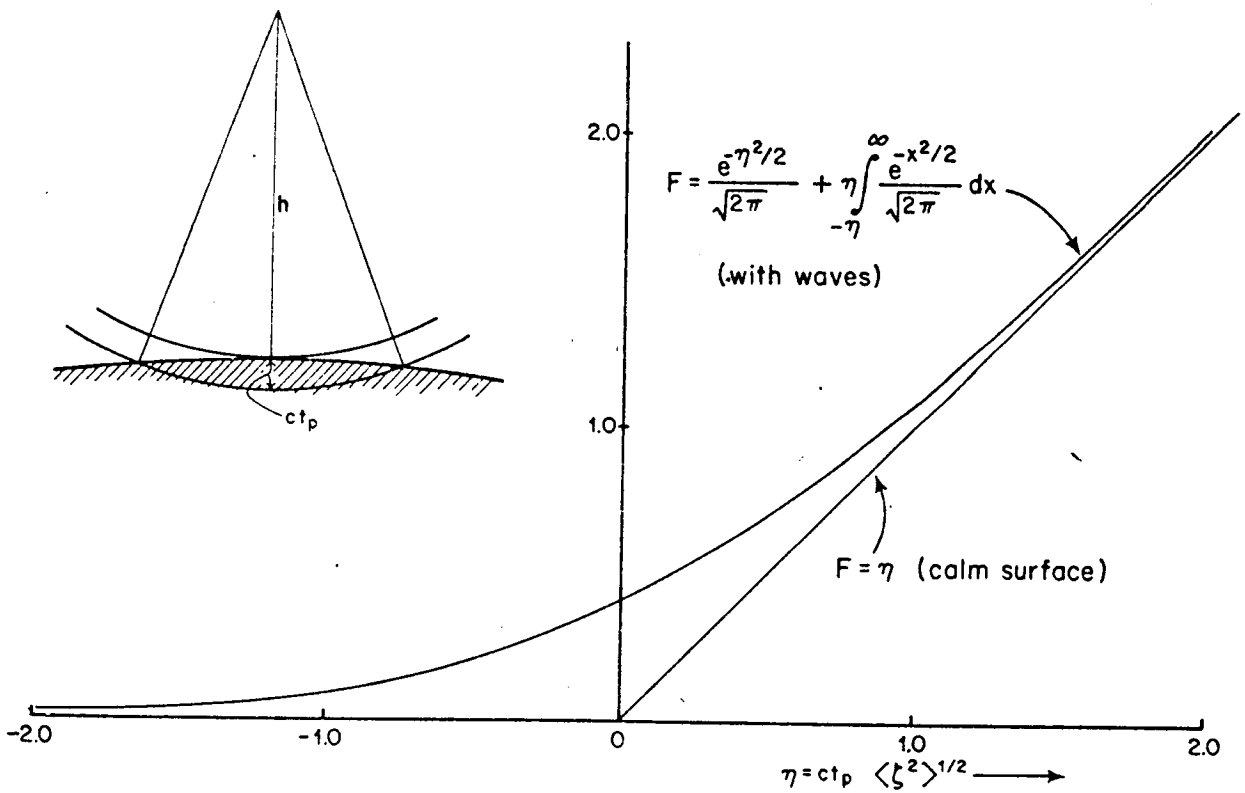

Figure 9. Mean shape (in power) of incident step-function pulse on reflexion from sea surface. The wave field smooths the corner of the linear-ramp response for a calm surface. Solutions for a square pulse are obtained by subtracting a second, identical step-function solution displaced in time.

a narrow but finite angular beam, so that all points within the footprint reflect equal power back to the source) the returned power I at a given delay time $t_d = \frac{2h}{c} + 2t_p$ is proportional to the area of the footprint. For small footprint diameters relative to the source height h, the area increases linearly with the penetration time t_p (cf. Fig. 9), so that

$$I = \begin{cases} 0 \text{ for } t_p \leq 0 \\ \alpha t_p \text{ for } t_p \leq 0 \end{cases} \qquad (3)$$

where the constant α is determined by geometric factors and the mean square wave slope, in accordance with the specular reflexion model valid for normal incidence (cf. table 1). The case of a square-shaped initial pulse follows from the step-function solution (including the modifications considered below) by subtracting a second, identical solution displaced in time.

In the presence of waves, the sharp break at the onset of the reflected pulse is smoothed through the early arrivals of energy reflected from the crests of waves before the pulse reaches the mean sea surface. The modification of the reflected pulse shape contains useful sea state information, but tends also to degrade measurements of the mean sea surface elevation. Particularly important for the latter problem is the question whether the pulse distortion

is indeed limited only to the pulse onset (and the second corner terminating the linear ramp in the square-pulse case) or whether the entire pulse is affected. If the wave signature is restricted to the pulse corners, it can be largely eliminated from the mean surface measurement by extrapolation of the linear regime; if not, a correction must be applied to the entire pulse, and its magnitude can be computed only if the wave field is known.

According to the specular reflexion model, the mean CW power reflected vertically from an infinitesimal area dA is given by

$$dI = \beta\, P_2(\underset{\sim}{n})_{\underset{\sim}{n}=0} dA \qquad (4)$$

where β is a geometrical constant and $P_2(\underset{\sim}{n})$ the probability distribution of facet slopes $\underset{\sim}{n} = \left(\frac{\delta\zeta}{\delta x_1}, \frac{\delta\zeta}{\delta x_2}\right)$ In the case of a step-function pulse, power is received at the delay time t_d only if the reflecting facet lies within a sphere of radius $R = ct_d/2$. from the source, or in terms of the penetration time t_p and footprint diameter $r = (2hct_p)^{\frac{1}{2}}$, if the surface displacement

$$\zeta \geq \hat{\zeta}(r', t_p) = (r'^2 - r^2)/2h$$

where r' is the radial distance of the element dA from the foot of the surface normal passing through the source. Thus the expression (4) must be replaced in this case by

$$dI = \beta \int_{\zeta}^{\infty} P_s(\zeta, \underset{\sim}{n})\, d\zeta dA$$

where $P_3(\zeta,\underset{\sim}{n})$ is the joint probability distribution of surface slopes and displacements. Integrating over the surface, the backscattered power is thus given by

$$I = \beta\int_0^\infty 2\pi r'\left[\int_\zeta^\infty P_3(\zeta,\underset{\sim}{n})_{\underset{\sim}{n}=o}\,d\zeta\right]dr' \qquad (5)$$

For a Gaussian wave field, the surface slopes and heights are statistically independent, since

$$\langle\zeta\underset{\sim}{n}\rangle = \langle\zeta\nabla\zeta\rangle = \nabla\langle\zeta^2/_2\rangle = 0$$

on account of the statistical homogeneity. Hence

where
$$P_3(\zeta,\underset{\sim}{n}) = P_1(\zeta)P_2(\underset{\sim}{n}) \ ,$$
$$P_1(\zeta) = (2\pi\langle\zeta^2\rangle)^{-\frac{1}{2}}\exp\left\{-\zeta^2/2\langle\zeta^2\rangle\right\}$$

Substituting in equation (5), the integrations can be preformed explicitly, yielding

$$I = \alpha\langle\zeta^2\rangle^{\frac{1}{2}}c^{-1}\{(2\pi)^{-\frac{1}{2}}\exp(-\eta^2/_2) + \eta\phi(\eta)\} \qquad (6)$$

where $\eta = ct_p/\langle\zeta^2\rangle^{\frac{1}{2}}$, $\phi(\eta) = \int_\eta^\infty e^{-\eta'^2/_2}\,d\eta'$

denotes the error function and α is the same constant as in equation (3).

We note that the shape of the pulse onset shown in Fig. 9 is the same for all sea states, equation (6) depending on the wave field only through the single scaling

parameter $\langle \zeta^2 \rangle$.

A preliminary analysis indicates that further useful parameters of the wind-sea, including wavelength information, can be obtained from a more detailed analysis of the complete doppler spectrum and higher order signal moments. However, the dependence of these functions on the wind-wave spectrum is highly nonlinear, so that the inversion of the functional relations presents a nontrivial mathematical problem which can probably be solved only numerically with the aid of parametrised representations of the wind-wave spectrum.

According to the solution (6), the wave field affects only the onset of the reflected pulse, the asymptotic pulse shape approaching the calm-surface solution (3) (as, of course, must be the case if the solutions for all sea states, including the limit $\langle \zeta^2 \rangle \to 0$, differ only by a scale factor). Although this result appears encouraging for the measurement of mean sea surface, it is a particular consequence of the Gaussian hypothesis, with its corollary of statistically independent wave slopes and surface heights. In the non-Gaussian case, the asymptotic pulse shape is in general parallel to, but offset from, the calm-surface solution. Physically, if the mean square wave slopes tend to be higher on the wave crests than in the troughs, the average energy reflected vertically from the

wave crests is smaller than from the troughs, and the mean backscattered power is biased towards greater delay times. Thus a linear extrapolation of the asymptotic pulse response defines a virtual onset time corresponding to a calm-surface elevation lower than the true mean surface. For significant correlations between the wave height and the wave slope squared the systematic error introduced in this manner could become of the order of the r.m.s. wave height. Although this will normally not exceed the achievable resolution of currently planned space altimeters, it could become serious should the sought-for dm resolution needed for most oceanographic applications (tides, geostrophic surface slopes, wind set up, etc.) become attainable. The correction for these errors will require not only measurements of the wave field but also an understanding of the coupling between the long wind-sea components and the shorter waves contributing to the mean square slope — which is essentially the same two-scale interaction problem that has been mentioned repeatedly above.

10. CONCLUSIONS

Microwave measurements from space hold considerable promise of yielding valuable synoptic data on sea state and surface winds. However, the interaction between microwaves and the surface is highly complex and poses several fundamental questions which require further extensive study

before the techniques can be usefully applied. Investigations are needed particularly in two areas:

(1) A detailed theoretical analysis of the complete doppler spectrum (or scattering function) and the non-Gaussian properties of backscatter signals may be expected to reveal additional useful sea-state signatures not contained in the traditional cross-section, doppler and travel-time measurements. This applies particularly to the backscatter statistics for radar altimeters, which appear to be intimately related to the wind-sea spectrum.

(2) Higher-order models of the radar return from the sea surface are strongly dependent on the interactions between very short waves and the longer wind-sea components. A second basic input for these models is the energy level of the wave spectrum at high wavenumbers. Both questions represent interrelated aspects of the energy balance of the short-wave region of the spectrum, and can be understood only through detailed measurements covering several decades of surface wavelengths from a few cms to several hundred meters. A broad-band wave experiment of this nature, combined with radar backscatter data — supplemented, if possible, by microwave-temperature and acoustic backscatter measurements as independent tests of the theoretical models— would be very helpful in clarifying some of the basic mechanisms involved in the interpretation of microwave backscatter from the sea surface.

REFERENCES

1. Bachmann, W. and B. de Raignac (1971) The calculation of the surface backscattering coefficient of underwater sound from measured data. SACLANTCEN Techn. Mem.No. 174

2. Baer, L. (1963) An experiment in numerical forecast of deep water ocean waves. Lockheed Missile Space Co., LMSC-801296

3. Barnett, T.P. (1968) On the generation, dissipation and prediction of wind waves. J. Geophys. Res. 73, 513-534

4. Barnett, T.P. (1970) Wind waves and swell in the North Sea. EOS 51 544-550

5. Barnett, T.P., E. Bouws, H. Carlson, D. Cartwright, J.A. Ewing, H. Gienapp, D.E. Hasselmann, K. Hasselmann, P. Krusemann, A. Meerburg, K. Richter, W. Sell and H. Walden (1971) Measurements of wind-wave growth and swell decay in the North Sea (Joint North Sea Wave Project - JONSWAP), AGU, Washington, April 1971, and IUGG, Moscow, Aug. 1971 (to be published in Deutsche Hydrogr. Zeitschrift)

6. Barnett, T.P. and J.C. Wilkerson (1967) On the generation of wind waves as inferred from airborne radar measurements of fetch-limited spectra. J. Mar. Res. 25, 292-328

7. Barnett, T.P. and A.J. Sutherland (1968) A note on the overshoot effect in wind-generated waves. J. Geophys. Res. 73, 6879-6884

8. Barrick, D.E. (1971) Dependence of second-order doppler side bands in HF sea echo upon sea state, G-AP Internat. Symp. Digest

9. Barrick, D.E. and W.H. Peake (1968) A review of scattering from surfaces with different roughness scales. Radio Sci. 3, 865-868

10. Bass, F.G., I.M. Fuks, A.I. Kalmykov, I.E. Ostrovsky and A.D. Rosenberg (1968) Very high frequency radiowave scattering by a disturbed sea surface. IEEE Trans., AP-16, 554-568

11. Chapman, R.P. and J.H. Harris (1962) Surface back-scattering strengths measured with explosive sound sources. J. Acoust. Soc. Am. 34, 1592-1597

12. Cox, C.S. and W.H. Munk (1954) Statistics of the sea surface derived from sun glitter. J. Mar. Res. 13, 198-227

13. Cox, C.S. and W.H. Munk (1954b) Measurements of the roughness of the sea surface from photographs of the sun's glitter. J. Optical Soc. Amer. 44, 838-850

14. Davis, R.E. (1969) On the high Reynolds number flow over a wavy boundary. J. Fluid Mech. 36, 337-346

15. Davis, R.E. (1970) On the turbulent flow over a wavy boundary. J. Fluid Mech. 42, 721-731

16. Dobson, F.W. (1971) Measurements of atmospheric pressure on wind-generated sea waves. J. Fluid Mech. 48, 91-127

17. Evans, V.U. and T. Hagfors (1968) Radar astronomy. McGraw Hill Book Co.

18. Ewing, J.A. (1971) Paper on wave prediction - to appear in Deutsche Hydrogr. Zeitschr. 24 (6)

19. Hasselmann, D.E. (1971) Wave generation by resonant Case-mode interactions in a turbulent wind. AGU, Washington, April 1971 (publ. in preparation)

20. Hasselmann, K. On the non-linear energy transfer in a gravity-wave spectrum.

    a. (1962) Part 1: General Theory. J. Fluid Mech. 12, 481-500

    b. (1963) Part 2: Conservation theorems, wave-particle correspondence, irreversibility. J. Fluid Mech. 15, 273-281

    c. (1963) Part 3: Computation of the energy flux and swell-sea interaction for a Neumann spectrum. J. Fluid Mech. 15, 385-398

21. Hasselmann, K. (1967) Nonlinear interactions treated by the methods of theoretical physics (with application to the generation of waves by wind) Proceedings of the Royal Society, A, 299, 77-100

22. Hasselmann, K. (1968) Weak-interaction theory of ocean waves, Basic developments in fluid dynamics (Editor, M. Holt) 2, 117-182

23. Hasselmann, K. (1971) Determination of ocean wave spectra from doppler radio return from the sea surface. Nature 229, 16-17

24. Hasselmann, K. (1971) On the mass and momentum transfer between short gravity waves and larger-scale motions. J. Fluid Mech. 50, 189-206

25. Hasselmann, K. and M. Schieler (1970) Doppler spectra of electromagnetic backscatter from the sea surface at centimeter-decimeter and decameter wavelengths; Proceedings VIIIth Naval Hydrodyn. Symp., Pasadena

26. Kenyon, K.E. (1971) Wave refraction in ocean currents. Deep-Sea Res. 18, 1023-1034

27. Kitaigorodski, S.A. (1962) Applications of the theory of similarity to the analysis of wind-generated wave motion as a stochastic process. Bull. I.Z.V. Geophys. Ser. 1, 73-80

28. Long, R. (1971) On generation of ocean waves by a turbulent wind. Diss., Univ. Miami, 1971

29. Longuet-Higgins, M.S. (1969) A nonlinear mechanism for the generation of sea waves. Proc. Roy. Soc. A. 311, 371-389

30. Longuet-Higgins, M.S. (1969) On wave breaking and the equilibrium spectrum of wind-generated waves. Proc. Roy. Soc. A 310, 151-159

31. Longuet-Higgins, M.S. and R.W. Stewart (1960) Changes in the form of short gravity waves on long waves and tidal currents. J. Fluid Mech. 8, 565-583

32. Longuet-Higgins, M.S. and R.W. Stewart (1961) The changes in amplitude of short gravity waves on steady non-uniform currents. J. Fluid Mech. 10, 529-549

33. Longuet-Higgins, M.S. and R.W. Stewart (1964) Radiation stresses in water waves; a physical discussion, with applications. Deep-Sea Res. 11, 529-562

34. Marsh, H.W. (1963) Sound reflection and scattering from the sea surface. J. Acoust. Soc. Am. 35, 240-244

35. Miles, J.W. (1957) On the generation of surface waves by shear flows. J. Fluid Mech. 3, 185-204

36. Mitsuyasu, H. On the growth of the spectrum of wind-generated waves.

a. (1968) (I) Rep. Research Inst. Appl. Mech., Kyushu Univ. 16, 459-482

b. (1969) (II) Rep. Research Inst. Appl. Mech., Kyushu Univ. 17, 235-248

37. Mitsuyasu, H. (1968) A note on the nonlinear energy transfer in the spectrum of wind-generated waves. Rep. Research Inst. Appl. Mech. Kuyshu Univ. 16, 251-264

38. Mitsuyasu, H., R. Nakayama and T. Komori (1971) Observations of the wind and waves in Hakata Bay. Rep. Research Inst. Appl. Mech. Kyushu Univ. 19, 37-74

39. Moore, R.K., J.P. Claassen, A.K. Fung. S. Wu and H.L. Chan (1971) Toward radscat measurements over the sea and their interpretation. Remote Sensing Lab., Univ.

40. Phillips, O.M. (1957) On the generation of waves by turbulent wind. J. Fluid Mech. 2, 417-445

41. Phillips, O.M. (1958) The equilibrium range in the spectrum of wind-generated waves. J. Fluid Mech. 4, 426-434

42. Phillips, O.M. (1960) On the dynamics of unsteady gravity waves of finite amplitude. Part I. J. Fluid Mech. 9, 193-217

43. Phillips, O.M. (1963) On the attenuation of long gravity waves by short breaking waves. J. Fluid Mech. 16, 321-32

44. Phillips, O.M. (1966) "The Dynamics of the Upper Ocean". Camb. Univ. Press, London and New York

45. Pierson, W.J. (1970) The integration of remote sensing data into global weather prediction, wave forecasting, and ocean circulation computer based systems. New York Univ., NASA-MSC Review

46. Pierson, W.J., F.C. Jackson, R.A. Stacy, and E. Mehr (1971) Research on the problem of the radar return from a wind roughened sea. Contr. No. 117, Geophysic. Sciences Lab., Dept. Met. Ocean., New York Univ., Bronx, N.Y.

47. Pierson, W.J., L.J. Tick and L. Baer (1966) Computer based procedure for preparing global wave forecasts and wind field analysis capable of using wave data obtained by a space craft. 6th Naval Hydrodynamic Symposium, Washington, Office of Naval Res., Washington, D.C.

48. Ruck, G., D. Barrick, T. Kalisvewski (1972) Bistatic radar sea state monitoring. Batelle Tech. Rep., Columbia Lab., Ohio

49. Semenov, B. (1966) An approximate calculation of scattering on the perturbed sea surface. IVUZ Radiofizika (USSR) 9, 876-887

50. Sell, W. and K. Hasselmann (1972) Computations of nonlinear energy transfer for JONSWAP and empirical wind wave spectra. Rep. Inst. Geophysics, Univ. Hamburg

51. Shemdin, O.H. and R.H. Lai (1971) Laboratory investigation of turbulence above waves. IUGG, Moscow, Aug. 1971

52. Snyder, R.L. and C.S. Cox (1966) A field study of the wind generation of ocean waves. J. Mar. Res. 24, 141-178

53. Sutherland, A.J. (1968) Growth of spectral components in a wind-generated wave train. J. Fluid Mech. 33, 545-560

54. Valenzuela, G.R. (1971) Non-linear energy transfer in gravity-capillary wave spectra. AGU Fall Meeting, San Francisco, Dec. 1971 (to be published)

55. Valenzuela, G.R., M.B. Laing and J.C. Daley (1971) Ocean spectra for the high frequency waves as determined from airborne radar measurements. J. Mar. Res. 29, 69-84

56. Valenzuela, G.R. and M.B. Laing (1970) Study of doppler spectra of radar sea echo. J. Geophys. Res. 75, 551-563

57. Wright, J.W. (1968) A new model for sea clutter. IEEE Trans. AP-16, 217-223

TIDES AND TSUNAMIS

N73-15096

Bernard D. Zetler

National Oceanic and Atmospheric Administration
Atlantic Oceanographic and Meteorological Laboratories
Physical Oceanography Laboratory
Miami, Florida 33130

Abstract

Although tides and tsunamis are both shallow water waves, it does not follow that they are equally amenable to an observational program using an orbiting altimeter on a satellite. Therefore, the physics of each is considered in an effort to evaluate the feasibility of successful measurement from space. Because tide analysis requires a multiplicity of orbits, absolute accuracy is important but a constant bias is acceptable. A numerical feasibility investigation using a hypothetical satellite orbit, real tide observations, and sequentially increased levels of white noise has been conducted to study the degradation of the tidal harmonic constants caused by adding noise to the tide data. Tsunami waves, possibly a foot high and one hundred miles long, must be measured in individual orbits, thus requiring high relative resolution.

Although the state of the art must be significantly improved for both tides and tsunamis, it appears that tides are more likely to be successfully studied from space in the foreseeable future.

1. INTRODUCTION

Inasmuch as both tides and tsunamis are shallow water waves (wave length much greater than water depth), there may be a tendency to assume that there is an equal potential for monitoring these from space. However, this does not follow because there are significant differences in the physics of these phenomena. Accordingly, some consideration of each is necessary for arriving at an evaluation of the potential for monitoring from spacecraft.

2. TIDES

There are some distinctive features that differentiate tides from most, if not all, other geophysical phenomena. An energy spectrum for most parameters is a continuum which peaks in one or more frequency bands; tides have a line structure and the frequencies of the lines are very accurately determined from astronomical data. The phases for each of these lines are locked into astronomical events and the signal to noise ratio is usually very high. Finally, it can be assumed that the Q of the ocean response to tide-

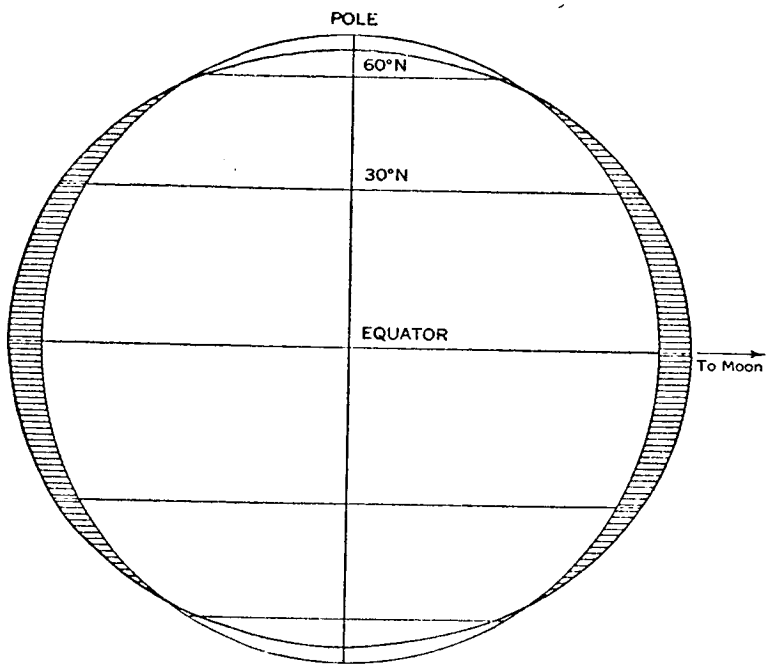

Figure 1. Tide with moon on equator.

producing forces is not large and therefore it can be assumed that the ocean responds smoothly over a narrow frequency band.

To calculate the important frequencies in the tide, oceanographers start with an equilibrium theory whose assumptions are obviously invalid. These include a uniformly deep water mass over all of the earth (no continents or shoal areas) and no friction so that the waters respond immediately to tide-producing forces.

If we first consider an earth-moon two-body system with the moon rotating around the earth in a circular orbit in the plane of the earth's equator (Figure 1), there are two areas of high tide, one directly under the moon and the other on the opposite side farthest from the moon. In between

these two bulges is a trough girdling the earth and connecting the poles. The two high tides are most easily understood by considering the forces acting on the earth. At any point there is an attractive force to the center of the earth that depends on the mass of the moon and inversely as the square of the distance. If that was the only force, the earth and moon would be drawn together. There is also a centrifugal force acting in the opposite direction along the line of centers of the moon and the earth. The amount of this centrifugal force is equal and opposite to the gravitational attraction but, unlike the latter, is equal and in the same direction for all points on the earth. Therefore, although the vectorial sum of the two forces at the center of the earth is zero, along the line of centers there is a net force toward the moon on the earth's surface directly under the moon, and a net force away from the moon on the opposite side. Calculations show that this difference (tide-producing) force varies inversely as the cube of the distance to the center of the moon.

Although the above simplified explanation implies a vertical lifting of the sea surface, actually the high tide is formed by a very small horizontal component of the vector for all points not on the line of centers which is unopposed whereas the lifting force is opposed by the gravitational pull toward the center of the earth.

As the earth rotates on its axis, a point on the earth's surface experiences two high tides and two low tides each lunar day (note that the moon is also rotating around the earth in a period of about a month). The tidal constituent described here, with a period of about 12.42 hours, is called M_2, the M for the moon and the subscript for the cycles per day.

The moon does not really have a circular orbit around the earth, but rather an elliptical orbit that is closest to the earth as a point called perigee and farthest at apogee. Therefore the attractive force will vary, being greatest at perigee and smallest at apogee. Tidal scientists cope with this by concocting a second moon and placing it also in a circular orbit around the earth. They select a period about 12.66 hours, so that the resulting force, named constituent N_2, will be exactly in phase with M_2 at perigee and exactly in opposite phase with it at apogee, thus modulating the M_2 force over the period of a lunar month.

A similar treatment is designed for the solar forces, with the principal solar constituent (period 12 hours) labeled as S_2. Thus when M_2 and S_2 are in phase at new and full moon, we have spring tides (larger than average) and, since M_2 and S_2 are exactly opposed at quadrature, there are neap tides (smaller than average) at these times. If spring tides and perigean tides coincide, the range is even

greater whereas if neap and apogean tides coincide, there are particularly small ranges at these times.

In his opening remarks, Dr. Stewart mentioned unusually large tides occurring at the time of this meeting. Not only are M_2, S_2 and N_2 in phase, but another constituent K_2 is also. K_2 modulates the S_2 constituent in a six month period, being in phase with S_2 at the time of the equinoxes.

Thus far, the moon has been constrained to the plane of the earth's equator whereas it actually has extreme declinations, both north and south, of as much as $28\frac{1}{2}^{\circ}$. Figure 2 shows the tidal configuration of the earth with the moon at extreme north declination. As the earth rotates, a point experiences two high tides of different heights (high water inequality). This can be considered as a diurnal tide superimposed on the semidiurnal tide. To simulate a diurnal tide that is large at extreme declination and small (or zero) when the moon is on the equator, two diurnal constituents, K_1, and O_1, are introduced. These two have circular orbits of about 23.93 and 25.82 hours respectively, so that they are in phase at extreme declination and opposed a week later when the moon is on the equator. Furthermore, the sum of their hourly speeds (in degrees per hour) exactly equals the M_2 speed so that the phase relationship of the principal semidaily and daily tide remains fixed although the amplitude relationship varies over a 14-day period.

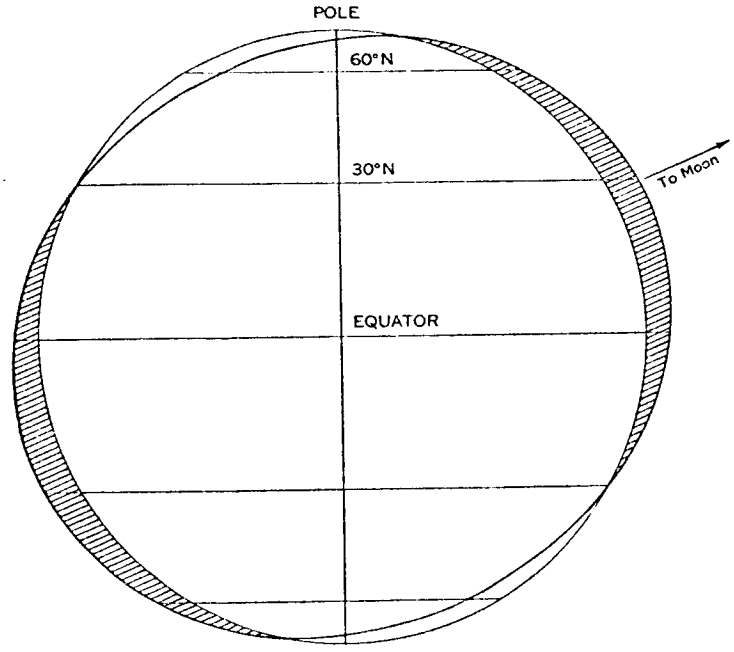

Figure 2. Tide with moon at extreme declination.

Although the initial assumptions of equilibrium theory are invalid, i.e. there are large land masses, complex ocean bathymetry and friction, nevertheless we do learn the important astronomical periods and the theoretical phases of the tidal constituents. Hence we can imperically analyze sets of tide observations for amplitude and phase lags (called tidal harmonic constants). We can then synthesize these same constituents (sum of a set of cosine curves) to obtain tide predictions for another period.

Traditionally this has been done on mechanical tide prediction machines. Figure 3 shows the machine used by the Coast and Geodetic Survey from about 1910 to 1965. The

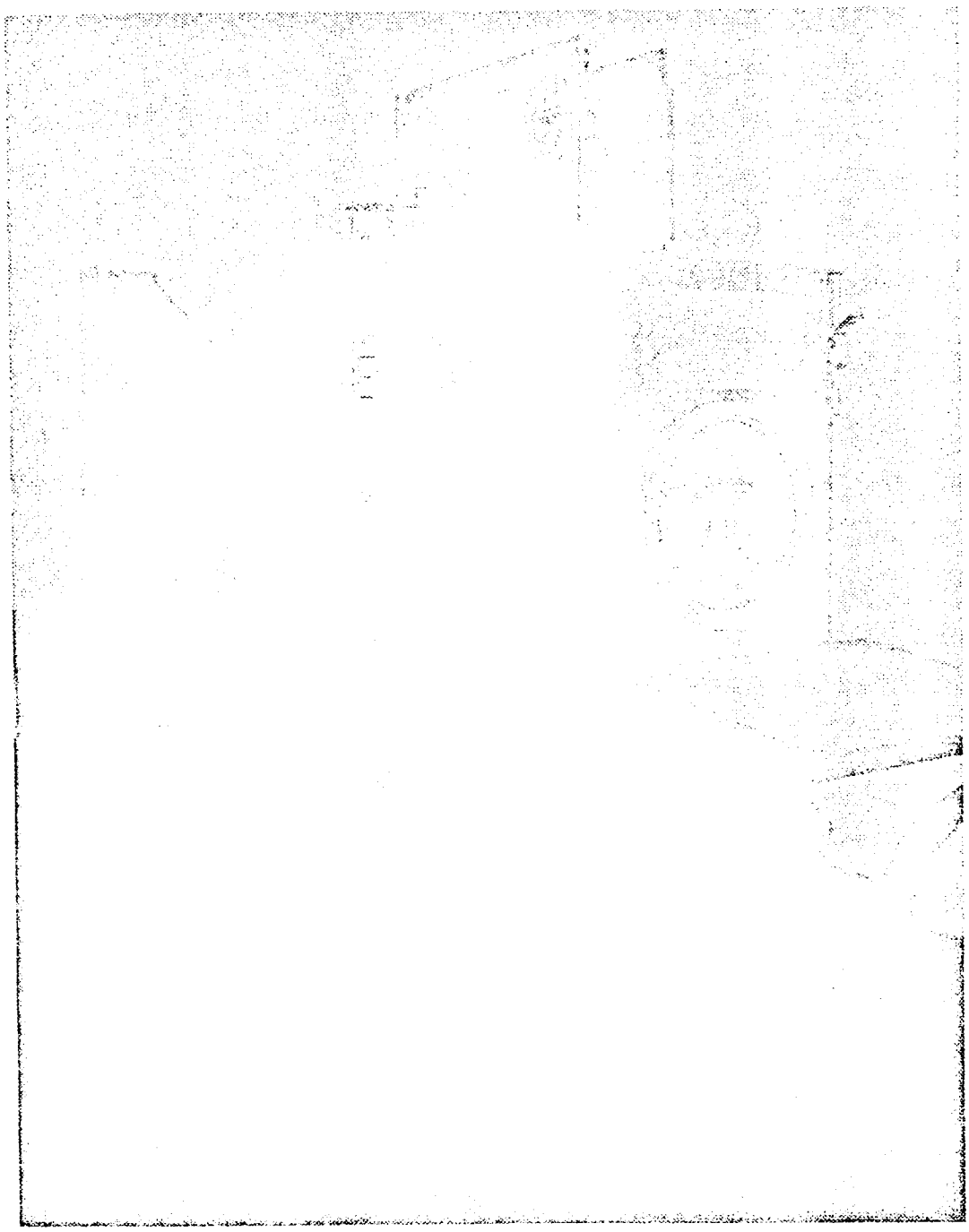

Figure 3. Mechanical tide-predicting machine -- 37 constituents.

C&GS machine was geared for 37 frequencies between one cycle per year to eight cycles per day. Although most periods were incommensurable, the gearing was done so precisely that no constituent was off more than 2^{o} at the end of a year's predictions. The left side of the machine summed the cosine curves. The right side summed the first derivatives of the cosine curves; therefore the amplitude scales on the right were weighted for the constituent speeds. When the derivative side showed a zero sum, the operator recorded the times and heights of the predicted high or low tide for use in the tide tables. When the C&GS bought its first electronic computer, an IBM 650, an attempt to program tide predictions on the 650 disclosed that the mechanical, hand-cranked machine, almost a half century old, could turn out the predictions faster. The comparability vanished quickly as faster electronic computers were developed and tide predictions are now prepared routinely on the latter. The printed output is reproduced directly for publication.

Other countries use more constituents, particularly for shallow water areas where important non-linear combinations introduce the need for additional tidal constituents. An extreme case of the latter came up in trying to improve tide predictions for Anchorage, Alaska. The range of tide is very large, about 25 feet, and the discovery of oil in Cook Inlet brought in deep-draft oil tankers. These required more accurate tide predictions; Figure 4 shows the

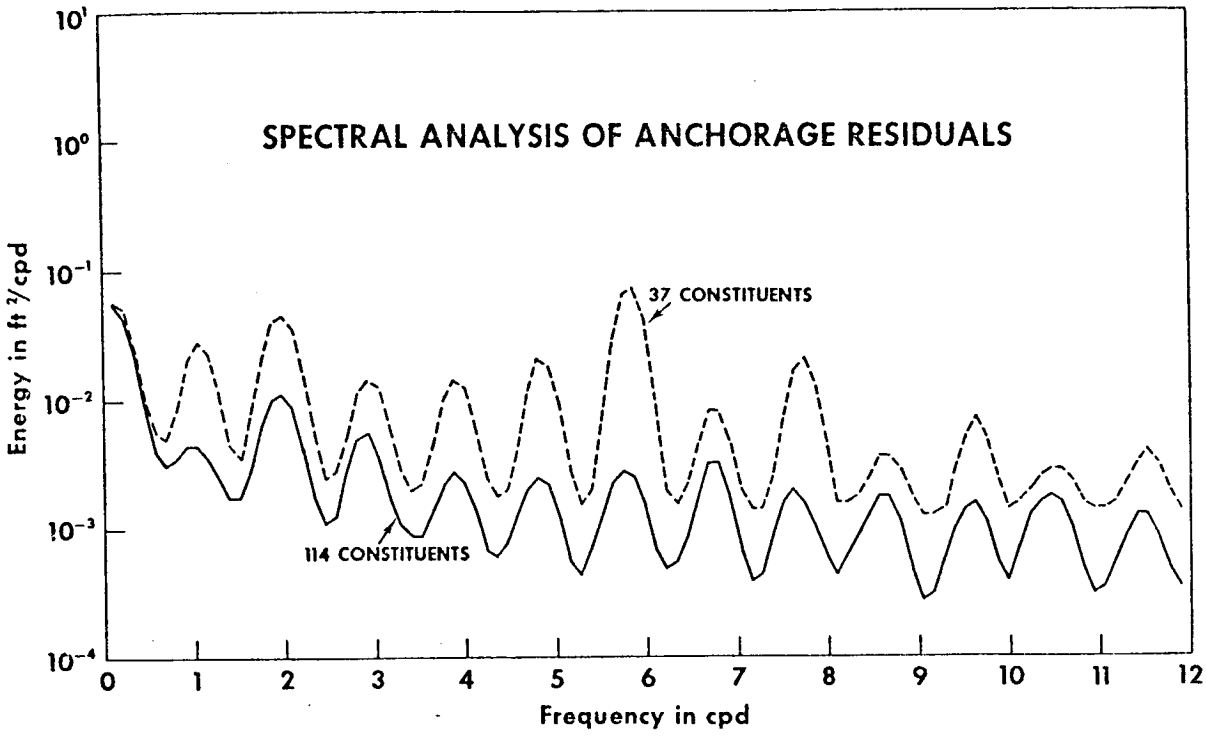

Figure 4. Spectral distribution of residual energy (Anchorage tides -- predicted minus observed hourly heights).

spectral distribution of residual energy (observed minus predicted hourly heights) with the standard 37 constituents and when the set was expanded to 114 constituents. The principal improvement is found at six cycles per day, but some improvement is found in other bands, for example five cycles per day, where no constituents has been considered in the past.

Identifying unknown frequencies of important constituents is quite difficult to the accuracy required for tide predictions. It was a considerable help that it could be assumed that the frequency of any constituent must consist

of integral sums of six specified frequencies. The six, determined by Doodson, are shown in Table 1.

Table 1.

f_a^{-1} = 1 day (period of Earth's rotation relative to Sun)
f_b^{-1} = 1 month (period of Moon's orbital motion)
f_c^{-1} = 1 year (period of Sun's orbital motion)
$f_d^{-1} \approx 8.85$ years (period of lunar perigee)
$f_e^{-1} \approx 18.61$ years (period of regression of lunar nodes)
$f_f^{-1} \approx 20{,}900$ years (period of solar perigee)

$$f_k = S_a f_a + S_b f_b - - - S_f f_f, \quad S=0, \pm 1, \pm 2, - - -$$

Fortunately for the purposes of the tidal spacecraft experimental computations, the five constituents already described (M_2, N_2, S_2, K_1 and O_1) ordinarily include more than 95% of the total energy in a tidal prediction and therefore the experiment could meaningfully be constrained to solving for the harmonic constants of these five.

The spectrum of sea level should be mentioned briefly. Figure 5 (presented in a lecture by Walter Munk) is a log-log presentation of the complete spectrum. The high energy in the very low frequencies is primarily due to thermal causes for periods greater than a month and to barometric variations for periods between a day and a month. The tidal

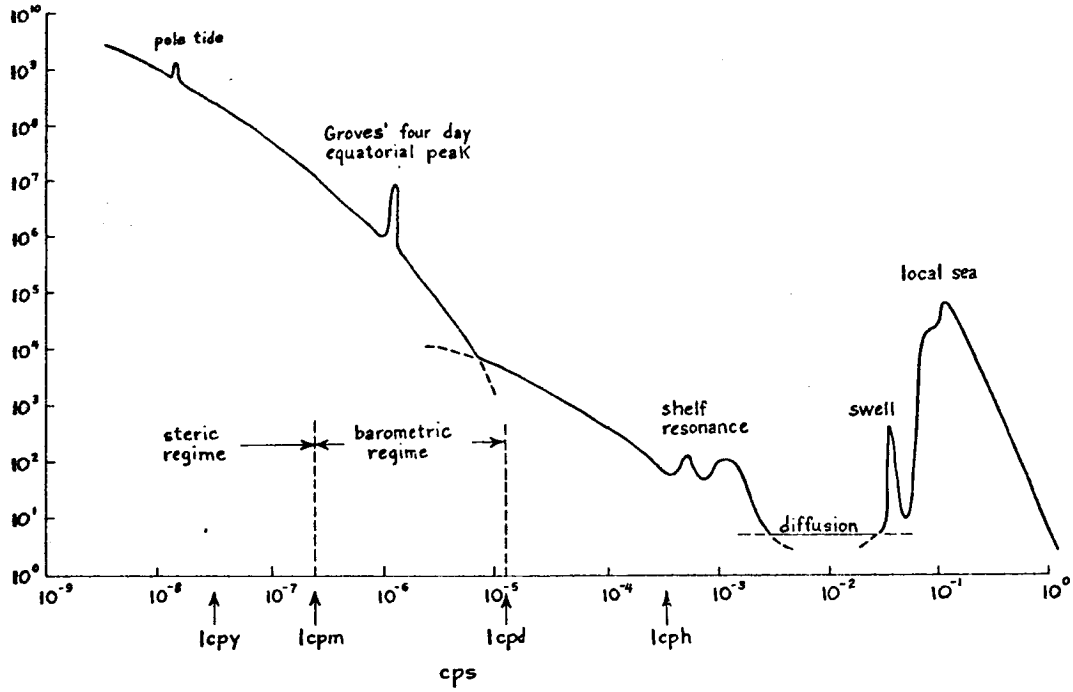

Figure 5. Spectral distribution of wave energy (log-log scale).

lines are superimposed, mostly at 1 and 2 cycles per day. There are shallow-water tides at higher harmonics, mostly 4 and 6 cycles per day. Then follow seiches and tsunamis with periods ranging from minutes to several hours, and finally wind waves (swell and sea). This continuum cannot be predicted because, although the amplitude may be reasonable estimated, the phase is random. Thus, when we analyze for a particular tidal frequency, we get a vectorial combination of the signal and noise. Tide predictions are ordinarily accurate because the signal to noise ratio is large.

It may be of some interest to show the various types of tide found along the U.S. coastline. Figure 6, for the east and Gulf coasts, shows the typical semidaily tide (no large inequality between either the two high waters or the two low waters in a day) on the east coast. The tide is mixed (significant inequality) at Key West and is diurnal at Pensacola. The tides on the west coast (Figure 7) are

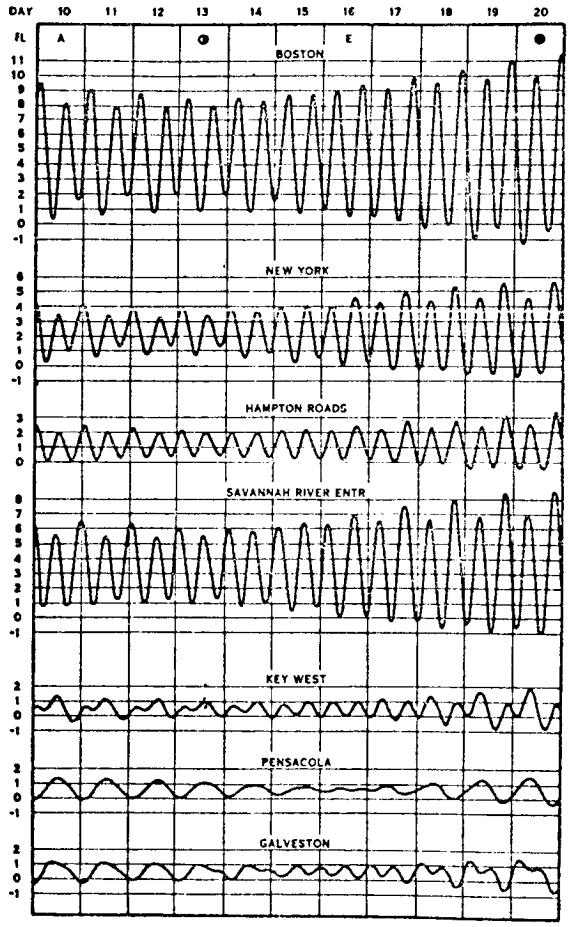

Figure 6. Typical tide curves for U.S. east coast and Gulf ports.

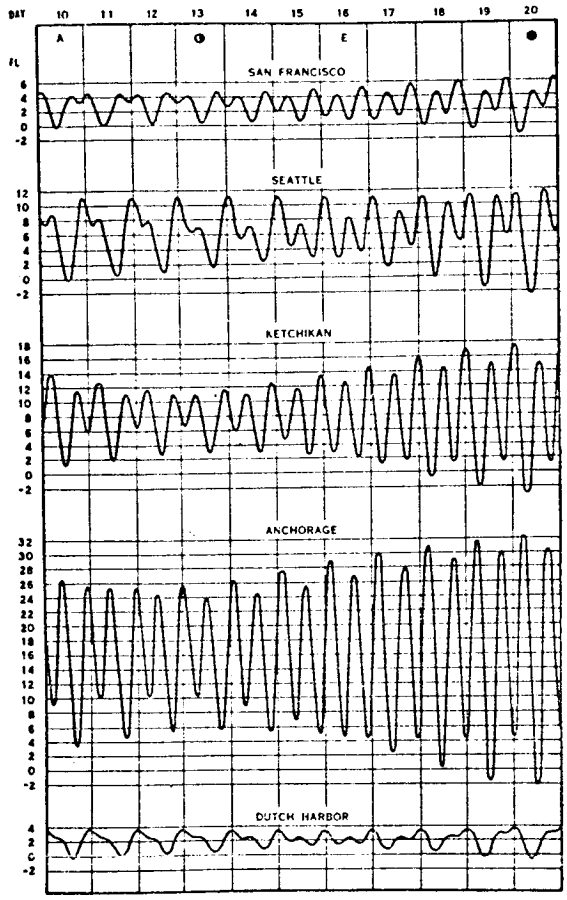

Figure 7. Typical tide curves for U.S. west coast ports.

mostly mixed. Figure 8 shows low-passed (tide-removed daily) values at Atlantic City, New Jersey, for a full year. The large variations in a day or a few days are due to wind set-up along the wide continental shelf. The variations, much larger in winter than summer, indicate why the continuum peaks at low frequencies.

A principal objective in tidal research is the preparation of accurate cotidal and co-range charts. These charts,

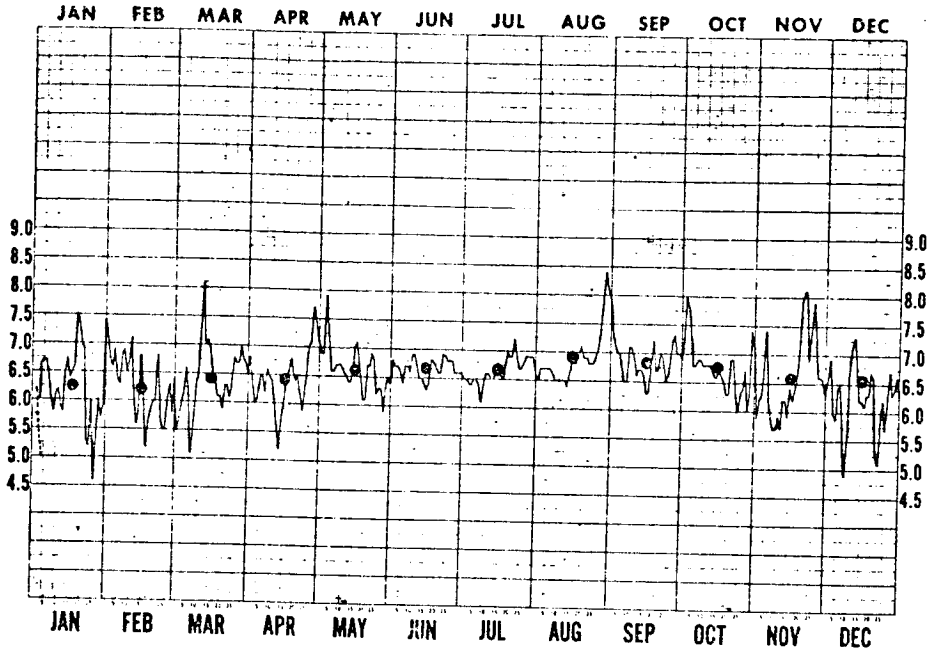

Figure 8. Daily values of mean sea level at Atlantic City, N.J., 1939.

prepared for particular frequencies, usually M_2 or K_1, have cotidal lines connecting points of equal phase and co-range lines connecting points of equal amplitude. Dietrich's cotidal charts (Figures 9 and 10) show his empirical estimates for diurnal and semidiurnal tides respectively based on coastal and island observations. Projecting offshore is clearly a subjective process and therefore cotidal charts prepared by various oceanographers may vary significantly. Actually, most coastal data are measured by tide gauges located on piers within estuaries. Because the tide may be significantly modified by the estuarine bathymetry, this is the worst possible place to obtain data for projecting lines

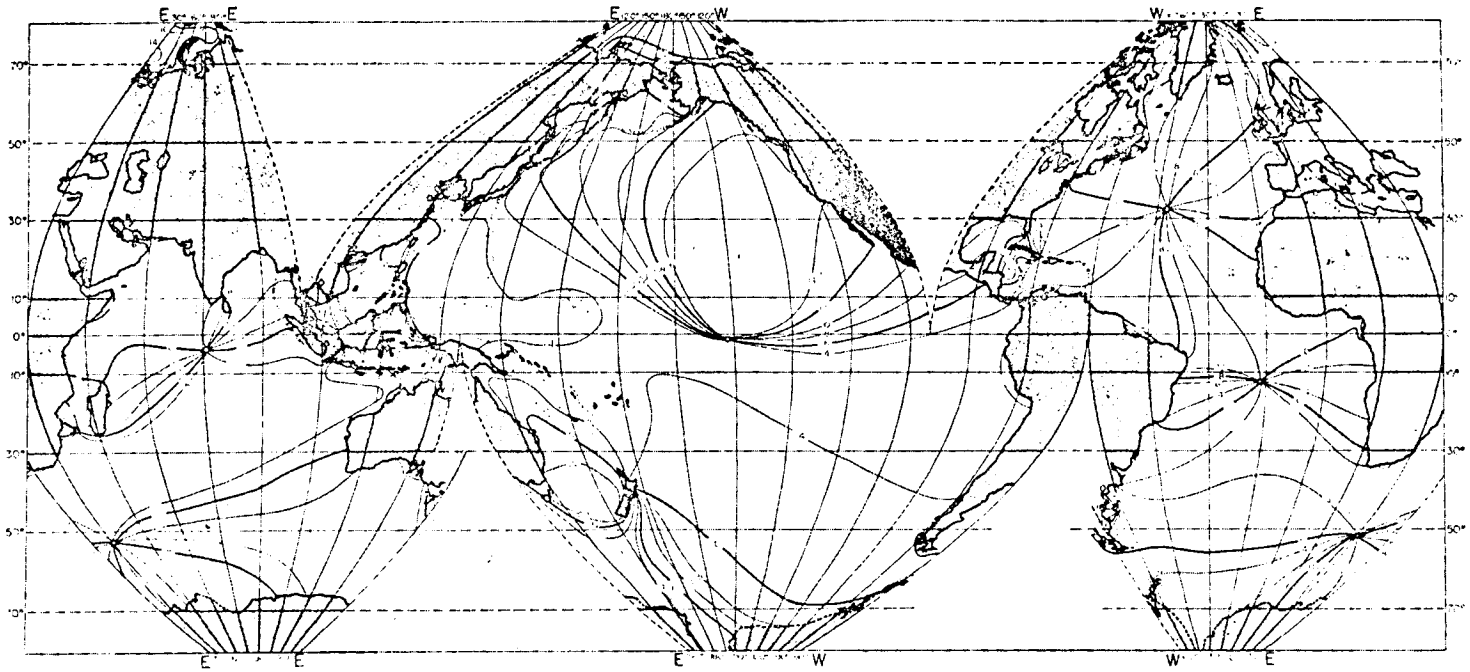

Figure 9. Dietrich's cotidal chart for diurnal tides.

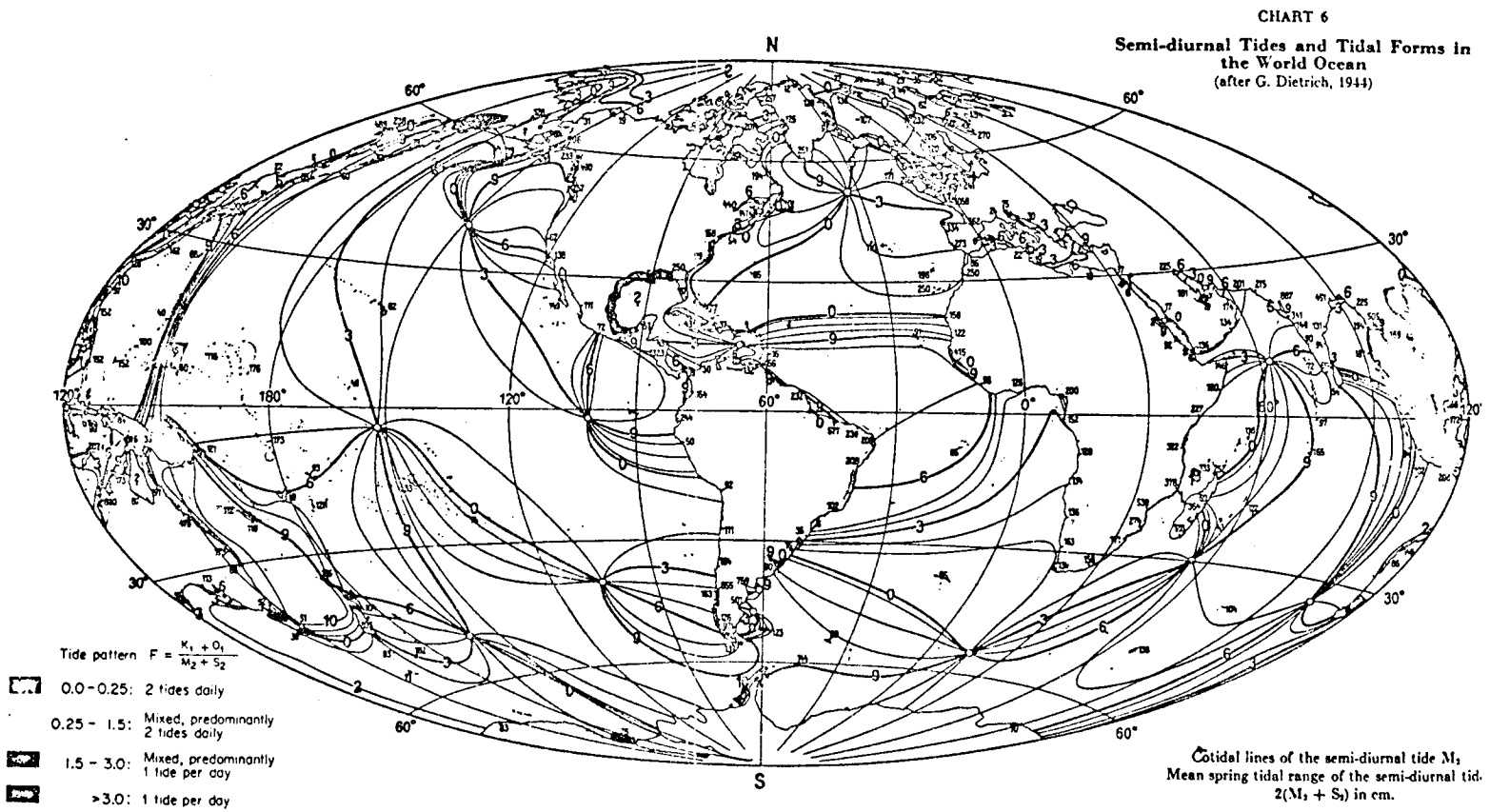

Figure 10. Dietrich's cotidal chart for semi-diurnal tides.

to mid-ocean. An important theoretical feature is the location of the amphidromic (no-tide) points. Note that the locations of these points are entirely different in Dietrich's two charts, illustrating the frequency dependence of the response.

In order to facilitate the preparation of more accurate cotidal charts, a Working Group on Deep-Sea Tides was organized under the auspices of IUGG, SCOR and UNESCO, with Walter Munk as chairman. This group is concerned with encouraging tide observations in a grid of stations spanning the world's oceans, improving the quality of deep-sea tide gauges, and determining optimum analysis procedures for the measurements that are made, usually at very large cost.

Figure 11 shows the NOAA tide gauge being lowered into the water. The gauge was subsequently modified by replacing time releases that were found to be not dependable by acoustic release mechanisms. Figure 12 shows the same gauge after it has left its tripod base on the sea floor and returned to the surface. The two gauges, presently at a depth of about 4,000 meters on the Caribbean sea floor, have additional floation above the instrument frame to offset the added weight of the acoustic releases, a larger frame and a current meter.

A numerical experiment on spacecraft tides is described in the following article, reproduced by permission of the American Geophysical Union. The paper, by Bernard D. Zetler

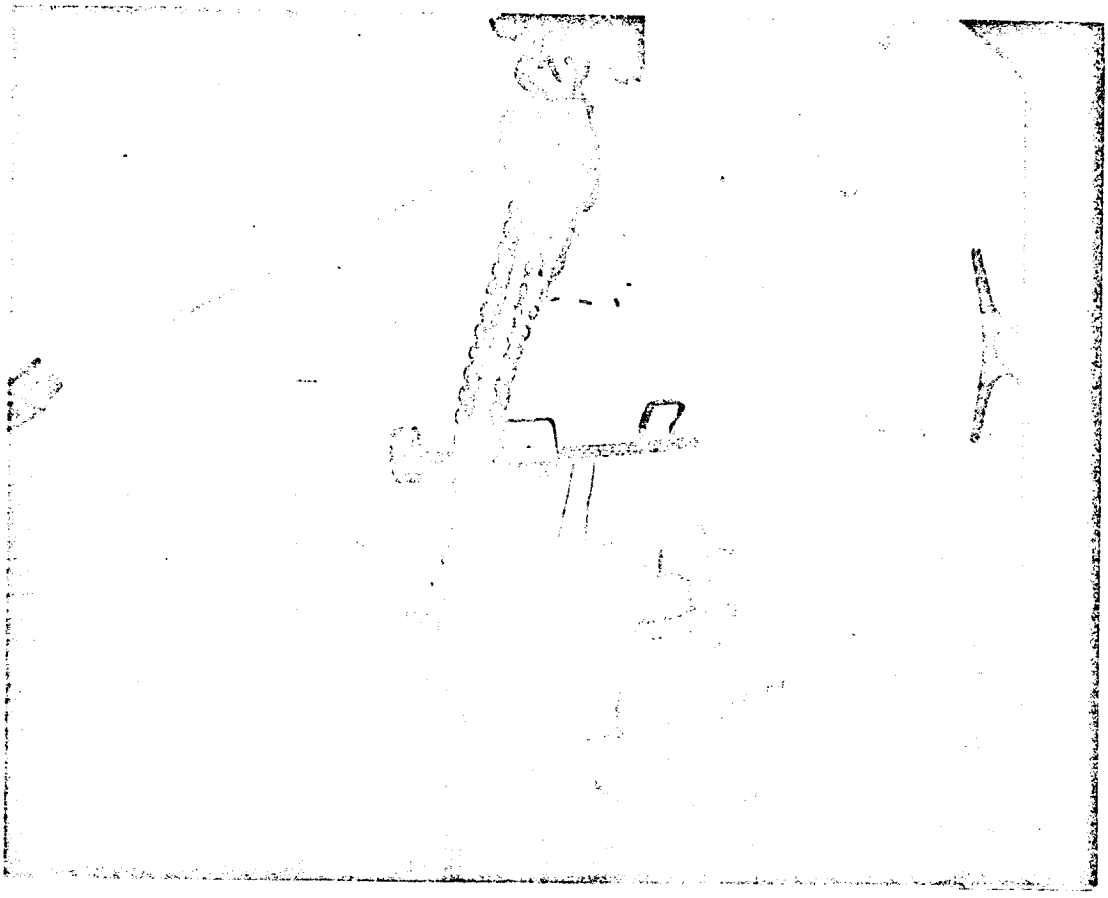

Figure 11. Launching of NOAA deep-sea tide gauge showing expendable tripod.

and George A. Maul, was published in Journal of Geophysical Research, Vol. 76, No. 27, pp. 6601-6605, 1971.

There are certain special orbits for which the conclusions reached in the Zetler-Maul paper are not applicable. If the regression in longitude between successive orbits divides evenly into 360 , then the spacecraft would periodically cover exactly the same set of paths. As a consequence, some areas (as a one degree

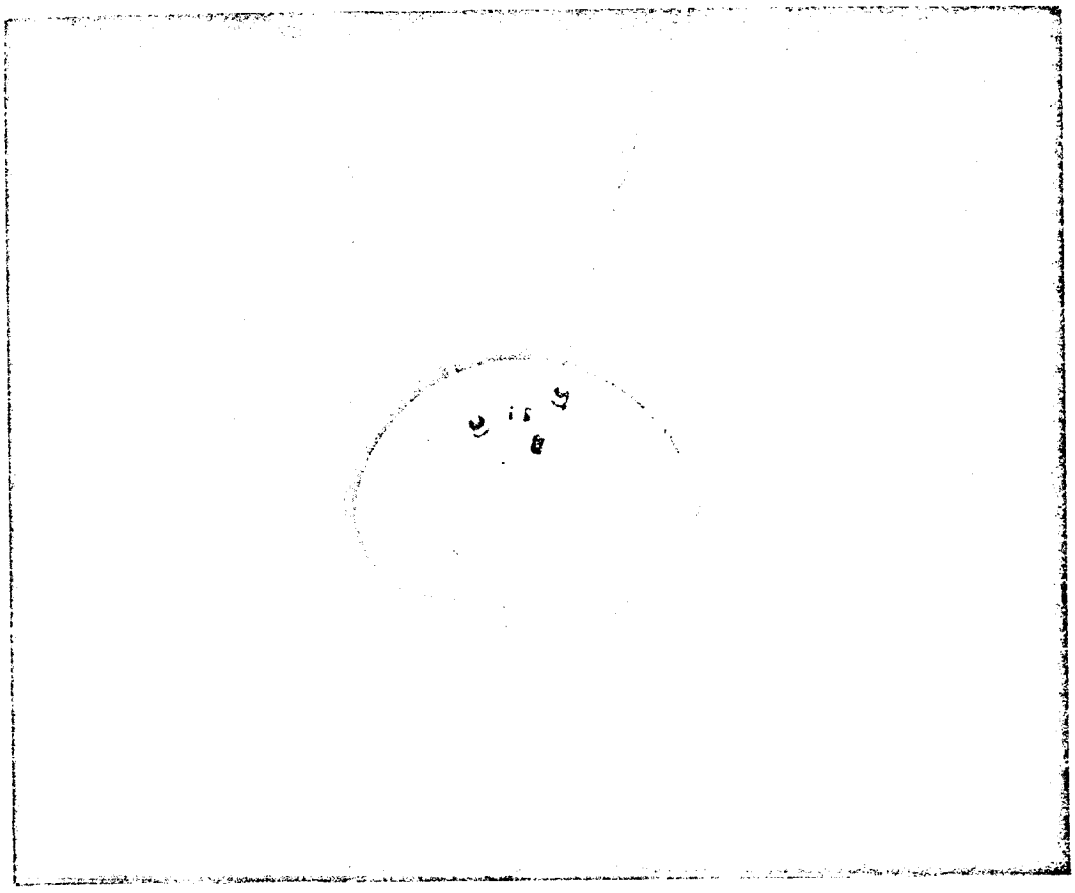

Figure 12. NOAA deep-sea tide gauge after return to surface.

square) would be transited more frequently than in the study but the spacecraft would never pass over many other areas and hence no data would be obtained for these areas.

A more likely (hence more serious) exception is the sun-synchronous orbit. The transit time over a particular area will always be close to a particular solar time or that time plus 12 hours. S_2, the second largest semi-daily tide, has a period of exactly 12 hours. Since the

observations for an area will always be at approximately the same phase in the S_2 cycle, the harmonic constants for S_2 cannot be resolved. As a matter of fact, the S_2 height at that time will be aliased into the mean height, an undesirable consequence for both oceanographic and geodetic purposes.

Only a few years ago, it might have been considered feasible to infer S_2 harmonic constants from the other large semidaily constituents using tidal equilibrium theory and an assumption that since the oceans are not finely tuned to particular frequencies, the response in a narrow frequency band can be assumed to be smooth. However, it has been demonstrated recently that there is a significant meteorological S_2 tide (called a radiational time by Munk and Cartwright). This tide, which exists only in a very narrow frequency band, is believed to be caused by the solar semidaily barometric tide and by a nonlinear contribution of wind stress associated with the solar diurnal onshore-offshore winds. An equilibrium inference of S_2 would not include the meteorological contribution at this frequency.

The frequency of K_1, the largest diurnal constituent, differs from that of S_1 (solar diurnal, period 24 hours) by one cycle per year. It is suggested in the literature that this type of separation is not resolvable with data

from a sun-synchronous orbit over a period of one year. I have no doubt that this is true for a shorter period (with resolvability depending on an extremely high signal to noise ratio) but, as long as there is at least one synodic period within the observation period, I believe such a frequency can be resolved as well as any other of comparable signal to noise ratio. This could be readily tested by a computer experiment similating a sun-synchronous orbit and real tide data.

3. TSUNAMIS

We have many tide gauge records showing tsunamis and these data have been supplemented by visual reports, damage estimates and run-up studies.

Usually tsunamis are generated by an abrupt vertical shift of the sea floor associated with an earthquake. The displacement is transmitted to the sea surface as a crest or a trough. The wave then propagates in all directions but with some directivity (conservation of energy) near the source normal to the fault line of the earthquake.

On the open ocean a tsunami, which travels with a speed of about 400 to 500 knots, is believed to be only about 30 cm high whereas the wave-length may be as long as several hundred kilometers. With a slope of only 10^{-6}, it is not observed by ships at sea. As the wave impinges on coastal

slopes, the wave length shortens and the height of the wave increases. In general it is noted on the shore as a series of rapid changes in sea level with the troughs exposing large areas offshore and the crests inundating coastal areas.

Ships have been carried well inland and left high and dry, structures have been lifted off their foundations and swept to sea, and people have been carried to sea or struck by floating debris. Thus tsunamis have caused significant loss of life and property damage.

Figures 13, 14, and 15 are copies of tide gauge records for Crescent City (California), Caldera (Chile) and Acapulco (Mexico) for the same tsunami. The period and shape of the tsunami records at these stations are quite different. A study of spectra for several tsunamis at different locations demonstrated that certain frequencies at each location appear to be augmented for all tsunamis. Figures 16 and 17, spectra for Honolulu and Santa Monica tsunami records for the same two tsunamis, indicate that the spectra of energy for different tsunamis at the same location tend to be parallel whereas the spectra for the same tsunami at different locations tend to be quite different. This supports the suggestion that the wave is severely distorted by the response characteristics of local bathymetry.

Considerable priority in tsunami research has been assigned to developing a system for measuring a tsunami in

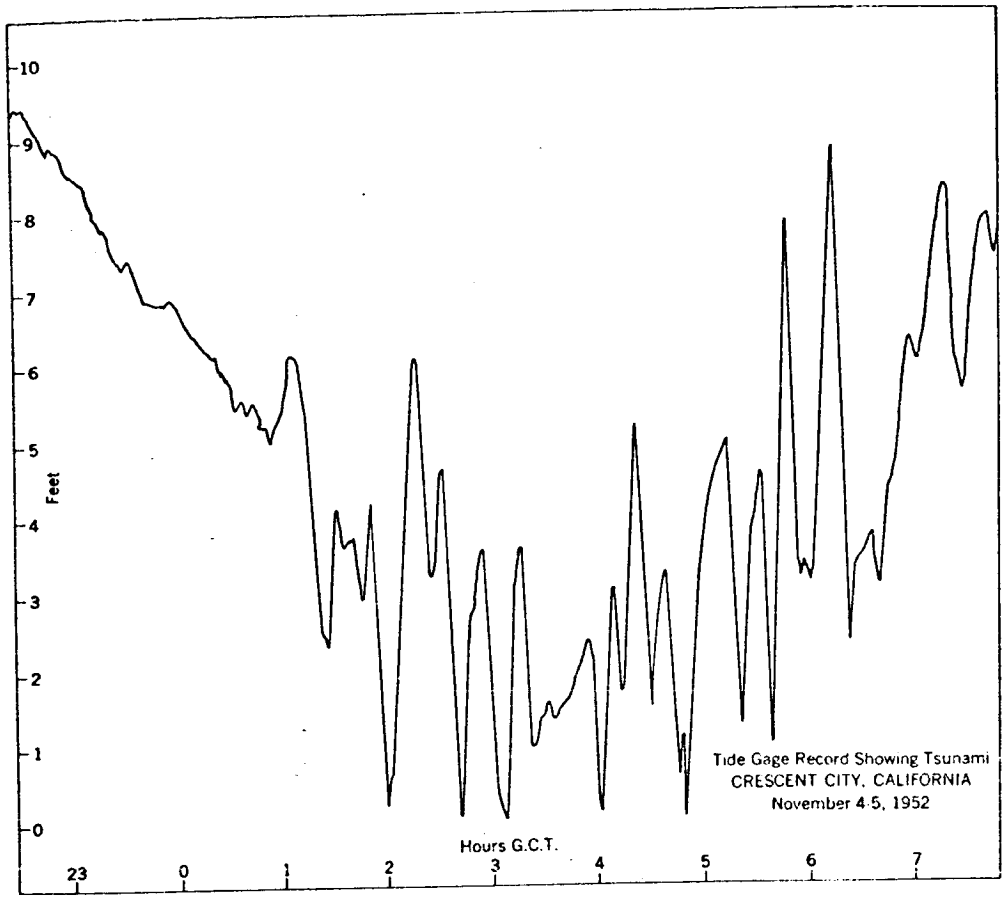

Figure 13. Crescent City, California marigram showing 1952 tsunami.

the deep ocean. If this can be achieved, a subsequent development of a real-time reporting system would greatly improve the capabilities of the international Tsunami Warning System. The existing system (Figure 18), with headquarters at the NOAA Honolulu Observatory, uses an array of seismographs around the Pacific to report earthquake data. Using a very high priority on all available communication systems, the location of an epicenter for a large earthquake is ordinarily computed in less than an hour after the event.

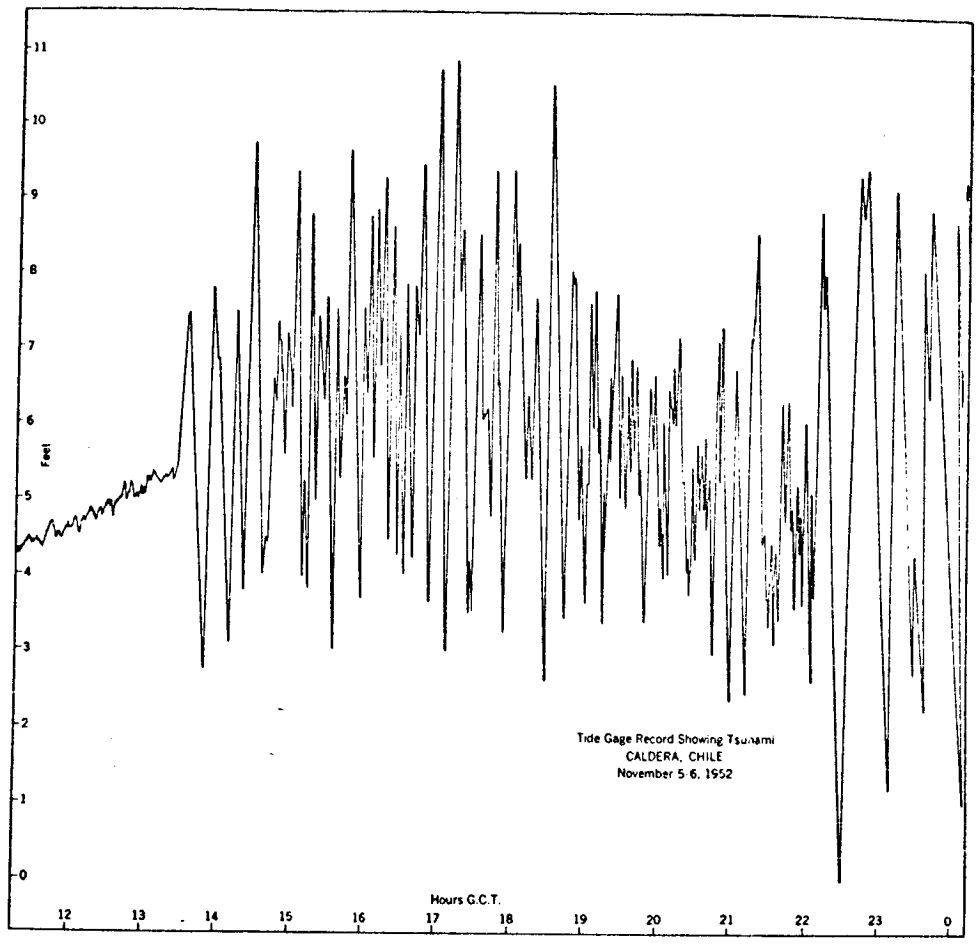

Figure 14. Caldera, Chile marigram showing 1952 tsunami.

The headquarters has rapid communications to a network of reporting tide stations; the travel time to each tide station from any nearby epicenter has been computed and is available on a series of tsunami travel time charts. The tide observers are alerted to watch their tide records (usually remoted for safety and efficiency) at particular times and to report the data from their records. If the tide records confirm the existence of a tsunami, warnings including

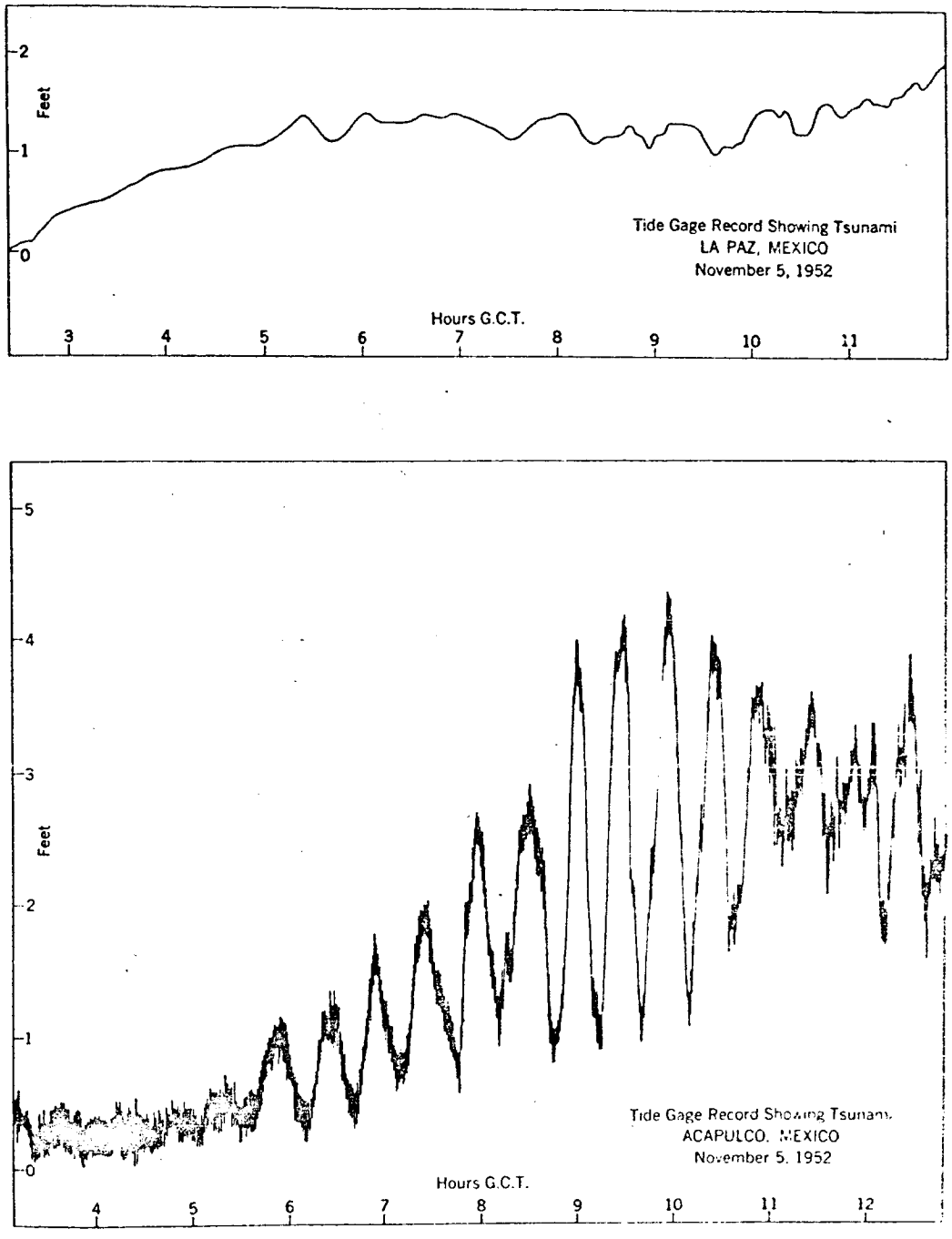

Figure 15. Acapulco, Mexico marigram showing 1952 tsunami.

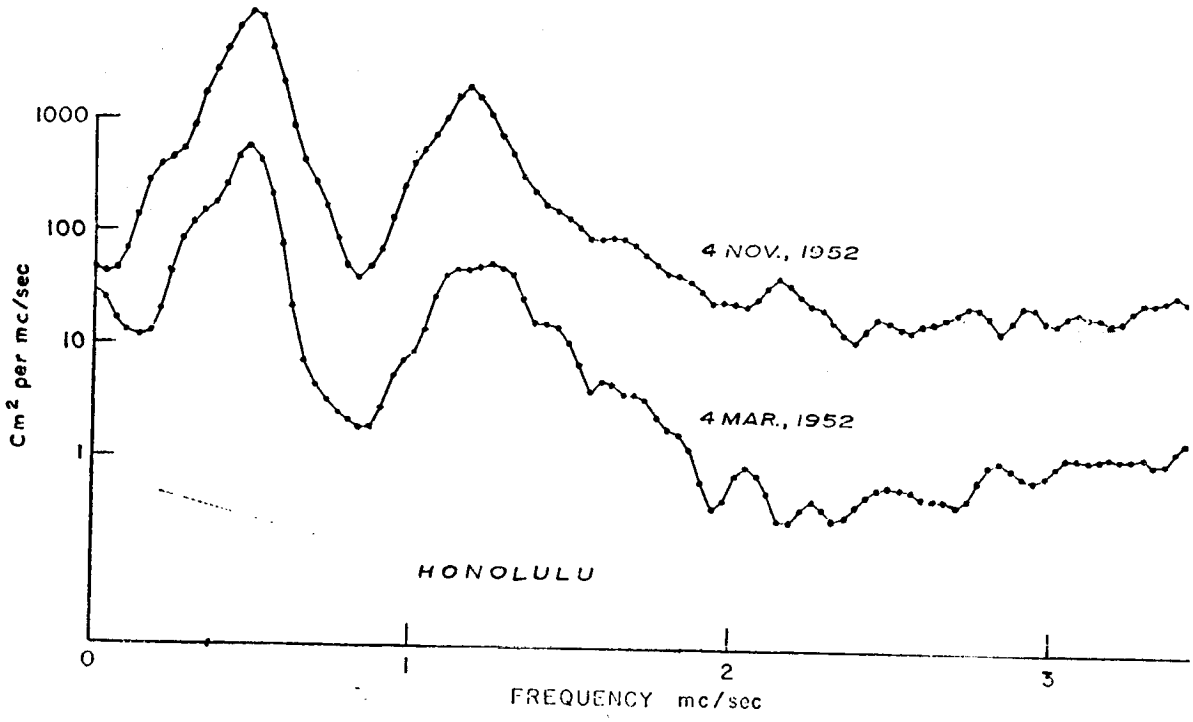

Figure 16. Spectra of tsunamis recorded at Honolulu.

estimated arrival times are distributed to all areas in the system. For localities near an epicenter, warnings may be issued on seismological evidence only.

If a tsunami could be detected on the open ocean from a spacecraft, an estimate of its dimensions would be very valuable to the warning system. However, if the slope of a large tsunami is truly only 10^{-6}, this is roughly equal to a slope of a moderate ocean current system and an order of magnitude smaller than the slope of a major current such as the Gulf Stream. Therefore, a detectable anomaly from the geostrophic slopes in the ocean must be determined. Furthermore, this would require an orbit that happened to be in the

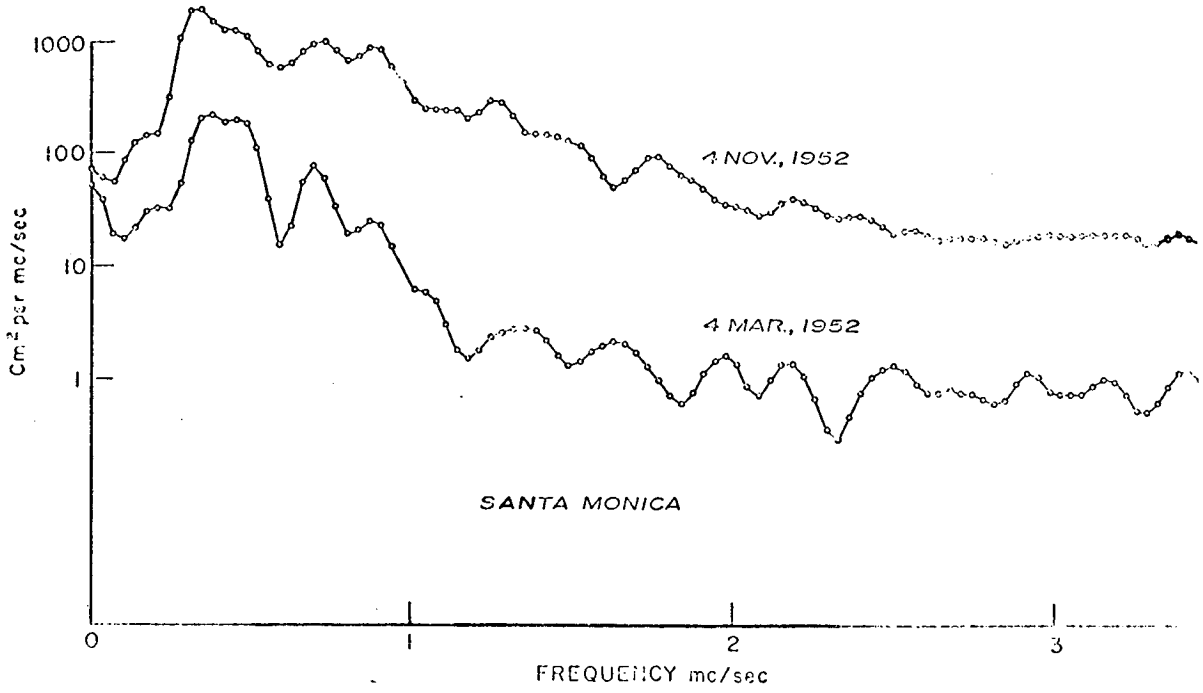

Figure 17. Spectra of tsunamis recorded at Santa Monica.

right place at the right time and that happened to be normal to the wave front (otherwise the slope is even less). The slope calculations would need to be done in real time on the occasions that the warning service issues an alert containing the time and location of the epicenter.

Since the availability and orbit of a spacecraft must be fortuitous and the state of the art needs considerable improvement, it does not seem likely that spacecraft measurements are a likely prime mechanism for warning purposes. However, if the capability of measuring ocean slopes improves

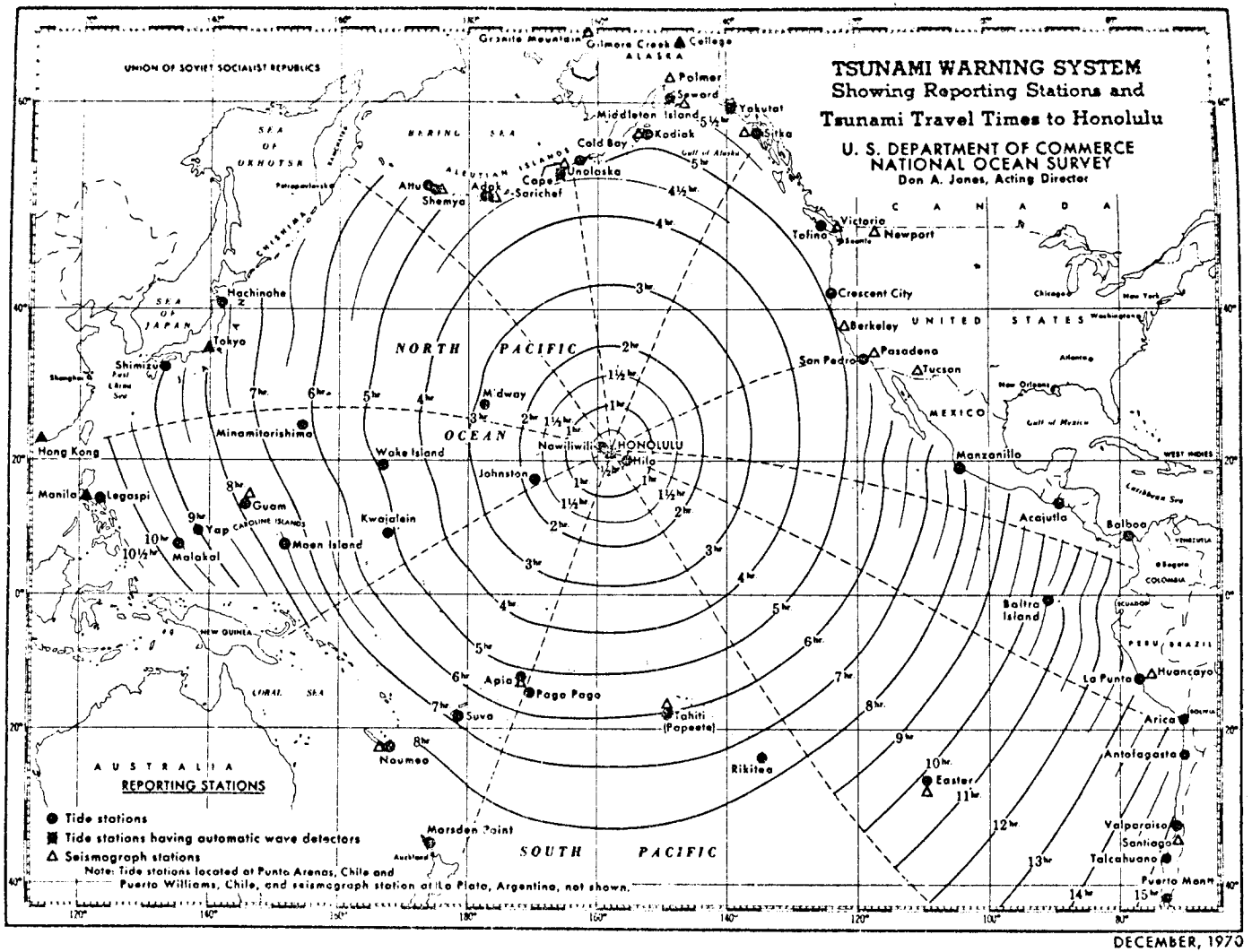

Figure 18. Tsunami warning system, January 1971.

sufficiently, the calculations could be useful for tsunami research by describing the tsunami characteristics on the open sea. Furthermore, under those conditions, the possibilities of using spacecraft as "ships of opportunity" for reporting during an alert would have to be considered.

* * *

GPO 842-756